WAVEFORM EFFECTS ON THE OPERATION OF THE PARALLEL-BRIDGE RECTIFIER SYSTEM AND THE FIELD MODULATED GENERATOR SYSTEM

By

ALTAF-UR-RAHMAN

Bachelor of Engineering
Osmania University
Hyderabad, A.P., India
1966

Master of Engineering
Maharaja Sayajirao University of Baroda
Baroda, Gujarat, India
1972

Submitted to the Faculty of the Graduate College
of the Oklahoma State University
in partial fulfillment of the requirements
for the Degree of
DOCTOR OF PHILOSOPHY
December, 1979

WAVEFORM EFFECTS ON THE OPERATION OF THE PARALLEL-BRIDGE RECTIFIER SYSTEM AND THE FIELD MODULATED GENERATOR SYSTEM

Thesis Approved:

R. Ramakumar
Thesis Adviser

Wm. J. Hughes

Donald W. Grace

D. D. Fitzgerald

Norman N. Hackerman
Dean of the Graduate College

ACKNOWLEDGMENTS

I wish to express my sincere appreciation to Dr. R. Ramakumar, my thesis adviser, for stimulating my interest in this research, and for his guidance and assistance throughout this study.

The suggestions and comments offered by Dr. W. L. Hughes, Dr. D. D. Lingelbach, and Dr. D. W. Grace, members of my doctoral committee, are appreciated.

I wish to thank Dr. C. M. Bacon, Head of the School of Electrical Engineering, for providing the facilities for the experimental work, and Dr. W. L. Hughes, Director of the Engineering Energy Laboratory, for making the field modulated generator and the energy laboratory available for the experimental investigation. A note of thanks is given to Mr. Vijaykumar Madali, School of Mechanical and Aerospace Engineering, Oklahoma State University, for his advice on the computer programs used in the course of this study.

The financial support received from the National Science Foundation Grant No. ERDA/NSF-AER 75-00647 in the early stages of my doctoral program, from the School of Electrical Engineering as a graduate teaching associate, and from the Fluid Power Research Center as a research associate is gratefully acknowledged.

Special gratitude is expressed to my wife, Husanara, my daughters, Kausar and Arshiya, for their understanding, patience and sacrifices during my study in this country. I am grateful to Ms. Louise Sumpter and Ms. Charlene Fries for the prompt and excellent typing of this thesis.

Finally, I would like to dedicate this thesis to my parents, brothers, and sisters for their constant encouragement throughout my doctoral program.

TABLE OF CONTENTS

TABLE

LIST OF FIGURES

LIST OF SYMBOLS

B	Specific magnetic loading, Wb/m^2.
C	Stator tuning (bridge-input) capacitance per phase, F.
D	Stator bore diameter, m.
e	Instantaneous value of source voltage, V.
e_a, e_b, e_c	Instantaneous values of voltages induced in the three stator phase windings, V.
e_{am}, e_{bm}, e_{cm}	Instantaneous values of voltages induced in the three stator phase windings with field modulation, V.
E	Maximum peak induced voltage/phase in the stator, V.
E_{ph}	Induced rms voltage per phase, V.
f	Basic machine frequency, Hz.
f_a	Average machine frequency, Hz.
f_m	Modulation frequency, Hz.
F	Constant defined by Equation (3.3.59).
G	Output coefficient, $kW\text{-}second/m^3$.
G_1	Constant defined by Equation (3.3.69).
i	Instantaneous value of source current, A.
i_a, i_b, i_c	Instantaneous values of phase currents in the three stator windings, A.
i_{ac}, i_{bc}, i_{cc}	Instantaneous values of bridge-input capacitor currents, A.
$i_{a\ell}$, $i_{b\ell}$, $i_{c\ell}$	Instantaneous values of bridge-input currents, A.
i_f	Instantaneous value of excitation current under modulation, A.
i_ℓ	Instantaneous value of load current, A.

I_f	Peak value of excitation current, A.
I_ℓ	Magnitude of load current at a given instant, A.
$I(0)_\ell$	Initial value of load current at $\theta = 0$, A.
I_p	Phase current (rms), A.
K	Ratio of rectangular pulse width to half cycle.
K_f	Form factor.
K_{ff}	Filter factor.
K_v	Ratio of V_d to E read from Figure 23.
K_w	Winding factor.
ℓ_g	Radial air-gap length, m.
L	Stator commutating inductance per phase, H.
L_C	Stator core length, m.
m	Modulation frequency ratio (f/f_m).
n	Minimum rotor speed, r/s.
N	Minimum speed of operation, r/min.
2p	Total number of poles.
P	Constant defined by Equation (3.3.62).
P_o	Power output of FMGS, kW.
q	Specific electric loading, ampere-conductors/m.
R_ℓ	Load resistance, Ω.
t	Time, s.
T	Number of turns per phase in stator.
u	Rotor peripheral speed, meters per second.
v	Instantaneous value of bridge-input voltage, V.
v_a, v_b, v_c	Instantaneous values of bridge-input voltages of three phases, V.
v_f	Instantaneous value of excitation voltage, V.
v_ℓ	Instantaneous value of load voltage, V.

V_d	Average (dc) load voltage, V.
V_f	Peak value of excitation voltage, V.
V_o	Initial value of bridge-input (capacitor) voltage, V.
V_p	Peak value of output voltage, V.
V_{rms}	Output voltage rms value, V.
X_C	Capacitive reactance of bridge-input capacitor, Ω.
X_L	Commutating reactance of stator per phase, Ω.
Y	Pole pitch ($\pi D/2p$), m.
α	Value of ωt over which phase-a conducts through the load, rad.
β	Angle by which e_a leads $\omega t = 0$, rad.
γ	Value of ωt at which diode pair 1 starts conduction, rad. (See Figures 12, 13, 14 and 20.)
Θ	Angle which is equal to ωt, rad.
Θ_1	Angle which is equal to $\pi/3$, rad.
ϕ	Magnetic flux per pole, Wb.
ω	Source electrical angular frequency, rad/s.
ω_a	Average machine electrical angular frequency, rad/s.
ω_m	Modulation angular frequency, rad/s.

CHAPTER I

INTRODUCTION

1.1 General Literature Review

Variable-speed adjustable-frequency (VSAF) [1] power systems have many attractive practical applications. They can serve as variable-voltage variable-frequency power supplies for electric drives and in ground transportation, deriving their mechanical input from an unregulated shaft [2, 3]. Operated as variable-speed constant-frequency (VSCF) systems, they can be used with non-synchronous prime-movers such as aeroturbines [4-7], aircraft engines and in other vehicles for power generation [8, 9]. VSCF systems have been suggested as an alternative in engineering systems for harnessing renewable energy sources such as geothermal and wind. In addition, they are ideally suited as interfaces between flywheel energy storage systems and conventional utility grids [10]. Recently, VSCF systems have been recommended as an alternative power generation scheme for application in dispersed solar-thermal-electric power systems employing "parabolic-dish electric-transport" [11]. Over the past two decades, several variable-speed adjustable (constant)-frequency systems have been proposed. The approaches used generally fall into two broad categories, namely (i) differential methods, and (ii) non-differential methods.

Mechanical techniques employing variable ratio gears [12], and electrical techniques involving the feeding of slip frequency power to

rotor [13, 14], to obtain constant speed and/or frequency, belong to the first category.

Static frequency changers such as AC-DC-AC conversion systems [15], purely rotary devices (without any solid-state switching) such as AC commutator generators [16, 17], and combinations of rotating machines and solid-state switching devices such as diodes and thyristors [18, 19], come under the second category. Numerous applications of solid state devices in electrical power and other industries have been discussed in detail in the literature [20].

Judicious synthesis of rotating machines with solid-state switching devices and the use of field modulation and demodulation techniques combined with low frequency switching have resulted in a new variable speed adjustable frequency power system known as the Field Modulated Generator System (FMGS) [21]. This system has been under development at Oklahoma State University since 1970.

1.2 Background

The term 'field modulation' refers to varying the magnetic field in the air-gap of a rotating machine as desired by varying the excitation current to obtain a variety of desired outputs. The concept of employing field modulation techniques to control the output frequency of a generator has been disscussed in the literature for at least twenty years [22-25]. However, most of the early attempts were not highly successful either for the lack of high-speed high-powered solid-state switching devices at that time or due to low overall efficiencies resulting from line-to-line short circuits at the machine terminals during commutation or both.

With the availability of economical high-powered solid-state switching devices such as thyristors and diodes, and with the introduction of a new rectifier connection scheme known as the Parallel-Bridge Rectifier System (PBRS) [26], interest in field modulation techniques was revived in the early seventies [27].

The field modulated generator system consists of a specially designed three-phase high-frequency alternator operating in conjunction with solid-state electronic circuitry to provide single-phase output at the desired low frequency. The field coil is excited with alternating current at the desired low frequency instead of the conventional direct current. The outputs from the three stator phases are processed using a parallel-bridge rectifier system and a four thyristor inverter followed by a low-pass filter network [28].

With sinusoidal ac excitation of the field coil at modulation frequency, a parallel-bridge rectifier system connected across the machine stator terminals yields an output which consists primarily of a full-wave rectified sine wave at the frequency of modulation; in addition there is a small ripple at six times the basic machine frequency and a small dc component. If the ratio of the basic electrical rotational frequency to the modulation frequency is greater than ten, the ripple and the additional dc component become negligibly small.

In general, incorporating solid-state power conditioning devices at the outputs of conventional rotating machines distorts the waveforms and introduces harmonics in various parts of the system. As such, analysis and modeling of FMGS is complicated by the inherent rectification, inversion and filtering processes involved and the manner in which their effects are reflected back into the machine and affect its behavior.

Presence of stator tuning capacitors complicates the problem by providing closed paths for harmonic currents to circulate. The FMGS has been analyzed and a mathematical model for it has been developed based on the idealizing assumption that all waveforms are sinusoidal and by considering only fundamental components in the analysis [29]. Results based on this theory have been experimentally verified and the correlation was well within acceptable limits [30].

The FMGS has been under development at Oklahoma State University for the past nine years. Several prototypes have been designed, fabricated, and successfully tested. During this process, it was observed that certain variations in the magnetic circuit design of the FMGS yielded significant dividends by way of reducing the excitation requirements and improving the overall efficiency and power output capability. The variations primarily consist of changing the no-load field-form (flux distribution in the airgap), which, in turn, alters the induced voltage wave form in the stator windings under both loaded and no-load conditions. In particular, a slotted rotor with magnetic neutral planes in the centers of alternate teeth (instead of being in centers of slots) [31] corresponding to a no-load induced voltage waveform which is flat topped (essentially a rectangular pulse) and extends slightly over one half of the half-period resulted in the best performance, manifested in terms of high efficiency, improved waveform (less filtering) and decreased excitation requirements. This phenomenon has not yet been studied from the theoretical point of view.

1.3 Problem Statement

The primary objective of this thesis research is to study the effect

of non-sinusoidal, especially flat-topped, waveforms on the operation of the FMGS. Since the nucleus of the field modulated generator system is an alternator feeding into a PBRS, the first step in achieving the objective will be to study the influence of carefully selected flat-topped waveforms on the operation of the parallel-bridge rectifier system. The results of this analysis can then be employed to study the effect of flat-topped waveforms on the performance of the FMGS. Clearly, the results of this work are applicable and can be extended to any system that utilizes the PBRS as the key component in its operation.

1.4 Outline of the Method of Study

The parallel-bridge rectifier system consists of three full-wave bridges, connected one each across the three isolated phases of a three-phase power system. The outputs of the three bridges are tied in parallel across the load. The waveform of the voltages induced in the stator windings of an alternator changes depending on the load and the associated armature reaction effects. A rigorous analysis of the PBRS-alternator combination, based on the initial source voltage waveform and its dependence on load, is extremely complicated. In this thesis, as a first step, some judicious approximations are made to understand the basic behavior of the PBRS with such non-sinusoidal waveforms.

It was observed from the oscillograms obtained from experimental prototypes that, in the absence of bridge-input capacitors [32], the induced voltage waveform closely approximated a rectangular pulse. Consequently, the PBRS is first analyzed with a rectangular pulse waveform as input and with a resistive load.

The use of proper stator tuning capacitors decreases the excitation requirements and improves the efficiency of an alternator. Similar advantages are observed with FMGS also. The induced voltage waveform under full load conditions with bridge-input capacitors and resistive load is very close to a symmetric trapezoid with top width approximately equal to one third of the half-period. This is a consequence of the no-load field-form, magnetic circuit configuration and armature reaction effects. Therefore the PBRS with bridge-input capacitors and resistive load is analyzed next with this trapezoidal waveform as input.

In order to develop certain design guidelines for the FMGS, a relationship between the average voltage across the load and the amplitude of the source voltage is derived for different values of circuit parameter ratios. The results of the PBRS study directed towards analyzing waveform effects under dc excitation are extended to the field modulated case by using proper modulation factors. Finally, a set of experiments are conducted using the available experimental prototype to establish the validity of the results of the theoretical analyses.

In the following paragraphs, brief descriptions of the procedures followed and the manner in which the results are brought together are given.

1.4.1 Operation of the PBRS with Rectangular-Pulse Source Voltage Wave-forms (Without Bridge-Input Capacitors)

In order to develop the background necessary to study the effect of non-sinusoidal waveforms on the operation of the PBRS and the FMGS, a thorough study of the PBRS without bridge-input capacitors and with

rectangular pulse source voltage waveforms of variable width is undertaken. Circuit differential equations are set up for various voltages and currents in the idealized model and solved using proper initial values and boundary conditions. In the analysis, two angles, α and β, related to the "on" and "off" conditions of various diodes, play a key role. Values of these angles are numerically evaluated by solving a set of non-linear algebraic equations obtained by the application of proper boundary conditions. The non-sinusoidal nature of the input waveform necessitates the development of current and voltage expressions during different portions of a half-cycle. In order to determine the relationship between the circuit parameter ratio (X_L/R_ℓ), the ratio (K) of the input pulse width to the half-period, angles α and β, it is necessary to consider different ranges of values for angles α and β due to the overlapping of current and voltage waveforms. Theoretical values of α and β are presented with non-dimensional circuit constant (X_L/R_ℓ) and pulse width ratio (K) as parameters. Theoretical waveforms of different voltages and currents are derived and shown for a specific value of the pulse width ratio (K) to illustrate the nature of the results obtained.

1.4.2 Operation of the PBRS with Trapezoidal Source Voltage Waveforms (With Bridge-Input Capacitors)

The induced voltage waveform under full load conditions with bridge-input capacitors and resistive load is a symmetric trapezoid with the top width approximately equal to one third of the half-period. The PBRS with bridge-input capacitors and resistive load is therefore analyzed next with this waveform as input. With flat-topped source voltages, the

bridge-input voltage is not expected to vary much during the conduction duration of that bridge and consequently the capacitor current during this period will be small compared to the load component of the bridge-input current and hence neglected in the analysis.

The approach used in the analysis is similar to the one used in the previous section. Differential equations relating the various voltages and currents in the model are set up and solved using proper boundary conditions. Two angles, γ and β, related to the "on" and "off" states of various diodes are evaluated by solving appropriate non-linear algebraic equations. Different ranges for the sum of angles γ and β need to be considered to cover the practical range of circuit parameter ratios. Theoretical values of γ and β are presented with non-dimensional circuit constants (X_L/R_ℓ) and X_L/X_C) as parameters. Theoretical waveforms of various voltages and currents are plotted for the cases considered and the results are discussed.

1.4.3 Waveform Effects on the Operation of the FMGS and Development of Design Guidelines

The different waveform effects studied in Steps 1.4.1 and 1.4.2 are valid for an alternator-PBRS combination under dc excitation. From the results of the study of trapezoidal waveform effects on PBRS, a relationship between normalized (with respect to the maximum value of the induced voltage in the stator winding of each phase) load voltage and the circuit parameters can be derived. The PBRS studies for conditions of dc excitation can be extended to the field modulated (ac excitation) case by using proper modulation factors. The relationship between the load voltage, the maximum value of the induced source voltage and the circuit

parameters provides a starting point for the development of certain basic design guidelines for the FMGS.

1.4.4 Experimental Investigation

As a final step, a set of experiments are performed using the available experimental prototype to establish the validity of the theoretical analyses. The different current and voltage waveforms and the angles γ and β obtained from experimental results are compared with their theoretical counterparts and an attempt is made to explain the discrepancies.

1.5 Organization of the Thesis

Chapter II presents a theoretical analysis of the operation of the PBRS with rectangular-pulse source voltage waveforms and without bridge-input capacitors. Values of key angles α and β are presented in the form of a family of plots, plotted against (X_L/R_ℓ) and (K) as parameters. Theoretical waveforms of different voltages and currents are presented and discussed.

Chapter III presents a theoretical analysis of the operation of the PBRS with bridge-input capacitors, when the source voltage waveforms are trapezoidal. Relationships between key angles γ and β and circuit parameter ratios are derived and presented in the form of a family of plots. Theoretical waveforms for different voltages and currents are obtained and the results are discussed.

Chapter IV employs the results of Chapter III to obtain a relationship between the normalized value of the average (dc) load voltage and the maximum value of voltage induced in the stator windings for different values of circuit parameters. Extension of the PBRS studies to the field

modulated case is discussed and some design guidelines of practical significance are developed in terms of the system output parameters.

Chapter V documents the results of experimental investigations conducted to establish the validity of the theoretical analyses. Experimental procedures employed and the resulting oscillograms are recorded. Theoretical and experimental results are compared and sources of errors are discussed.

The thesis concludes with a summary of the results and suggestions for further work in Chapter VI.

CHAPTER II

EFFECT OF RECTANGULAR PULSE WAVEFORM ON THE OPERATION OF THE PARALLEL-BRIDGE RECTIFIER SYSTEM

2.1 Introduction

Rectification systems have been under study since the beginning of this century. With the availability of economic high-powered solid state switching devices such as thyristors and diodes, their application in rectification, inversion, control and frequency conversion is continuing to interest researchers. The parallel-bridge rectifier system consists of three full-wave bridges, connected one each across the three isolated phases of a three-phase power source, with their outputs tied in parallel across the load. Ramakumar et al. [33] have presented a detailed analysis of the parallel-bridge rectifier system for both resistive and inductive load conditions for the case of sinusoidal source voltage waveforms and without capacitors at bridge-inputs. Operation of alternators with parallel-bridge rectifier systems [34] without bridge-input capacitors has also been studied in detail for the case of sinusoidal source voltage waveforms. It has been observed in practice that a flat-topped waveform which extends slightly over one half of the half-period improves the performance of devices that employ the parallel-bridge rectifier system.

In order to develop an understanding of the effect of flat-topped waveforms on the operation of devices employing the PBRS, as a first step, operation with a rectangular pulse waveform of variable width is studied in detail.

This chapter presents the results of a detailed theoretical analysis of the PBRS without capacitors at bridge inputs under resistive load conditions for a rectangular pulse source voltage waveform [35]. The approach consists of setting up differential equations relating the various voltages and currents in the idealized model of the system and solving them with proper initial and boundary conditions. In the analysis, two angles, α and β, related to the "on" and "off" conditions of various diodes play a key role. These angles, which in turn are related to the circuit parameter ratio (X_L/R_ℓ) and the ratio (K) of the input pulse width to the half-period, are evaluated by solving appropriate non-linear algebraic equations using an IBM 370 digital computer.

Section 2.2 begins with the circuit model of the PBRS and the idealizing assumptions involved in its formulation. The general nature of the waveforms is discussed to illustrate the circuit interactions within the model. In this study, the ratio (K) of the input pulse width to the half-period is limited to the range given by $0 < K \leq (2/3)$. This appears to be the realistic range for most of the practical cases of interest. Different ranges of values for angles α and β are considered in the analysis due to the overlapping of current and voltage waveforms.

Section 2.3 presents the formulation of circuit differential equations and their solution using proper boundary conditions. The non-sinusoidal nature of the input waveform requires splitting the conduction duration into a number of segments for analysis. The key angles α and β

are introduced and evaluated. Theoretical values of α and β are presented with non-dimensional circuit constant (X_L/R_ℓ) and the pulse width ratio (K) as parameters. Theoretical waveforms of different voltages and currents for a chosen value of K are shown for specific parameter ratios (X_L/R_ℓ) to illustrate the nature of the results obtained.

Section 2.4 summarizes the theoretical results obtained and discusses the various current and voltage waveforms for different values of the parameter ratio (X_L/R_ℓ).

2.2 Idealized PBRS Model

An idealized circuit model of the parallel-bridge rectifier system under study is shown in Figure 1. The assumptions involved in the development of this circuit model are listed below.

1. All solid state devices are ideal; zero forward voltage drop and zero reverse current.

2. Power source impedance is purely reactive.

3. Each phase of the source is modeled as an ideal voltage source in series with a commutating inductance L.

4. The source voltage waveform is a rectangular pulse.

Figure 2(a) shows the three rectangular pulse voltage waveforms and their relationship to the corresponding phase currents. The value of the pulse width ratio (K) is chosen as 0.4 for the purpose of illustration. The general nature of the load current waveform is shown in Figure 2(b). The load current is periodic with a period of ($\pi/3$). The non-sinusoidal nature of the input waveform requires splitting the conduction duration into a number of segments as shown in Figure 2(a) for the purpose of analysis. The conduction duration of each bridge depends on the

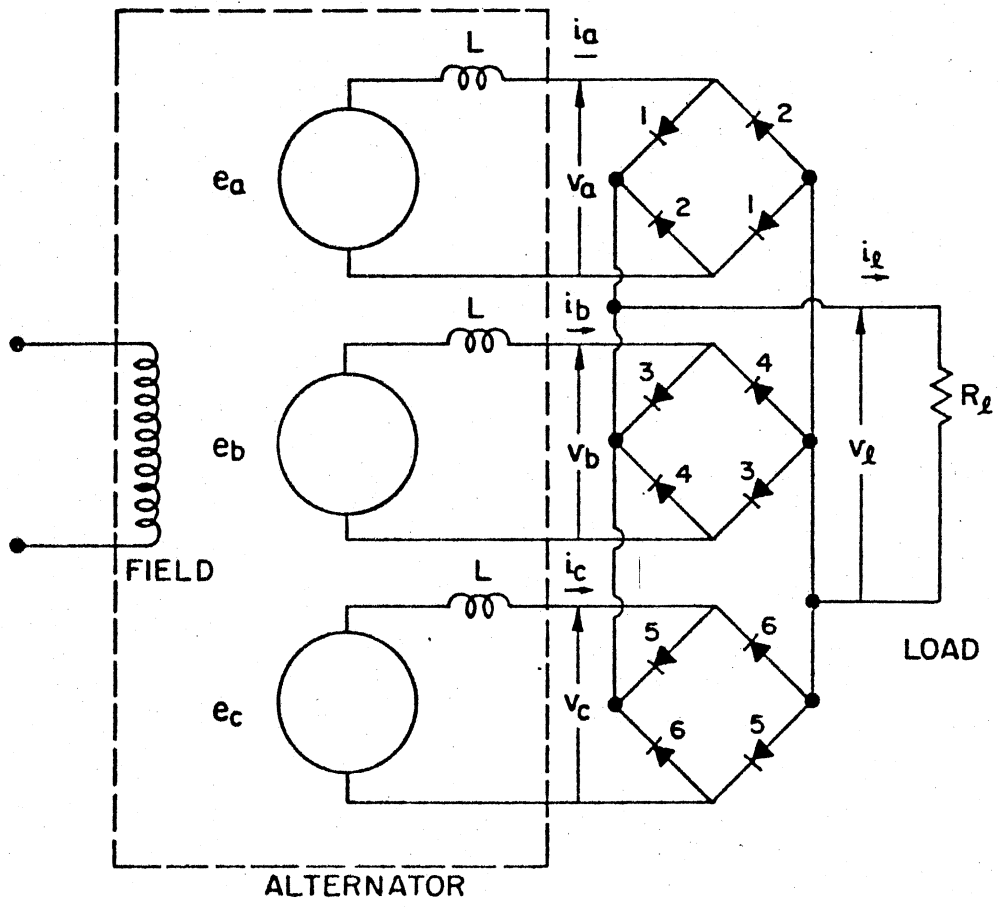

Figure 1. Parallel-Bridge Rectifier System Model

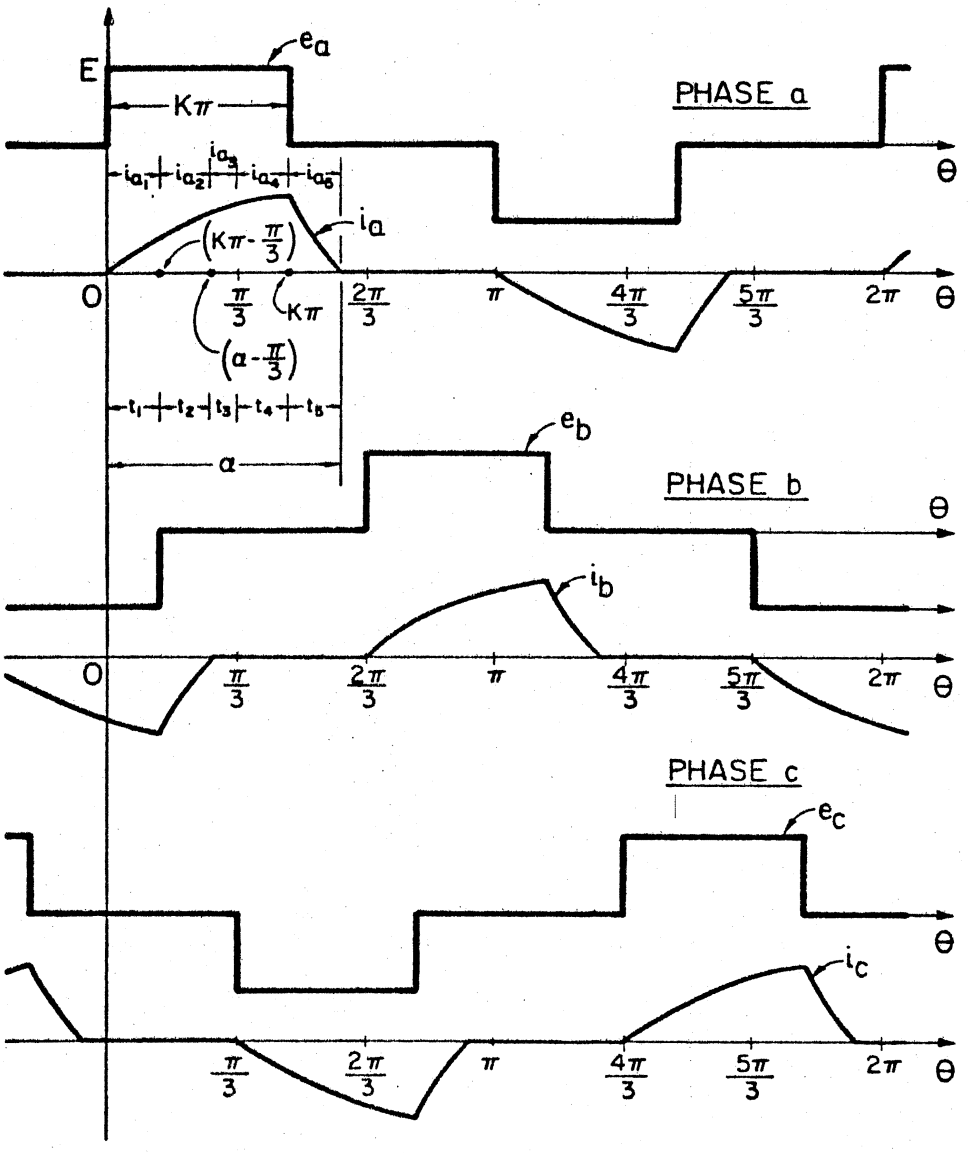

a.) e and i waveforms in the three phases for K=0.4, with conduction angle α.

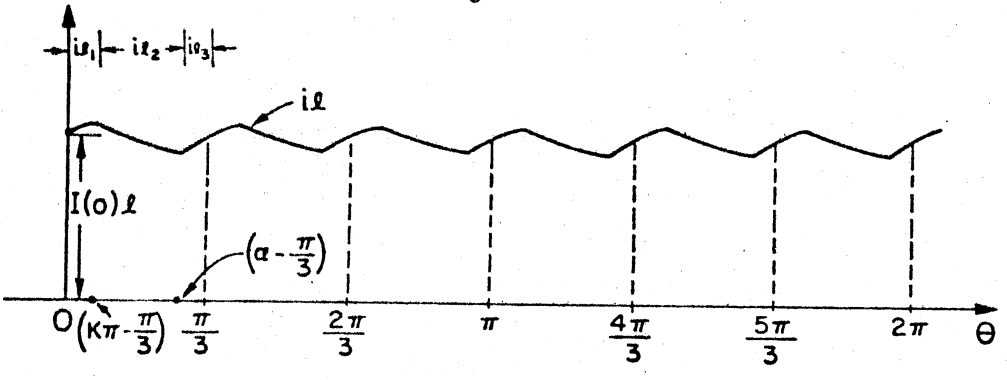

b.) Load current waveform

Figure 2. Voltage and Current Waveforms for Case (i)

width of the input pulse, the energy stored in the commutating inductance, and the voltage across the load. For a given pulse width ratio (K), and for small values of the parameter ratio (X_L/R_ℓ), the conduction duration (α/ω) of each bridge is small. If the parameter ratio (X_L/R_ℓ) is sufficiently large, the conduction of each bridge continues throughout the entire half-cycle, resulting in an effective phase difference β between the source voltage and the phase current. This is shown in Figure 3(a). The general nature of the load current waveform for this case is shown in Figure 3(b). The load current is once again periodic with a period of ($\pi/3$).

The significance of the angles 'α' and 'β' is evident from Figures 2(a) and 3(a). The conduction angle α determines the number of phases conducting simultaneously through the load and the angle β determines the stagger between the zeros of the source voltage and the corresponding phase current for a given circuit parameter ratio (X_L/R_ℓ) and pulse width ratio (K).

In order to determine the relationship between α, β, the circuit parameter ratio (X_L/R_ℓ) and the pulse width ratio (K), it is necessary to consider different ranges of values for angles 'α' and 'β' due to the overlapping of current and voltage waveforms.

Ranges of values for angles 'α' and 'β':

(a) For the range of the pulse width ratio (K) given by $1/3 < K \leq 2/3$, the following ranges for angles α and β exist, requiring separate treatment.

Case (i) $\quad K\pi < \alpha \leq (2\pi/3)$

Case (ii) $\quad (2\pi/3) < \alpha \leq (K\pi + \pi/3)$

Case (iii) $\quad (K\pi + \pi/3) < \alpha \leq \pi$

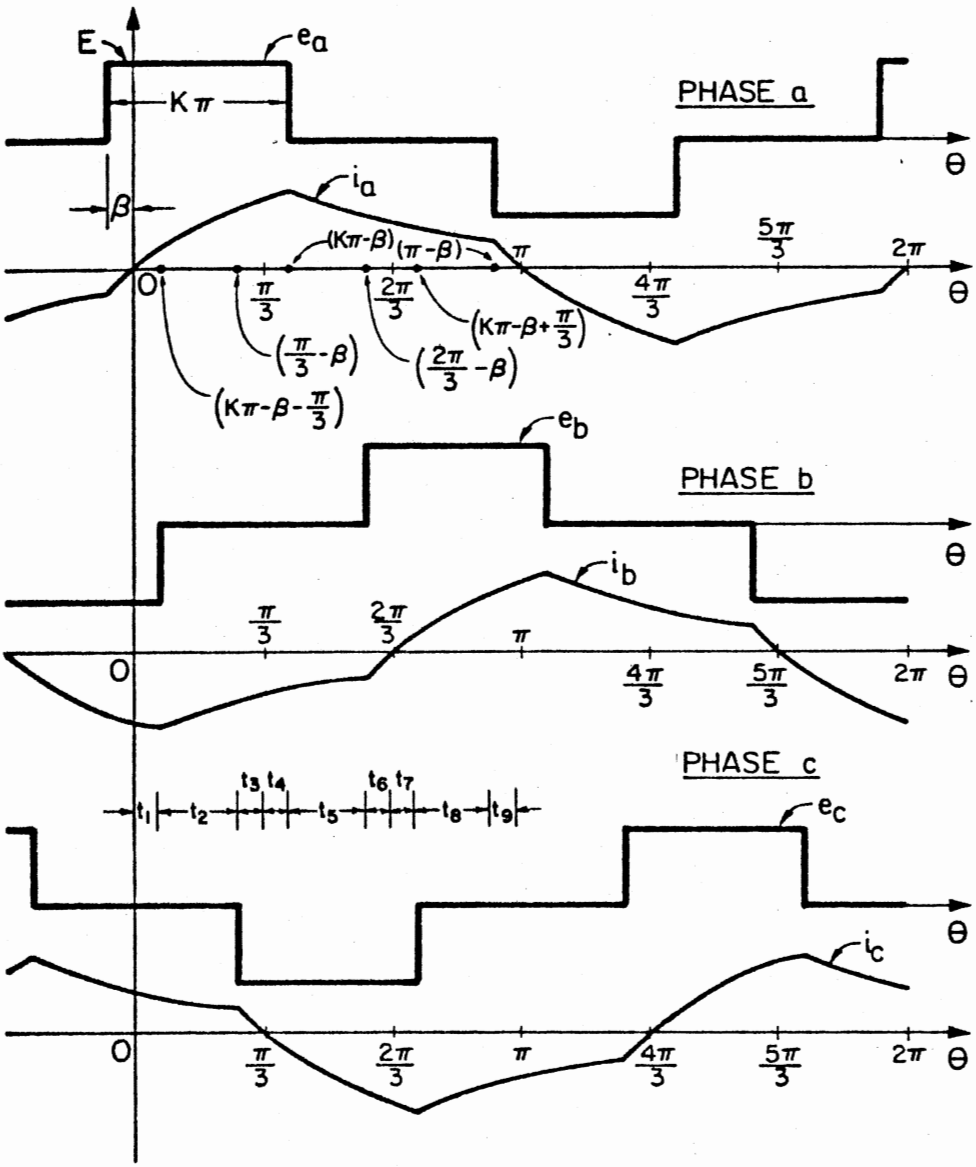

a.) e and i waveforms in the three phases for K=0.4, with angle β shown.

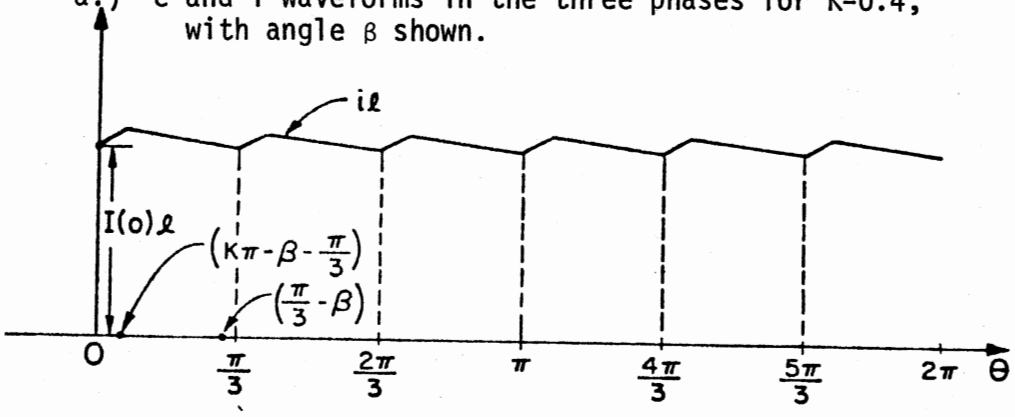

b.) Load current waveform

Figure 3. Voltage and Current Waveforms for Case (iv)

Case (iv) $0 \leq \beta \leq (K\pi - \pi/3)$

Case (v) $(K\pi - \pi/3) < \beta \leq (K\pi/2)$

(b) For the range of the pulse width ratio (K) given by $0 < K \leq 1/3$, the following ranges for angles α and β should be considered.

Case (vi) $K\pi < \alpha \leq (K\pi + \pi/3)$

Case (vii) $(K\pi + \pi/3) < \alpha \leq (2\pi/3)$

Case (viii) $(2\pi/3) < \alpha \leq (K\pi + 2\pi/3)$

Case (ix) $(K\pi + 2\pi/3) < \alpha \leq \pi$

Case (x) $0 \leq \beta \leq (K\pi/2)$

The phase angle 'β' reaches a maximum value of $(K\pi/2)$ when the parameter ratio (X_L/R_ℓ) goes to infinity, corresponding to the short circuit condition. Figure 2(a) corresponds to Case (i) and Figure 3(a) corresponds to Case (iv). Figures 4(a), 5(a), and 6(a) correspond to Cases (ii), (iii), and (v), respectively. The load current waveforms corresponding to these cases are shown in Figures 4(b), 5(b), and 6(b).

Each of the above-mentioned cases need to be analyzed separately in order to derive the relationships between the parameter ratio (X_L/R_ℓ), K and angles α and β, over a range of values for K given by $0 < K \leq 2/3$.

In the next section, only Cases (i) and (iv) with the range for K given by $1/3 < K \leq 2/3$ will be considered in detail. This covers the most useful range for the practical cases of interest. Similar analyses (not detailed here) can be undertaken for the other cases mentioned above. However, the plots for angles α and β are presented to include all the cases mentioned.

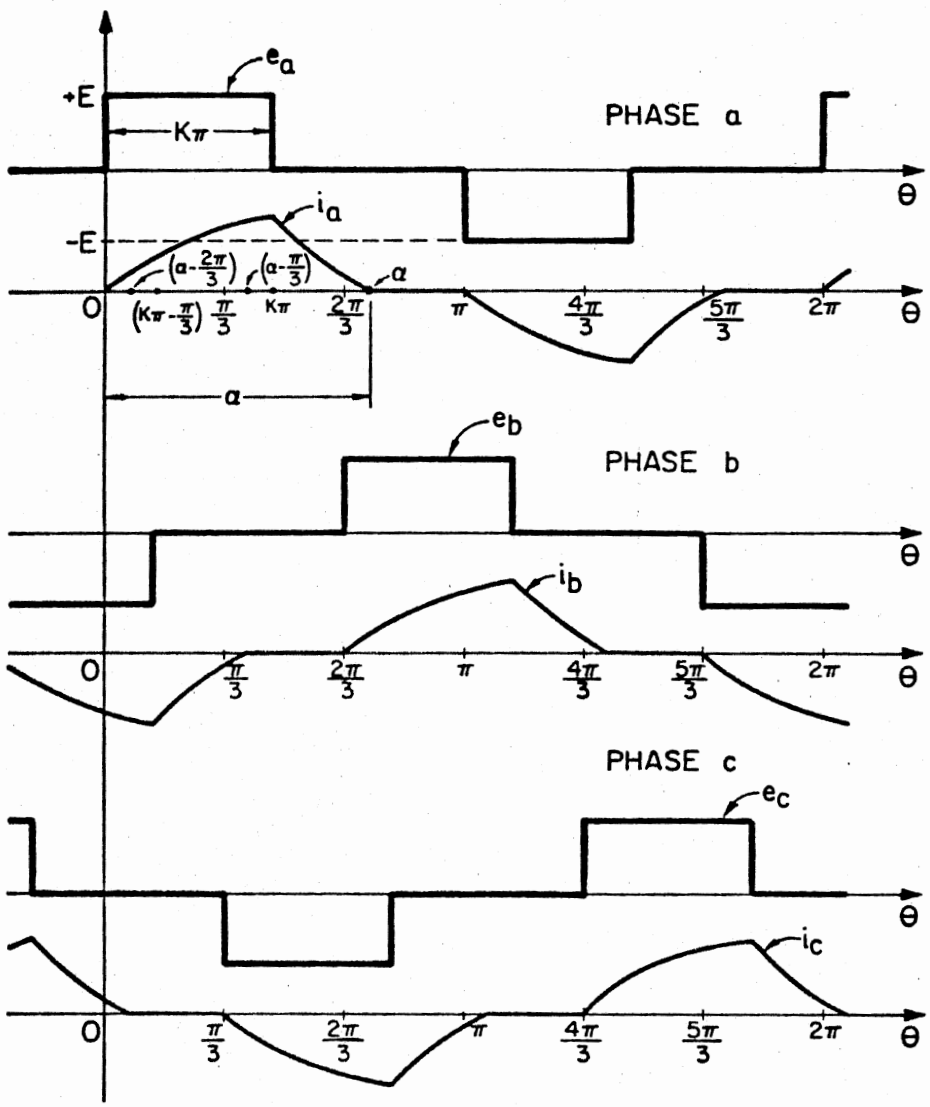

a.) e and i waveforms in the three phases

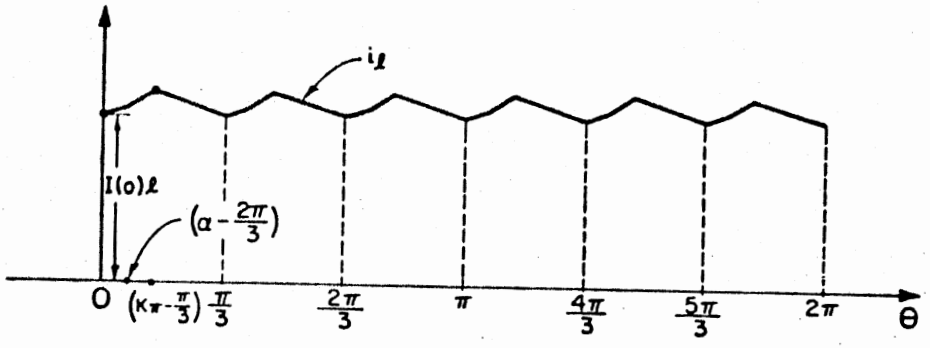

b.) Load current waveform

Figure 4. Voltage and Current Waveforms with K=0.4 for Case (ii)

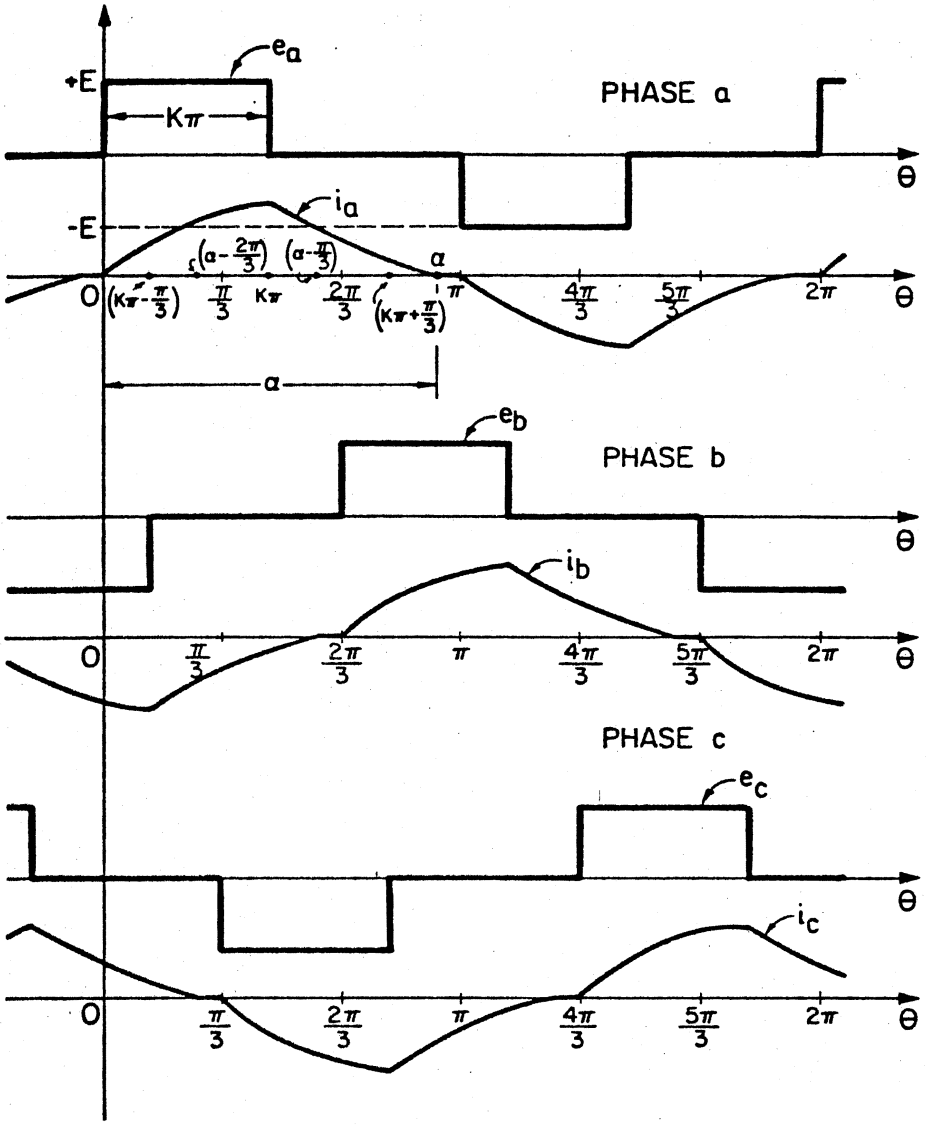

a.) e and i waveforms in the three phases

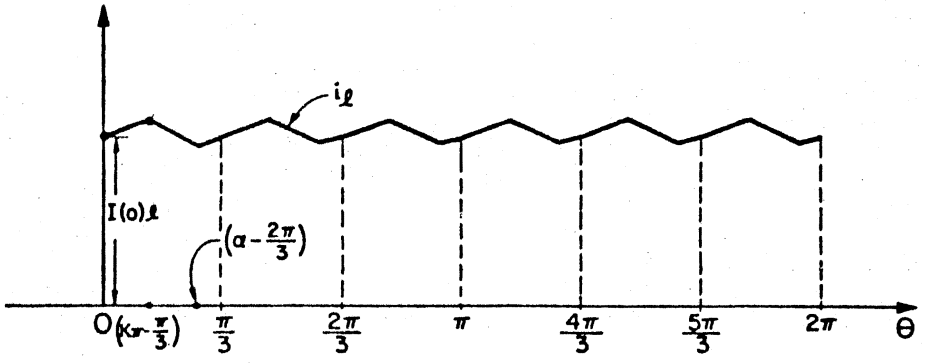

b.) Load current waveform

Figure 5. Voltage and Current Waveforms with K=0.4 for Case (iii)

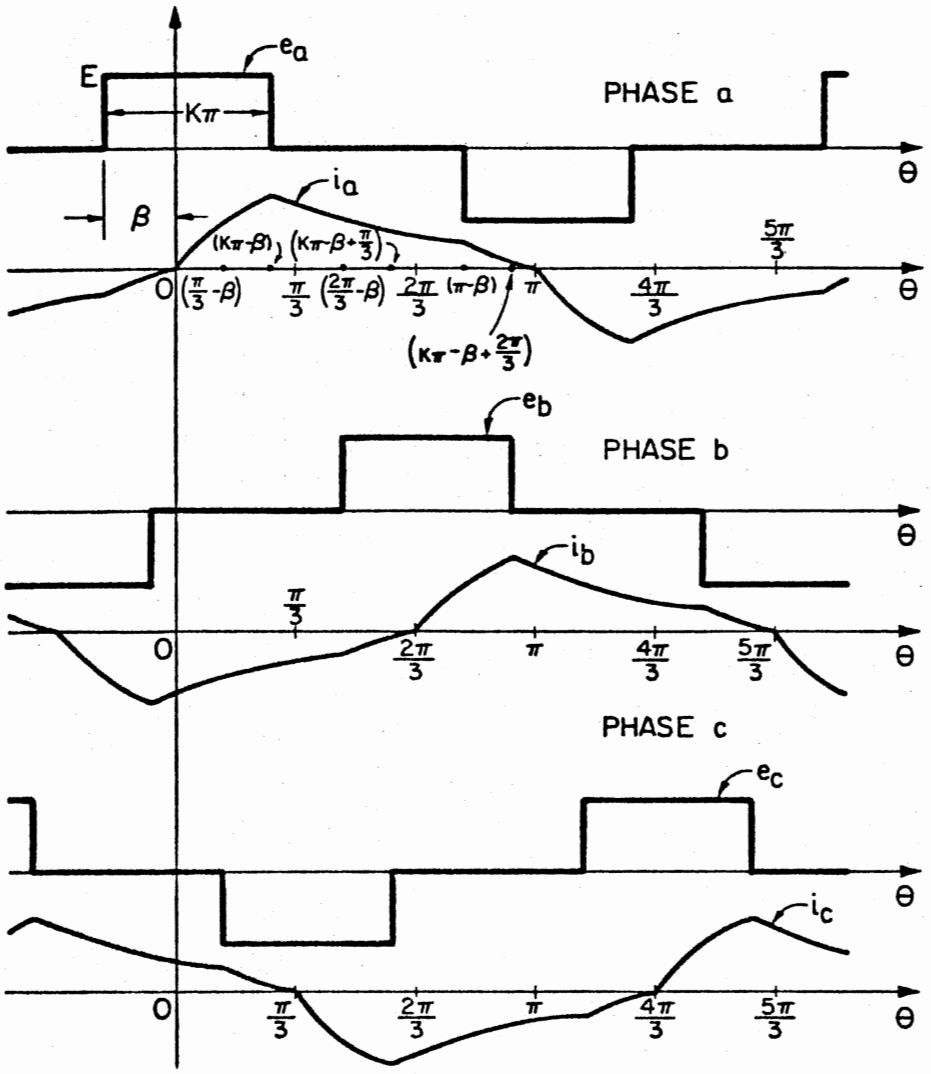

a.) e and i waveforms in the three phases

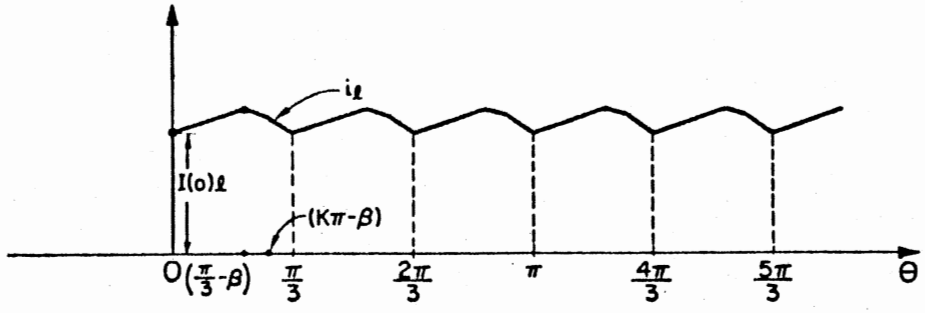

b.) Load current waveform

Figure 6. Voltage and Current Waveforms with K=0.4 for Case (V)

2.3 Circuit Analysis

2.3.1 Case (i) $K\pi < \alpha \leq (2\pi/3)$

Figure 2(a) illustrates the source voltage and source current waveforms for the case under consideration. The conduction duration (α/ω) is divided into five segments and the quantities corresponding to these intervals are designated with subscripts 1 through 5, respectively. As a matter of convenience, the circuit of phase-a is considered. Waveforms for phases b and c will be similar, except for the inherent phase differences of $\pm(2\pi/3)$.

Expressions for load current and phase current will be derived during each of the time intervals t_1 through t_5 with the restriction that there can be no jump in the flow of current through the commutating inductance L. Since the load current is periodic with a period of $(\pi/3)$, the different expressions obtained for load current during this period will be used in the evaluation of the load current during other corresponding durations with a change in the time variable. Time zero is chosen such that at $t = 0^+$, diode pair 1 (see Figure 1) starts conducting.

2.3.1.1 Derivation of the Load Current i_ℓ. During the time interval $0^+ \leq t_1 \leq (K\pi - \pi/3)/\omega$, only the bridges connected to phase-a and phase-b conduct through the load as shown in Figure 2(a). Assuming ideal diodes, circuit equations for phases a and b are given as follows.

$$E - L \frac{di_{a1}}{dt_1} = i_{\ell 1} R_\ell \tag{2.3.1}$$

$$E + L \frac{di_{b1}}{dt_1} = i_{\ell 1} R_\ell \tag{2.3.2}$$

Using the relationship between phase currents and load current, the following differential equation is obtained for $i_{\ell 1}$.

$$\frac{di_{\ell 1}}{dt_1} + \frac{2R_\ell}{L} i_{\ell 1} = \frac{2E}{L} \tag{2.3.3}$$

Solution of (2.3.3) is

$$i_{\ell 1}(t_1) = \frac{E}{R_\ell} + \left(I(0)\ell - \frac{E}{R_\ell}\right) e^{\frac{-2R_\ell t_1}{L}} \tag{2.3.4}$$

where $I(0)\ell$ is the load current at $\omega t_1 = 0$. The load current at $\omega t_1 = (K\pi - \pi/3)$ is given by

$$I_{\ell 1} = \frac{E}{R_\ell} + \left(I(0)\ell - \frac{E}{R_\ell}\right) e^{\frac{-2R_\ell (K\pi - \pi/3)}{\omega L}} \tag{2.3.5}$$

During the interval $(K\pi - \pi/3) \leq \Theta \leq (\alpha - \pi/3)$, define a new time variable t_2 such that

$$\omega t_2 = [\Theta - (K\pi - \pi/3)]$$

and the time interval is now given by $0 \leq t_2 \leq (\alpha - K\pi)/\omega$. Phases a and b conduct through the load during this duration and the new circuit equations are given below.

$$E - L \frac{di_{a2}}{dt_2} = i_{\ell 2} R_\ell \tag{2.3.6}$$

$$0 + L \frac{di_{b2}}{dt_2} = i_{\ell 2} R_\ell \tag{2.3.7}$$

Substituting the relationship between phase currents and load current, the following differential equation is obtained for $i_{\ell 2}$.

$$\frac{di_{\ell 2}}{dt_2} + \frac{2R_\ell}{L} i_{\ell 2} = \frac{E}{L} \tag{2.3.8}$$

Solution of (2.3.8) with the initial condition $i_{\ell 2}(0^+) = I_{\ell 1}$ is

$$i_{\ell 2}(t_2) = \frac{E}{2R_\ell} + \left\{ \frac{E}{2R_\ell} + \left(I(0)_\ell - \frac{E}{R_\ell} \right) e^{\frac{-2R_\ell(K\pi - \pi/3)}{\omega L}} \right\} \cdot e^{\frac{-2R_\ell t_2}{L}} \tag{2.3.9}$$

The load current at $\omega t_2 = (\alpha - K\pi)$ is given by

$$I_{\ell 2} = \frac{E}{2R_\ell} \left[1 + e^{\frac{-2R_\ell(\alpha - K\pi)}{\omega L}} \right] + \left[I(0)_\ell - \frac{E}{R_\ell} \right] e^{\frac{-2R_\ell(\alpha - \pi/3)}{\omega L}} \tag{2.3.10}$$

During the interval $(\alpha - \pi/3) \leq \Theta \leq (\pi/3)$ define another new time variable t_3 such that

$$\omega t_3 = [\Theta - (\alpha - \pi/3)]$$

and the time interval is now given by $0 \leq t_3 \leq (2\pi/3 - \alpha)/\omega$. Only phase-a conducts through the load during this period and the circuit equation is

$$E - L \frac{di_{a3}}{dt_3} = i_{\ell 3} R_\ell \tag{2.3.11}$$

Using the relationship between phase current and load current, the following differential equation is obtained for $i_{\ell 3}$.

$$\frac{di_{\ell 3}}{dt_3} + \frac{R_\ell}{L} i_{\ell 3} = \frac{E}{L} \tag{2.3.12}$$

Solution of (2.3.12) with the initial condition $i_{\ell 3}(0^+) = I_{\ell 2}$ is

$$i_{\ell 3}(t_3) = \frac{E}{R_\ell} + \left[\frac{-E}{2R_\ell} + \frac{E}{2R_\ell} e^{\frac{-2R_\ell(\alpha - K\pi)}{\omega L}} + \left(I(0)_\ell - \frac{E}{R_\ell} \right) e^{\frac{-2R_\ell(\alpha - \pi/3)}{\omega L}} \right] \cdot e^{\frac{-R_\ell t_3}{L}} \tag{2.3.13}$$

The load current at $\omega t_3 = (2\pi/3 - \alpha)$ is given by

$$I_{\ell 3} = \frac{E}{R_\ell} - \frac{E}{2R_\ell} e^{\frac{-R_\ell(2\pi/3 - \alpha)}{\omega L}} + \frac{E}{2R_\ell} e^{\frac{-R_\ell(\alpha - 2K\pi + 2\pi/3)}{\omega L}} + \left(I(0)_\ell - \frac{E}{R_\ell} \right) e^{\frac{-R_\ell \alpha}{\omega L}} \tag{2.3.14}$$

Due to the symmetry of the input voltage and phase current waveforms, the load current i_ℓ is periodic with a period of $(\pi/3)$. Therefore the load current at $\Theta = (\pi/3)$ should be equal to the load current at

$\Theta = 0$. Equating $I_{\ell 3}$ given by (2.3.14) to $I(0)_\ell$, an expression for the load current at $\Theta = 0$ is obtained.

$$I(0)_\ell = \frac{E}{2R_\ell} \cdot \left[\frac{2 - e^{\frac{R_\ell(\alpha - 2\pi/3)}{\omega L}} + e^{\frac{R_\ell(2K\pi - 2\pi/3 - \alpha)}{\omega L}} - 2e^{\frac{-R_\ell \alpha}{\omega L}}}{1 - e^{\frac{-R_\ell \alpha}{\omega L}}} \right] \tag{2.3.15}$$

2.3.1.2 Derivation of Phase Current i_a. At $t = 0^+$, phase-a circuit starts conducting through the load with zero initial current in the inductor as shown in Figure 2(a). During the time interval $0^+ \leq t_1 \leq (K\pi - \pi/3)/\omega$, the circuit equation for phase-a is

$$E - L \frac{di_{a1}}{dt_1} = i_{\ell 1} R_\ell \tag{2.3.16}$$

Substituting for $i_{\ell 1}$ from equation (2.3.4) into (2.3.16) and solving for i_{a1} with the initial condition $i_{a1} = 0$ at $\omega t_1 = 0$ yields

$$i_{a1}(t_1) = \left(\frac{E}{2R_\ell} - \frac{I(0)_\ell}{2} \right) \left(1 - e^{\frac{-2R_\ell}{L} t_1} \right) \tag{2.3.17}$$

The phase-a current at $\omega t_1 = (K\pi - \pi/3)$ is given by

$$I_{a1} = \left(\frac{E}{2R_\ell} - \frac{I(0)_\ell}{2} \right) \left(1 - e^{\frac{-2R_\ell}{\omega L} (K\pi - \pi/3)} \right) \tag{2.3.18}$$

During the time interval $0 \leq t_2 \leq (\alpha - K\pi)/\omega$ the circuit equation for phase-a is

$$E - L\frac{di_{a2}}{dt_2} = i_{\ell 2} R_\ell \tag{2.3.19}$$

Substituting for $i_{\ell 2}$ from (2.3.9) into (2.3.19), the solution for i_{a2} with the initial condition $i_{a2}(0^+) = I_{a1}$ is obtained as

$$i_{a2}(t_2) = \frac{Et_2}{2L} + \frac{E}{4R_\ell} - \frac{I(0)\ell}{2} + \left\{ \frac{E}{4R_\ell} + \left(\frac{I(0)\ell}{2} - \frac{E}{2R_\ell} \right) e^{\frac{-2R_\ell(K\pi - \pi/3)}{\omega L}} \right\} \cdot e^{\frac{-2R_\ell t_2}{L}} \tag{2.3.20}$$

The phase-a current at $\omega t_2 = (\alpha - K\pi)$ is

$$I_{a2} = \frac{E(\alpha - K\pi)}{2L\omega} + \frac{E}{4R_\ell} - \frac{I(0)\ell}{2} + \left\{ \frac{E}{4R_\ell} e^{\frac{-2R_\ell(\alpha - K\pi)}{\omega L}} + \left(\frac{I(0)\ell}{2} - \frac{E}{2R_\ell} \right) e^{\frac{-2R_\ell(\alpha - \pi/3)}{\omega L}} \right\} \tag{2.3.21}$$

During the time interval $0 \leq t_3 \leq (2\pi/3 - \alpha)/\omega$, the circuit equation for phase-a is

$$E - L\frac{di_{a3}}{dt_3} = i_{\ell 3} R_\ell \tag{2.3.22}$$

Substituting for $i_{\ell 3}$ from (2.3.13) into (2.3.22), the solution for i_{a3}

with the initial condition $i_{a3}(0^+) = I_{a2}$ is

$$i_{a3}(t_3) = \frac{E(\alpha - K\pi)}{2L\omega} + \frac{E}{4R_\ell}\left(1 - e^{\frac{-2R_\ell(\alpha - K\pi)}{\omega L}}\right)$$

$$+ \left(\frac{E}{2R_\ell} - \frac{I(0)\ell}{2}\right)\left[1 + e^{\frac{-2R_\ell(\alpha - \pi/3)}{\omega L}}\right]$$

$$+ \left[\frac{-E}{2R_\ell} + \left\{\frac{E}{2R_\ell} e^{\frac{-2R_\ell(\alpha - K\pi)}{\omega L}}\right.\right.$$

$$\left.\left. + \left(I(0)\ell - \frac{E}{R_\ell}\right) e^{\frac{-2R_\ell(\alpha - \pi/3)}{\omega L}}\right\}\right] e^{\frac{-R_\ell t_3}{L}}$$

(2.3.23)

The phase-a current at $\omega t_3 = (2\pi/3 - \alpha)$ is given by

$$I_{a3} = \frac{E(\alpha - K\pi)}{2L\omega} + \frac{E}{4R_\ell}\left(1 - e^{\frac{-2R_\ell(\alpha - K\pi)}{\omega L}}\right)$$

$$+ \left(\frac{E}{2R_\ell} - \frac{I(0)\ell}{2}\right)\left[1 + e^{\frac{-2R_\ell(\alpha - \pi/3)}{\omega L}} - 2\, e^{\frac{-R_\ell \alpha}{\omega L}}\right]$$

$$+ \frac{E}{2R_\ell}\left[e^{\frac{-R_\ell(\alpha - 2K\pi + 2\pi/3)}{\omega L}} - e^{\frac{-R_\ell(2\pi/3 - \alpha)}{\omega L}}\right]$$

(2.3.24)

During the time interval $0 \leq t_4 \leq (K\pi - \pi/3)/\omega$ the circuit equation for phase-a is

$$E - L\frac{di_{a4}}{dt_4} = i_{\ell 4} R_\ell \qquad (2.3.25)$$

Due to the periodicity of the load current, the expression for $i_{\ell 4}$ is the same as $i_{\ell 1}$, with a change in time variable from t_1 to t_4. Substituting for $i_{\ell 4}$ in (2.3.25), the solution for i_{a4} with the initial condition $i_{a4}(0^+) = I_{a3}$ is

$$\begin{aligned} i_{a4}(t_4) = & \left(\frac{E}{2R_\ell} - \frac{I(0)_\ell}{2}\right) \\ & \cdot\left(2 + e^{\frac{-2R_\ell(\alpha - \pi/3)}{\omega L}} - e^{\frac{-2R_\ell t_4}{L}} - 2e^{\frac{-R_\ell \alpha}{\omega L}}\right) \\ & + \frac{E(\alpha - K\pi)}{2L\omega} + \frac{E}{4R_\ell}\left(1 - e^{\frac{-2R_\ell(\alpha - K\pi)}{\omega L}}\right) \\ & + \frac{E}{2R_\ell}\left[e^{\frac{-R_\ell(\alpha - 2K\pi + 2\pi/3)}{\omega L}} - e^{\frac{-R_\ell(2\pi/3 - \alpha)}{\omega L}}\right] \end{aligned} \qquad (2.3.26)$$

The phase-a current at $\omega t_4 = (K\pi - \pi/3)$ is given by

$$\begin{aligned} I_{a4} = & \left(\frac{E}{2R_\ell} - \frac{I(0)_\ell}{2}\right) \\ & \cdot\left[2 + e^{\frac{-2R_\ell(\alpha - \pi/3)}{\omega L}} - e^{\frac{-2R_\ell(K\pi - \pi/3)}{\omega L}} - 2e^{\frac{-R_\ell \alpha}{\omega L}}\right] \\ & + \frac{E(\alpha - K\pi)}{2L\omega} + \frac{E}{4R_\ell}\left(1 - e^{\frac{-2R_\ell(\alpha - K\pi)}{\omega L}}\right) \end{aligned}$$

$$+ \frac{E}{2R_\ell}\left[e^{\frac{-R_\ell(\alpha - 2K\pi + 2\pi/3)}{\omega L}} - e^{\frac{-R_\ell(2\pi/3 - \alpha)}{\omega L}}\right] \tag{2.3.27}$$

During the time interval $0 \leq t_5 \leq (\alpha - K\pi)/\omega$, the circuit equation for phase-a is

$$0 - L\frac{di_{a5}}{dt_5} = i_{\ell 5} R_\ell \tag{2.3.28}$$

The expression for load current $i_{\ell 5}$ is obtained from (2.3.9) by replacing t_2 with t_5. Substituting for $i_{\ell 5}$ in (2.3.28), the solution for i_{a5} with initial condition $i_{a5}(0^+) = I_{a4}$ is

$$\begin{aligned} i_{a5}(t_5) = {} & \frac{-Et_5}{2L} \\ & + \left\{\frac{E}{4R_\ell} + \left(\frac{I(0)\ell}{2} - \frac{E}{2R_\ell}\right)e^{\frac{-2R_\ell(K\pi - \pi/3)}{\omega L}}\right\} e^{\frac{-2R_\ell t_5}{L}} \\ & + \frac{E}{2R_\ell}\left[e^{\frac{-R_\ell(\alpha - 2K\pi + 2\pi/3)}{\omega L}} - e^{\frac{-R_\ell(2\pi/3 - \alpha)}{\omega L}}\right] \\ & + \left(\frac{E}{2R_\ell} - \frac{I(0)\ell}{2}\right)\left[2 - 2e^{\frac{-R_\ell\alpha}{\omega L}} + e^{\frac{-2R_\ell(\alpha - \pi/3)}{\omega L}}\right] \\ & + \frac{E(\alpha - K\pi)}{2L\omega} - \frac{E}{4R_\ell} e^{\frac{-2R_\ell(\alpha - K\pi)}{\omega L}} \end{aligned} \tag{2.3.29}$$

The phase-a current I_{a5} at $\omega t_5 = (\alpha - K\pi)$, obtained by substituting for $I(0)\ell$ from (2.3.15) is equal to zero. This satisfies the requirement that at $\Theta = \alpha$; $i_{a5} = 0$.

2.3.1.3 Evaluation of Angle 'α'. The load current $I(0)_\ell$ at $\omega t_1 = 0$ is represented in Figure 2(a) by

$$I(0)_\ell = -i_{b1}(0^+) \tag{2.3.30}$$

From the symmetry of the circuit, it is observed from Figure 2(a) that

$$-i_{b1}(0^+) = I_{a3} \tag{2.3.31}$$

Equating the expressions for currents obtained in Equations (2.3.15) and (2.3.24), a transcendental expression involving α, the circuit parameter ratio (X_L/R_ℓ) and K is obtained as follows.

$$3 = e^{\frac{R_\ell(\alpha - 2\pi/3)}{\omega L}} - e^{\frac{2R_\ell(K\pi - \alpha)}{\omega L}} + \frac{2R_\ell\alpha}{\omega L} - \frac{2R_\ell K\pi}{\omega L} + \left(4 + \frac{2R_\ell K\pi}{\omega L} - \frac{2R_\ell\alpha}{\omega L} - e^{\frac{-2R_\ell(K\pi - \pi/3)}{\omega L}}\right) e^{\frac{-R_\ell\alpha}{\omega L}} \tag{2.3.32}$$

The non-linear algebraic equation (2.3.32) involving angle α is solved for different parameter ratios (X_L/R_ℓ) and K by an iterative process on an IBM 370 digital computer. The value of K is varied between (1/3) and (2/3). A set of values for angle α is obtained by varying the ratio (X_L/R_ℓ) for each value of K chosen. Since the equations in this case are valid for the range of α given by $K\pi < \alpha \leq (2\pi/3)$, the maximum value α can have in each iteration is limited to $(2\pi/3)$.

A similar procedure is followed for the evaluation of conduction angle 'α' for different ranges of K and α, as mentioned earlier. The maximum value of conduction angle α is obviously equal to π.

Theoretical values of α are presented in Figure 7 as a family of curves for different parameter ratios (X_L/R_ℓ) and K.

The waveforms of phase-a bridge input voltage v_a, phase current i_a and load current i_ℓ for K = 0.4, (X_L/R_ℓ) = 0.5 and angle α = 107.18° are plotted in Figure 8.

2.3.2 Case (iv) $0 \leq \beta \leq (K\pi - \pi/3)$

Figure 3(a) shows the source voltage and source current waveforms in the three phases for this case. The conduction duration of each bridge is divided into nine segments and the quantities corresponding to these intervals are designated with subscripts 1 through 9, respectively. As a matter of convenience, the half-cycle corresponding to phase-a is considered. Waveforms for phases b and c will be similar except for the inherent phase differences of $\pm(2\pi/3)$.

Expressions for load current and phase current will be derived during each of the time intervals t_1 through t_9 while maintaining a smooth flow of current through the inductance L. Time zero is chosen such that at $t = 0^+$, diode pair 2 stops conducting and diode pair 1 starts conducting.

2.3.2.1 Derivation of the Load Current i_ℓ. During the time interval $0^+ \leq t_1 \leq (K\pi - \beta - \pi/3)/\omega$, bridges across phases a, b, and c conduct through the load as shown in Figure 3(a). Assuming ideal diodes, circuit equations for phases a, b, and c are given as follows.

$$E - L \frac{di_{a1}}{dt_1} = i_{\ell 1} R_\ell \qquad (2.3.33)$$

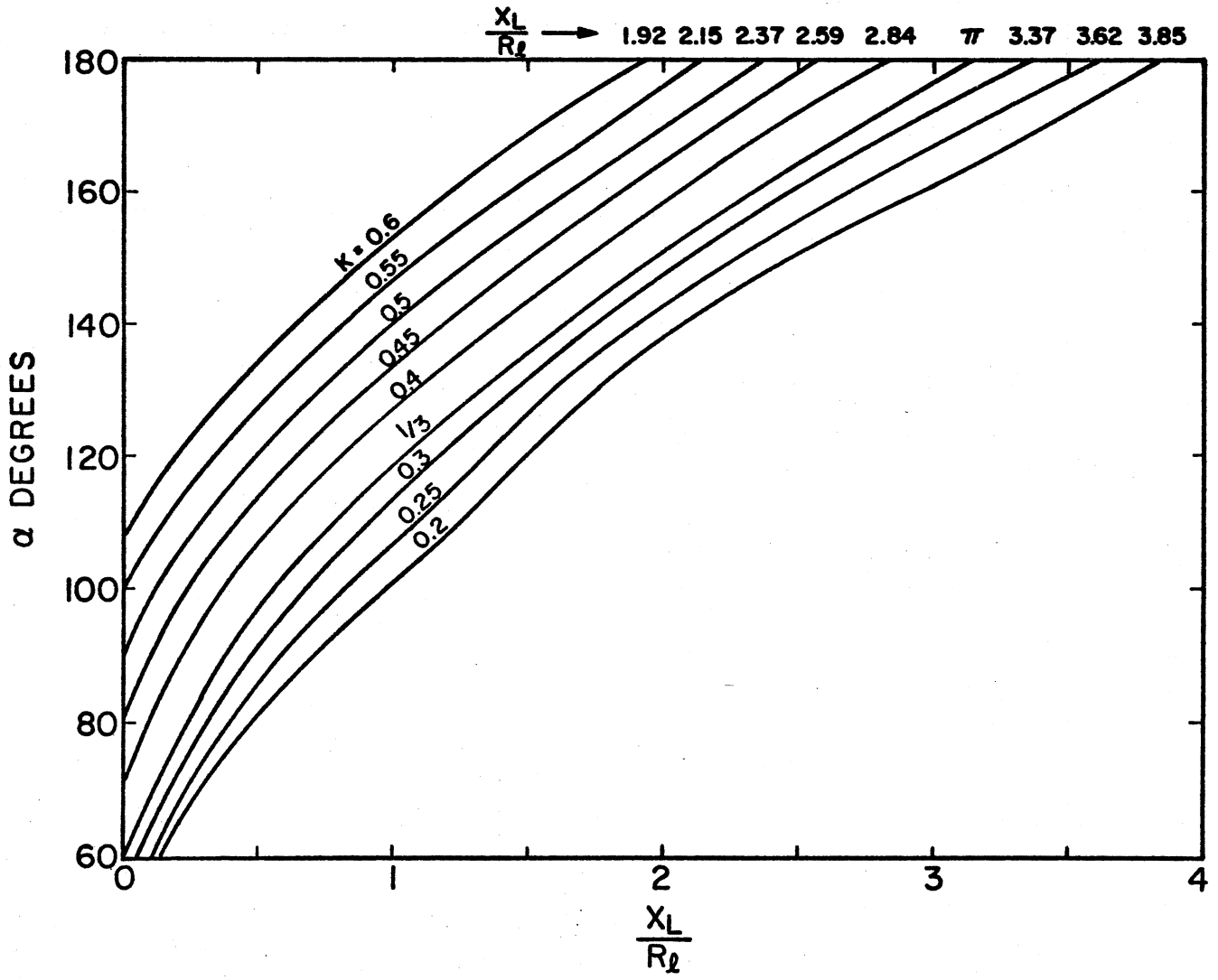

Figure 7. Theoretical Values of α

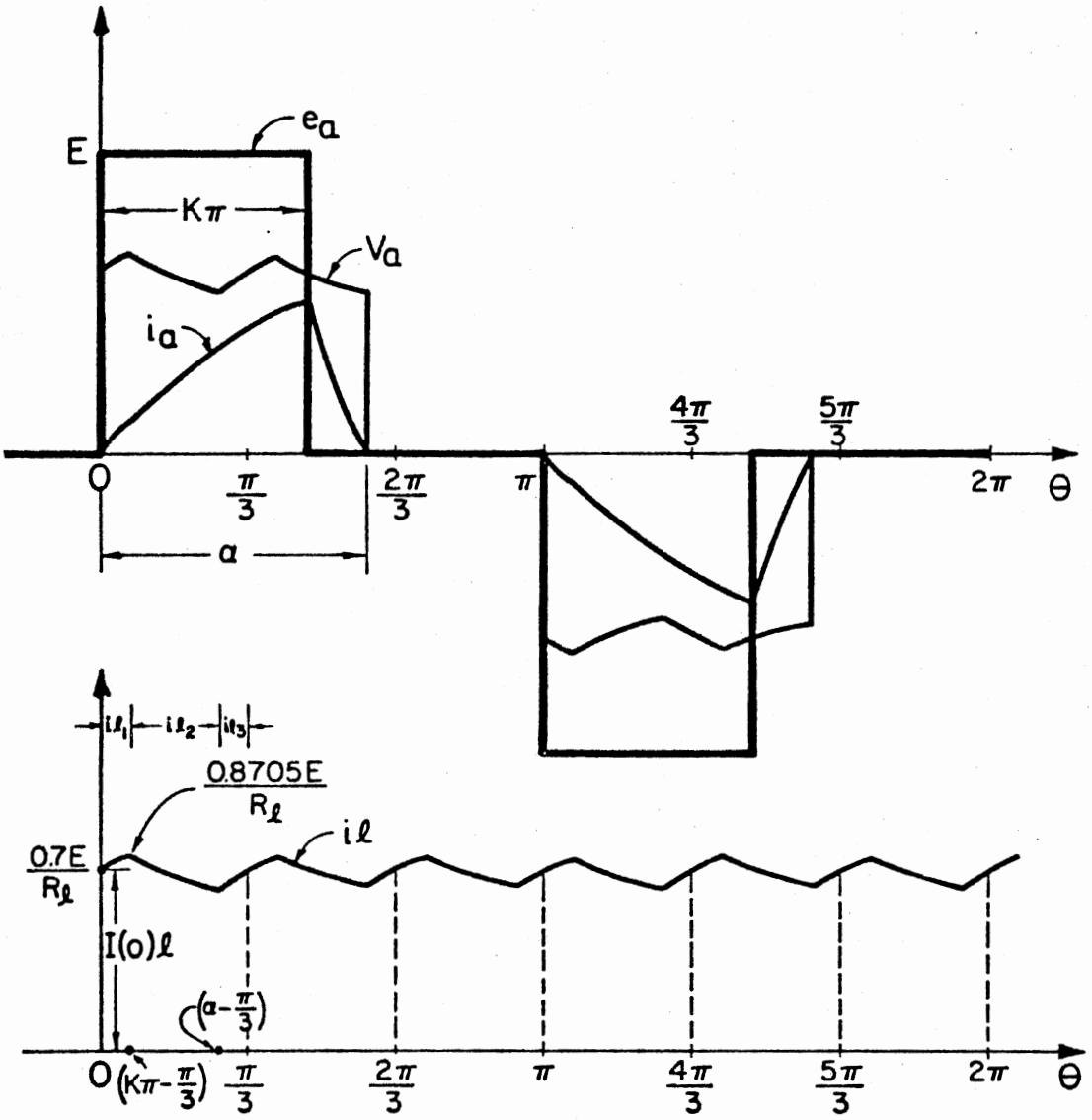

Figure 8. e_a, v_a, i_a and i_ℓ Waveforms for K= 0.4, (X_L/R_ℓ)=0.5 and α = 107.18°

$$E + L \frac{di_{b1}}{dt_1} = i_{\ell 1} R_\ell \tag{2.3.34}$$

$$0 - L \frac{di_{c1}}{dt_1} = i_{\ell 1} R_\ell \tag{2.3.35}$$

Using the relationship between phase currents and load current, the following differential equation is obtained for $i_{\ell 1}$.

$$\frac{di_{\ell 1}}{dt_1} + \frac{3R_\ell}{L} i_{\ell 1} = \frac{2E}{L} \tag{2.3.36}$$

Solution of (2.3.36) is

$$i_{\ell 1}(t_1) = \frac{2E}{3R_\ell} + \left(I(0)\ell - \frac{2E}{3R_\ell} \right) e^{\frac{-3R_\ell t_1}{L}} \tag{2.3.37}$$

in which $I(0)\ell$ is the load current at $\omega t_1 = 0$.

The load current at $\omega t_1 = (K\pi - \beta - \pi/3)$ is

$$I_{\ell 1} = \frac{2E}{3R_\ell} + \left(I(0)\ell - \frac{2E}{3R_\ell} \right) e^{\frac{-3R_\ell (K\pi - \beta - \pi/3)}{\omega L}} \tag{2.3.38}$$

During the interval $(K\pi - \beta - \pi/3) \leq \Theta \leq (\pi/3 - \beta)$ define a new time variable t_2 such that

$$\omega t_2 = [\Theta - (K\pi - \beta - \pi/3)]$$

with the time interval given by $0 \leq t_2 \leq (2\pi/3 - K\pi)/\omega$. The circuit equations for phases a, b, and c during this time interval are

$$E - L \frac{di_{a2}}{dt_2} = i_{\ell 2} R_\ell \tag{2.3.39}$$

$$0 + L \frac{di_{b2}}{dt_2} = i_{\ell 2} R_\ell \tag{2.3.40}$$

$$0 - L \frac{di_{c2}}{dt_2} = i_{\ell 2} R_\ell \tag{2.3.41}$$

Substituting the relationship between phase currents and load current, the following differential equation is obtained for $i_{\ell 2}$.

$$\frac{di_{\ell 2}}{dt_2} + \frac{3R_\ell}{L} i_{\ell 2} = \frac{E}{L} \tag{2.3.42}$$

Solution of (2.3.42) with the initial condition $i_{\ell 2}(0^+) = I_{\ell 1}$ yields

$$i_{\ell 2}(t_2) = \frac{E}{3R_\ell} + \left\{ \frac{E}{3R_\ell} + \left(I(0)_\ell - \frac{2E}{3R_\ell} \right) e^{\frac{-3R_\ell (K\pi - \beta - \pi/3)}{\omega L}} \right\} \cdot e^{\frac{-3R_\ell t_2}{L}} \tag{2.3.43}$$

The load current at $\omega t_2 = (2\pi/3 - K\pi)$ is

$$I_{\ell 2} = \frac{E}{3R_\ell} \left(1 + e^{\frac{-3R_\ell (2\pi/3 - K\pi)}{\omega L}} \right) + \left(I(0)_\ell - \frac{2E}{3R_\ell} \right) e^{\frac{-3R_\ell (\pi/3 - \beta)}{\omega L}} \tag{2.3.44}$$

During the interval $(\pi/3 - \beta) \leq \Theta \leq (\pi/3)$ define a time variable t_3 such that

$$\omega t_3 = [\theta - (\pi/3 - \beta)]$$

with the time interval given by $0 \leq t_3 \leq (\beta/\omega)$. The circuit equations for phases a, b, and c during this time interval are

$$E - L \frac{di_{a3}}{dt_3} = i_{\ell 3} R_\ell \tag{2.3.45}$$

$$0 + L \frac{di_{b3}}{dt_3} = i_{\ell 3} R_\ell \tag{2.3.46}$$

$$-E - L \frac{di_{c3}}{dt_3} = i_{\ell 3} R_\ell \tag{2.3.47}$$

Using the relationship between phase currents and load current, the following differential equation is obtained for $i_{\ell 3}$.

$$\frac{di_{\ell 3}}{dt_3} + \frac{3R_\ell}{L} i_{\ell 3} = 0 \tag{2.3.48}$$

Solution of (2.3.48) with the initial condition $i_{\ell 3}(0^+) = I_{\ell 2}$ yields

$$i_{\ell 3}(t_3) = \left[\frac{E}{3R_\ell} + \left(\frac{E}{3R_\ell} \right) e^{\frac{-3R_\ell(2\pi/3 - K\pi)}{\omega L}} + \left(I(0)_\ell - \frac{2E}{3R_\ell} \right) e^{\frac{-3R_\ell(\pi/3 - \beta)}{\omega L}} \right] e^{\frac{-3R_\ell t_3}{L}} \tag{2.3.49}$$

The load current at $\omega t_3 = \beta$ is given by

$$I_{\ell 3} = \frac{E}{3R_\ell}\left[e^{\frac{-3R_\ell\beta}{\omega L}} + e^{\frac{-3R_\ell(2\pi/3 - K\pi + \beta)}{\omega L}}\right]$$

$$+ \left(I(0)_\ell - \frac{2E}{3R_\ell}\right) e^{\frac{-R_\ell\pi}{\omega L}} \qquad (2.3.50)$$

Due to symmetry, the load current at $\Theta = 0$ should be equal to the load current at $\Theta = (\pi/3)$. Equating $I_{\ell 3}$ given by (2.3.50) to $I(0)_\ell$, an expression for the load current at $\Theta = 0$ is obtained.

$$I(0)_\ell = \left(\frac{E}{3R_\ell}\right) \cdot \frac{\left[e^{\frac{-3R_\ell\beta}{\omega L}} + e^{\frac{-3R_\ell(2\pi/3 - K\pi + \beta)}{\omega L}} - 2e^{\frac{-R_\ell\pi}{\omega L}}\right]}{\left(1 - e^{\frac{-R_\ell\pi}{\omega L}}\right)} \qquad (2.3.51)$$

2.3.2.2 Derivation of Phase Current i_a. At $t = 0^+$, diode pair 2 stops conducting and diode pair 1 starts conducting with zero initial current in L as shown in Figure 3(a). During the time interval $0^+ \leq t_1 \leq (K\pi - \beta - \pi/3)/\omega$, the circuit equation for phase-a is

$$E - L\frac{di_{a1}}{dt_1} = i_{\ell 1} R_\ell \qquad (2.3.52)$$

Substituting for $i_{\ell 1}$ from (2.3.37) into (2.3.52) and solving for i_{a1} with the initial condition $i_{a1} = 0$ at $\omega t_1 = 0$ gives

$$i_{a1}(t_1) = \frac{Et_1}{3L} + \left[\frac{2E}{9R_\ell} - \frac{I(0)\ell}{3}\right]\left(1 - e^{\frac{-3R_\ell t_1}{L}}\right) \quad (2.3.53)$$

The phase-a current at $\omega t_1 = (K\pi - \beta - \pi/3)$ is given by

$$I_{a1} = \frac{E(K\pi - \beta - \pi/3)}{3L\omega} + \left[\frac{2E}{9R_\ell} - \frac{I(0)\ell}{3}\right]\left(1 - e^{\frac{-3R_\ell(K\pi - \beta - \pi/3)}{\omega L}}\right) \quad (2.3.54)$$

During the time interval $0 \leq t_2 \leq (2\pi/3 - K\pi)/\omega$, the circuit equation for phase-a is

$$E - L\frac{di_{a2}}{dt_2} = i_{\ell 2} R_\ell \quad (2.3.55)$$

Substituting for $i_{\ell 2}$ from (2.3.43) into (2.3.55), the solution for i_{a2} with the initial condition $i_{a2}(0^+) = I_{a1}$ is given by

$$i_{a2}(t_2) = \frac{2Et_2}{3L} + \left\{\frac{E}{9R_\ell} + \left(\frac{I(0)\ell}{3} - \frac{2E}{9R_\ell}\right)e^{\frac{-3R_\ell(K\pi - \beta - \pi/3)}{\omega L}}\right\} \cdot e^{\frac{-3R_\ell t_2}{L}} + \frac{E(K\pi - \beta - \pi/3)}{3L\omega} + \frac{E}{9R_\ell} - \frac{I(0)\ell}{3} \quad (2.3.56)$$

The phase-a current at $\omega t_2 = (2\pi/3 - K\pi)$ is given by

$$I_{a2} = \frac{E(\pi - K\pi - \beta)}{3L\omega} + \frac{E}{9R_\ell} - \frac{I(0)\ell}{3}$$

$$+ \left(\frac{E}{9R_\ell}\right) e^{\frac{-3R_\ell(2\pi/3 - K\pi)}{\omega L}}$$

$$+ \left(\frac{I(0)\ell}{3} - \frac{2E}{9R_\ell}\right) e^{\frac{-3R_\ell(\pi/3 - \beta)}{\omega L}} \qquad (2.3.57)$$

During the time interval $0 \leq t_3 \leq (\beta/\omega)$, the circuit equation for phase-a is

$$E - L\frac{di_{a3}}{dt_3} = i_{\ell 3} R_\ell \qquad (2.3.58)$$

Substituting for $i_{\ell 3}$ from (2.3.49) into (2.3.58), the solution for i_{a3} with the initial condition $i_{a3}(0^+) = I_{a2}$ is given by

$$i_{a3}(t_3) = \frac{Et_3}{L}$$

$$+ \left[\frac{E}{9R_\ell} + \left(\frac{E}{9R_\ell}\right) e^{\frac{-3R_\ell(2\pi/3 - K\pi)}{\omega L}}\right.$$

$$\left. + \left(\frac{I(0)\ell}{3} - \frac{2E}{9R_\ell}\right) e^{\frac{-3R_\ell(\pi/3 - \beta)}{\omega L}}\right] e^{\frac{-3R_\ell t_3}{L}}$$

$$+ \frac{E(\pi - K\pi)}{3L\omega} - \frac{I(0)\ell}{3} - \frac{E\beta}{3L\omega} \qquad (2.3.59)$$

The phase-a current at $\omega t_3 = \beta$ is given by

$$I_{a3} = \frac{E}{3\omega L}[\pi + 2\beta - K\pi] \qquad (2.3.60)$$

During the time interval $0 \leq t_4 \leq (K\pi - \beta - \pi/3)/\omega$, the circuit equation for phase-a is

$$E - L\frac{di_{a4}}{dt_4} = i_{\ell 4} R_\ell \tag{2.3.61}$$

Due to the periodicity of load current, the expression for load current $i_{\ell 4}$ is the same as $i_{\ell 1}$ with a change in time variable from t_1 to t_4. Substituting for $i_{\ell 4}$ in (2.3.61), the solution for i_{a4} with the initial condition $i_{a4}(0^+) = I_{a3}$ is

$$i_{a4}(t_4) = \frac{Et_4}{3L} + \left(\frac{2E}{9R_\ell} - \frac{I(0)\ell}{3}\right)\left(1 - e^{\frac{-3R_\ell t_4}{L}}\right) + \frac{E(\pi + 2\beta - K\pi)}{3\omega L} \tag{2.3.62}$$

The phase-a current at $\omega t_4 = (K\pi - \beta - \pi/3)$ is given by

$$I_{a4} = \left(\frac{2E}{9R_\ell} - \frac{I(0)\ell}{3}\right)\left[1 - e^{\frac{-3R_\ell(K\pi - \beta - \pi/3)}{\omega L}}\right] + \frac{E(\beta + 2\pi/3)}{3\omega L} \tag{2.3.63}$$

During the time interval $0 \leq t_5 \leq (2\pi/3 - K\pi)/\omega$, the circuit equation for phase-a is

$$0 - L\frac{di_{a5}}{dt_5} = i_{\ell 5} R_\ell \tag{2.3.64}$$

The expression for load current $i_{\ell 5}$ is obtained by replacing t_2 with t_5 in equation (2.3.43). Substituting for $i_{\ell 5}$ in (2.3.64), the solution for i_{a5} with initial condition $i_{a5}(0^+) = I_{a4}$ is

$$i_{a5}(t_5) = -\frac{Et_5}{3L} + \left\{ \frac{E}{9R_\ell} + \left(\frac{I(0)\ell}{3} - \frac{2E}{9R_\ell} \right) e^{\frac{-3R_\ell(K\pi - \beta - \pi/3)}{\omega L}} \right\} \cdot e^{\frac{-3R_\ell t_5}{L}} + \frac{E(\beta + 2\pi/3)}{3\omega L} + \frac{E}{9R_\ell} - \frac{I(0)\ell}{3} \tag{2.3.65}$$

The phase current at $\omega t_5 = (2\pi/3 - K\pi)$ is

$$I_{a5} = \frac{E}{9R_\ell} e^{\frac{-3R_\ell(2\pi/3 - K\pi)}{\omega L}} + \left(\frac{I(0)\ell}{3} - \frac{2E}{9R_\ell} \right) e^{\frac{-3R_\ell(\pi/3 - \beta)}{\omega L}} + \frac{E(K\pi + \beta)}{3\omega L} + \frac{E}{9R_\ell} - \frac{I(0)\ell}{3} \tag{2.3.66}$$

During the time interval $0 \leq t_6 \leq (\beta/\omega)$, the circuit equation for phase-a is

$$0 - L\frac{di_{a6}}{dt_6} = i_{\ell 6} R_\ell \tag{2.3.67}$$

The expression for load current $i_{\ell 6}$ is obtained by replacing t_3 with t_6 in equation (2.3.49). Substituting for $i_{\ell 6}$ in (2.3.67), the solution for i_{a6} with initial condition $i_{a6}(0^+) = I_{a5}$ is

$$i_{a6}(t_6) = \left\{ \frac{E}{9R_\ell} + \frac{E}{9R_\ell} e^{\frac{-3R_\ell(2\pi/3 - K\pi)}{\omega L}} + \left(\frac{I(0)\ell}{3} - \frac{2E}{9R_\ell} \right) e^{\frac{-3R_\ell(\pi/3 - \beta)}{\omega L}} \right\} e^{\frac{-3R_\ell t_6}{L}} + \frac{E(\beta + K\pi)}{3\omega L} - \frac{I(0)\ell}{3} \qquad (2.3.68)$$

The phase-a current at $\omega t_6 = \beta$ is

$$I_{a6} = \frac{E}{3\omega L} [K\pi + \beta] \qquad (2.3.69)$$

During the time interval $0 \leq t_7 \leq (K\pi - \beta - \pi/3)/\omega$, the circuit equation for phase-a is

$$0 - L \frac{di_{a7}}{dt_7} = i_{\ell 7} R_\ell \qquad (2.3.70)$$

The expression for $i_{\ell 7}$ is obtained by replacing t_1 with t_7 in equation (2.3.37). Substituting for $i_{\ell 7}$ in (2.3.70), the solution for i_{a7} with the initial condition $i_{a7}(0^+) = I_{a6}$ is

$$i_{a7}(t_7) = \frac{-2Et_7}{3L} + \left(\frac{2E}{9R_\ell} - \frac{I(0)\ell}{3} \right) \left(1 - e^{\frac{-3R_\ell t_7}{L}} \right) + \frac{E(\beta + K\pi)}{3\omega L} \qquad (2.3.71)$$

The phase-a current at $\omega t_7 = (K\pi - \beta - \pi/3)$ is obtained as

$$I_{a7} = \left(\frac{2E}{9R_\ell} - \frac{I(0)\ell}{3} \right) \left(1 - e^{\frac{-3R_\ell(K\pi - \beta - \pi/3)}{\omega L}} \right)$$

$$+ \frac{E(3\beta + 2\pi/3 - K\pi)}{3\omega L} \qquad (2.3.72)$$

During the time interval $0 \leq t_8 \leq (2\pi/3 - K\pi)/\omega$, the circuit equation for phase-a is

$$0 - L \frac{di_{a8}}{dt_8} = i_{\ell 8} R_\ell \qquad (2.3.73)$$

The expression for load current $i_{\ell 8}$ is obtained by replacing t_2 with t_8 in equation (2.3.43). Substituting for $i_{\ell 8}$ in (2.3.73), the solution for i_{a8} with initial condition $i_{a8}(0^+) = I_{a7}$ is

$$i_{a8}(t_8) = \frac{-Et_8}{3L} + \left\{ \frac{E}{9R_\ell} + \left(\frac{I(0)\ell}{3} - \frac{2E}{9R_\ell} \right) e^{\frac{-3R_\ell(K\pi - \beta - \pi/3)}{\omega L}} \right\} e^{\frac{-3R_\ell t_8}{L}} + \frac{E(\beta - K\pi/3 + 2\pi/9)}{\omega L} + \frac{E}{9R_\ell} - \frac{I(0)\ell}{3}$$

(2.3.74)

The phase current I_{a8} at $\omega t_8 = (2\pi/3 - K\pi)$ is

$$I_{a8} = \frac{E\beta}{\omega L} + \frac{I(0)\ell}{3} \left(e^{\frac{-3R_\ell(\pi/3 - \beta)}{\omega L}} - 1 \right) + \frac{E}{9R_\ell} \left[1 + e^{\frac{-3R_\ell(2\pi/3 - K\pi)}{\omega L}} - 2e^{\frac{-3R_\ell(\pi/3 - \beta)}{\omega L}} \right]$$

(2.3.75)

During the time interval $0 \leq t_9 \leq (\beta/\omega)$, the circuit equation for phase-a

is

$$-E - L\frac{di_{a9}}{dt_9} = i_{\ell 9} R_\ell \tag{2.3.76}$$

The expression for $i_{\ell 9}$ is obtained from equation (2.3.49) by replacing t_3 with t_9. Substituting for $i_{\ell 9}$ in equation (2.3.76), the solution for i_{a9} with the initial condition $i_{a9}(0^+) = I_{a8}$ is

$$i_{a9}(t_9) = \frac{-Et_9}{L} + \left\{ \frac{E}{9R_\ell} + \frac{E}{9R_\ell} e^{\frac{-3R_\ell(2\pi/3 - K\pi)}{\omega L}} + \left(\frac{I(0)\ell}{3} - \frac{2E}{9R_\ell} \right) e^{\frac{-3R_\ell(\pi/3 - \beta)}{\omega L}} \right\} e^{\frac{-3R_\ell t_9}{L}} + \frac{E\beta}{\omega L} - \frac{I(0)\ell}{3} \tag{2.3.77}$$

The phase current I_{a9} at $\omega t_9 = \beta$ is equal to zero as shown in Figure 3(a) at $\Theta = \pi$.

2.3.2.3 Evaluation of Angle 'β'. The load current $I(0)\ell$ at $\omega t_1 = 0$ is given by equation (2.3.51). The load current $I(0)\ell$ can be represented by

$$I(0)\ell = -i_{b1}(0^+) + i_{c1}(0^+) \tag{2.3.78}$$

From the symmetry of phase voltages and phase currents, it can be observed from Figure 3(a) that

$$-i_{b1}(0^+) = I_{a3} \tag{2.3.79}$$

$$i_{c1}(0^+) = I_{a6} \tag{2.3.80}$$

Substituting the expressions already obtained for I_{a3} and I_{a6} in equation (2.3.78), a transcendental expression involving β, the circuit parameter ratio (X_L/R_ℓ) and pulse width ratio (K) is obtained and it is given below.

$$e^{\frac{-3R_\ell\beta}{\omega L}}\left(1 + e^{\frac{\pi R_\ell(3K - 2)}{\omega L}}\right) + \left(\frac{R_\ell\pi}{\omega L} + \frac{3R_\ell\beta}{\omega L} - 2\right)e^{\frac{-R_\ell\pi}{\omega L}}$$

$$-\left(\frac{R_\ell\pi}{\omega L}\right) - \left(\frac{3R_\ell\beta}{\omega L}\right) = 0 \qquad (2.3.81)$$

Equation (2.3.81) involving angle 'β' was solved by an iterative process using an IBM 370 digital computer. The value of K was varied within the range $(1/3) < K \leq (2/3)$. A set of values for angle 'β' was obtained by varying the ratio (X_L/R_ℓ) for each value of K chosen.

The equations in this section are valid for the ranges of K and β given by $(1/3) < K \leq (2/3)$ and $0 \leq \beta \leq (K\pi - \pi/3)$. In the evaluation of angle 'β', its maximum value in each iteration is limited to $(K\pi - \pi/3)$.

Similar analyses can be undertaken for the evaluation of the angle β for the different cases mentioned earlier. The maximum value of β is $(K\pi/2)$ corresponding to $(X_L/R_\ell) = \infty$, or the short circuit condition.

Theoretical results are presented in Figure 9 as a family of curves showing the values of β as a function of (X_L/R_ℓ) for different values of K.

The waveforms of phase-a bridge input voltage v_a, phase current i_a, and load current i_ℓ for K = 0.4 and $(X_L/R_\ell) = 3.0$ with the angle $\beta = 1.19°$ are shown in Figure 10.

2.4 Results and Discussion

Theoretical values of α are shown in Figure 7 as a function of the

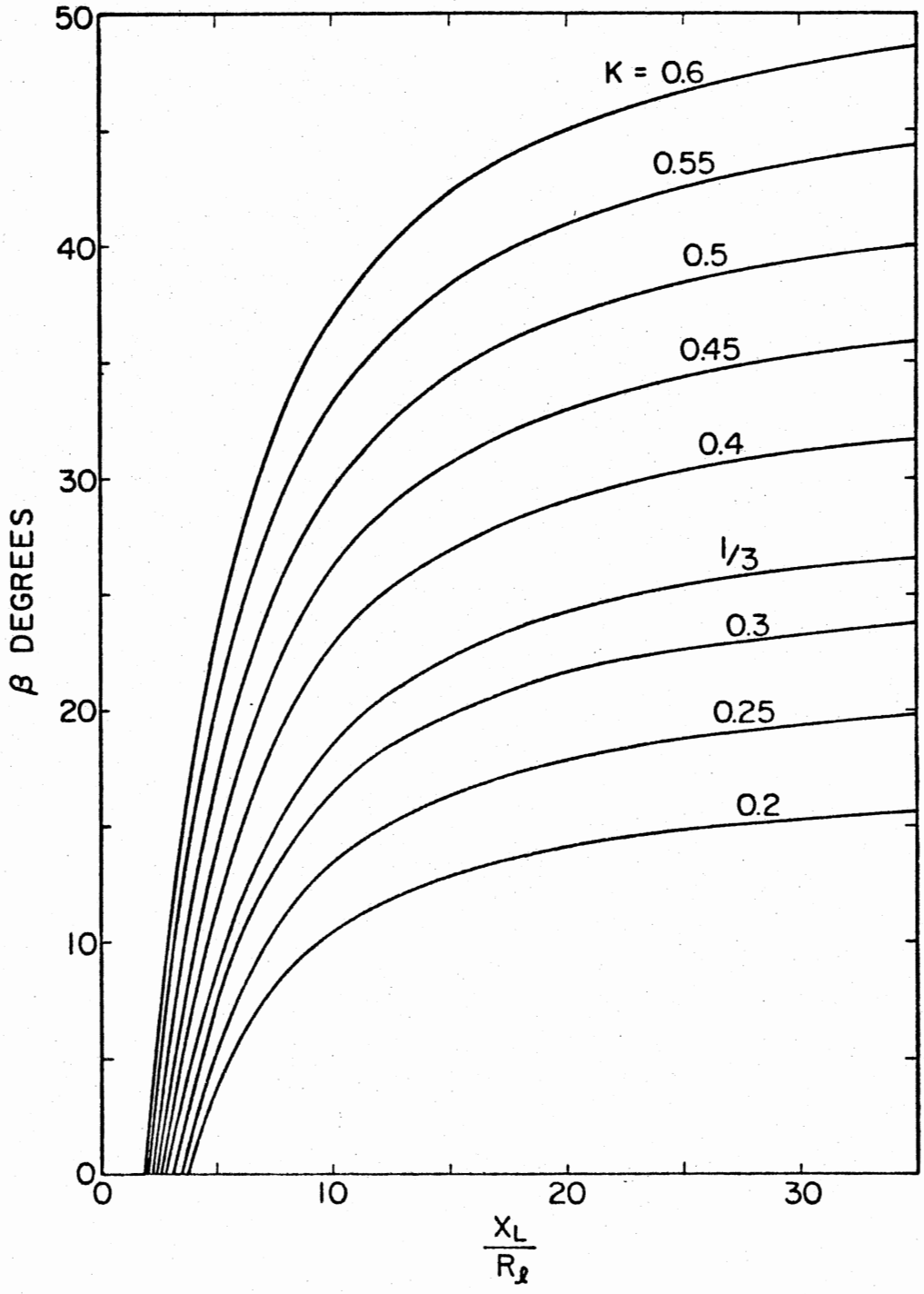

a.) Illustrating the overall dependence on (X_L/R_ℓ)

Figure 9. Theoretical Values of β

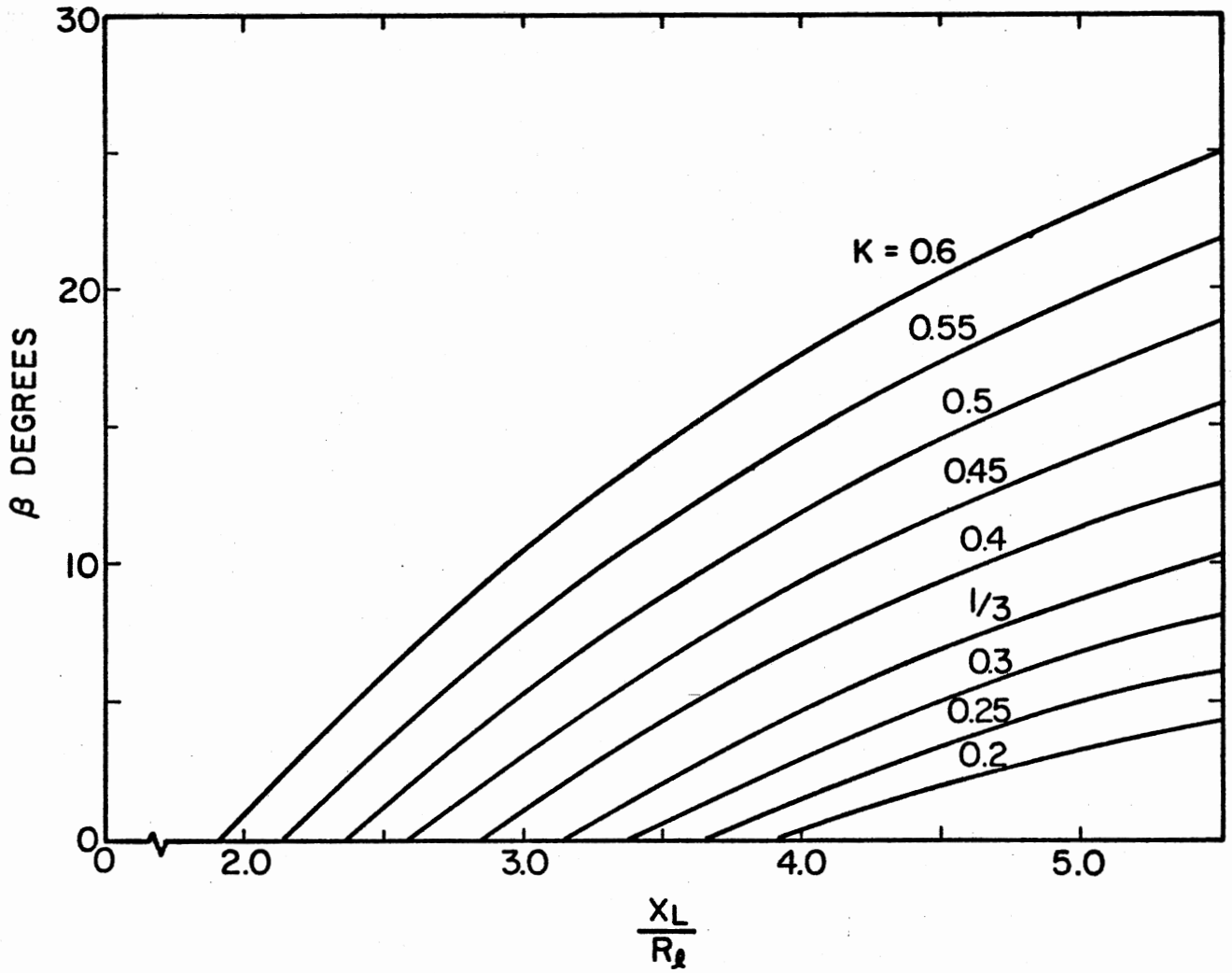

b.) Illustrating the dependence for small values of (X_L/R_ℓ)

Figure 9. (Continued)

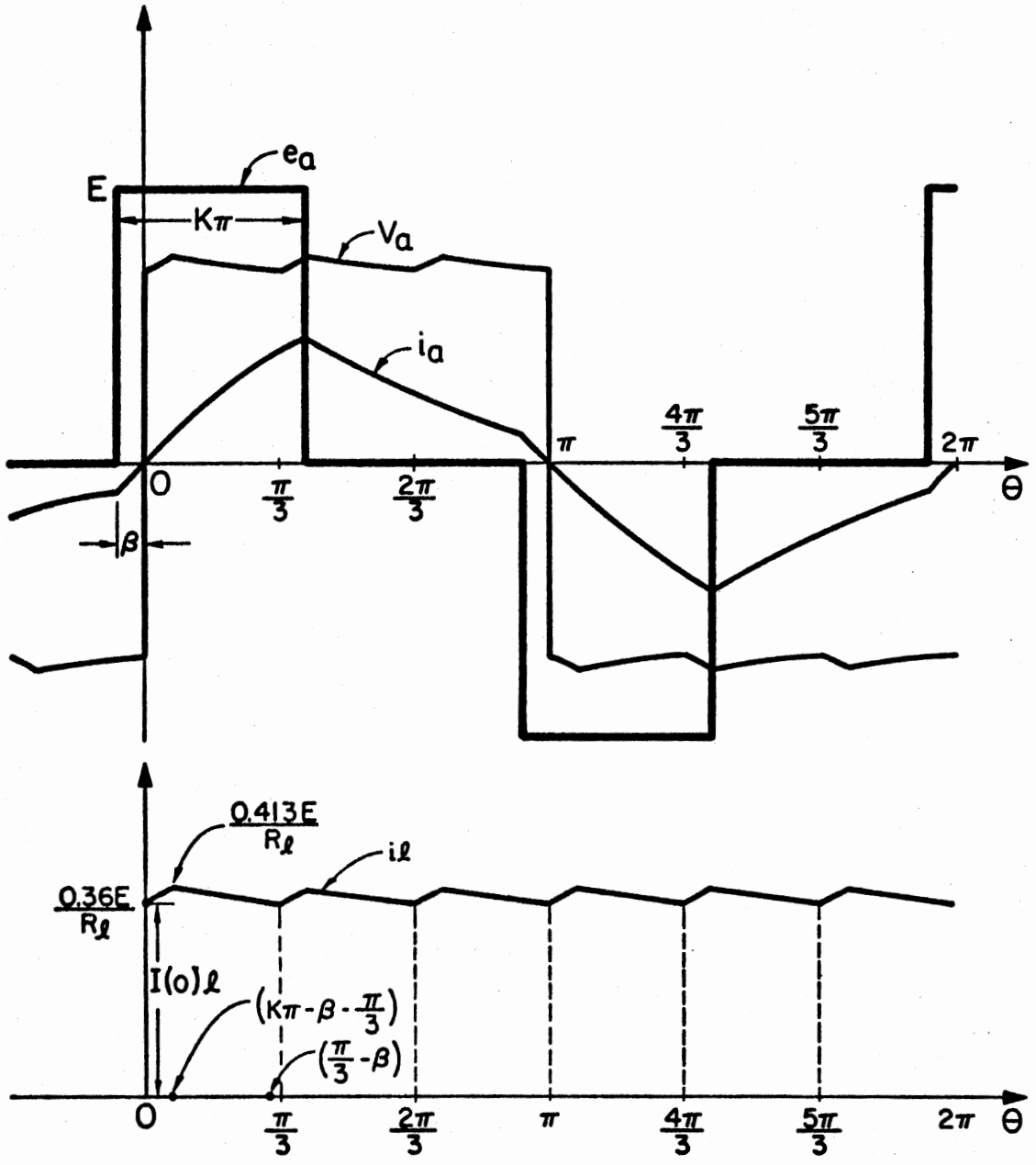

Figure 10. e_a, v_a, i_a and i_ℓ Waveforms for K=0.4, $(X_L/R_\ell) = 3.0$ and $\beta=1.19°$

circuit parameter ratio (X_L/R_ℓ) for different values of K. For values of K < (1/3) and with $\alpha \leq (\pi/3)$, only one bridge conducts through the load at any time, with the other two bridges remaining open. Such an operation will have the lowest utilization of components and therefore is uneconomical. As such, the case of $\alpha < (\pi/3)$ is not considered in detail.

It can be observed from the plots obtained that for a given pulse width ratio K, as (X_L/R_ℓ) increases, the conduction duration represented by angle 'α' increases. For known values of (X_L/R_ℓ) and K, the conduction angle α can be determined. Based on the value of the conduction angle 'α', the number of phases conducting and delivering power to the load can be determined. For example, when $\alpha = (2\pi/3)$, only two bridges conduct through the load simultaneously at all the time and with $\alpha = \pi$, all three bridges conduct through the load simultaneously. Bridge-input current and voltage have coincident zeros for all values of $\alpha \leq \pi$, even though there is a reactive element in the circuit. For values of K < (1/3), the wavy nature of the variation of α is a consequence of the increased number of time intervals needed in the analysis. However, the variation in α is smooth without jumps.

It can be observed from the plots that when the conduction angle α is equal to π, the bridge conducts for the entire half-period. This corresponds to the angle β being zero. Therefore, for a given pulse width ratio K, the parameter ratio (X_L/R_ℓ) corresponding to the cases of $\alpha = \pi$ and $\beta = 0$ should be the same. This has been verified for different values of K, by setting separately $\alpha = \pi$ and $\beta = 0$ in the respective non-linear algebraic equations involving α and β (see Figures 7 and 9b).

Figure 9 shows a family of curves depicting the variation of the angle β with (X_L/R_ℓ) and K. As (X_L/R_ℓ) increases, β increases for a given K. The plots become asymptotic to $(K\pi/2)$ as the parameter ratio (X_L/R_ℓ) approaches infinity corresponding to the short circuit condition. Then, the phase angle β reaches a maximum value given by $(K\pi/2)$. For all values of angle β, all the three phases conduct through the load simultaneously.

The phase-a bridge input voltage v_a, the phase current i_a, and the load current i_ℓ waveforms are shown in Figures 8 and 10 for cases (i) and (iv) respectively.

For case (i), with K = 0.4 and $(X_L/R_\ell) = 0.5$, the conduction angle α is determined as 107.18°. With ideal diodes, the bridge input voltage v_a waveform is the same as the load voltage v_ℓ waveform as long as the bridge conducts. When diode pair 1 stops conducting at $\Theta = \alpha$, the bridge input voltage v_a and phase current i_a simultaneously go to zero. However, the load current and voltage are periodic with a period of $(\pi/3)$.

For case (iv), with K = 0.4 and $(X_L/R_\ell) = 3.0$, the angle β is determined as 1.19°. Each diode pair conducts through the load for the entire half-period and the bridge input voltage v_a waveform and the load voltage v_ℓ waveform are similar over the half-period as shown in Figure 10. The bridge input voltage v_a and phase current i_a simultaneously go to zero when the diode pair 1 stops conducting. The load current is periodic with a period of $(\pi/3)$.

For a given pulse width ratio K, as the parameter ratio (X_L/R_ℓ) is increased, angles α and β increase, but the amplitudes of load current i_ℓ, phase current i_a and the value of initial load current $I(0)_\ell$ at $\Theta = 0$ decrease. It is observed that as the parameter ratio (X_L/R_ℓ)

increases, the load current waveform becomes more and more flat. With $K = 0.4$ and $(X_L/R_\ell) = 3.0$, the variation in the load current is within 6% of its peak value.

CHAPTER III

EFFECT OF TRAPEZOIDAL WAVEFORM ON THE OPERATION OF THE PARALLEL-BRIDGE RECTIFIER SYSTEM WITH BRIDGE-INPUT CAPACITORS

3.1 Introduction

It is well known that the use of proper capacitors across stator windings will decrease the excitation requirements [36] and improve the efficiency of an alternator. An alternator feeding into a parallel-bridge rectifier system with stator tuning capacitors exhibits similar advantages as well [37]. Tsung [38] analyzed the parallel-bridge rectifier system with capacitors at bridge input terminals and resistive loads for the case of sinusoidal source voltage waveforms. Results of this analysis have been applied successfully to develop an idealized model for the field modulated generator system [39].

With non-sinusoidal field forms, an exact analysis of the parallel-bridge rectifier system with bridge input capacitors which includes the dependence of the field form on load becomes extremely complicated. In this chapter, some judicious approximations are made to analyze the basic behavior of the PBRS with bridge input capacitors when the source voltage waveforms are non-sinusoidal of the type employed in the successful experimental prototypes. In the FMGS experimental prototype, under the combined effect of armature reaction, rotor excitation and the magnetic circuit configuration, the voltages induced in the stator windings have a waveform

which can be closely approximated by a symmetric trapezoid with the top width equal to one third of the half-period, under full load conditions.

The central role played by the PBRS with bridge input capacitors in the overal performance of the FMGS suggests that this circuit be studied first in detail with trapezoidal source voltage waveforms. This chapter presents the results of such a study. The approach taken is very similar to the one used in Chapter II. Differential equations relating the various voltages and currents in the idealized model are set up and solved with proper boundary conditions. Two angles, γ and β, are introduced relating the "on" and "off" conditions of various diodes. These angles are evaluated by solving appropriate non-linear algebraic equations using an IBM 370 digital computer.

Section 3.2 begins with a description of the circuit model, the assumptions involved and the general nature of the waveforms. The need to consider different ranges of values for $(\gamma + \beta)$ is discussed.

In Section 3.3 the circuit differential equations are formulated and solved using proper boundary conditions. The non-sinusoidal nature of the input waveforms requires splitting the half-period into a number of segments for the purpose of analysis. Theoretical values of the two key angles γ and β are evaluated and plotted with non-dimensional circuit constants (X_L/R_ℓ) and (X_L/X_C) as parameters. Appropriate voltage and current waveforms are presented for the cases considered.

Section 3.4 summarizes the results and discusses the relationship between angles γ, β and the non-dimensional circuit parameter ratios (X_L/R_ℓ) and (X_L/X_C). The relationship between various voltages and currents are also discussed.

3.2 Idealized Model and Assumptions

The parallel-bridge rectifier system considered in the present study consists of three full-wave bridges with a capacitor across each pair of bridge input terminals, each combination of full-wave bridge and capacitor being connected to one of the three isolated phases of a three phase power source, with their outputs tied in parallel across the load. Figure 11 shows an idealized PBRS model. The following assumptions are made in the development and analysis of the model.

1. All diodes are assumed to be ideal switches with zero forward voltage drops and zero reverse currents.

2. The source impedance is assumed to be purely reactive. This is a reasonable approximation commonly used in the study of practical systems. For a three-phase alternator used as the source, the inductance L will represent the effective commutating inductance of the machine per phase.

3. Each phase of the source is modeled as an ideal voltage source in series with a commutating inductance.

4. The source voltage waveform is a symmetric trapezoid with the top width equal to one third of the half-period.

5. With flat-topped source voltages, the bridge input voltage is not expected to vary much during the conduction duration of a bridge and consequently the capacitor current during this period will be small compared to the load component of the bridge-input current. Therefore, the current through the capacitor during the conduction duration of the corresponding bridge is neglected in the analysis.

6. As a direct consequence of the assumption that no current flows through the bridge-input capacitor whenever the corresponding bridge

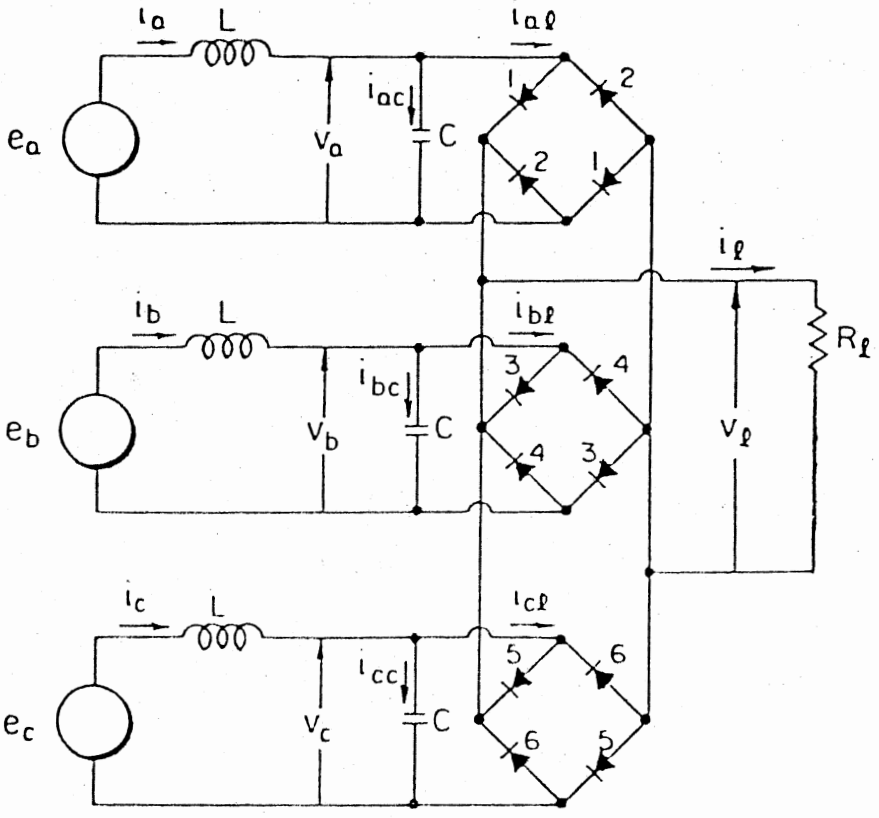

Figure 11. Idealized PBRS Model with Bridge-Input Capacitors

is delivering power to the load, the initial current through the commutating inductance L of phase 'a' at $t = 0^-$ when diode pair 2-2 stops conduction is zero. Similar statements can be made for the other two phases.

Figure 12(a) shows the three trapezoidal source voltage waveforms and their relationship to various currents and bridge-input voltages. The general nature of the load current waveform is shown in Figure 12(b). The load current is periodic with a period of $(\pi/3)$. Within this period, it consists of two specific parts. The first part corresponds to the duration when only two bridges are conducting with the third decoupled from the load, and the second part is the result of simultaneous conduction of all three bridges. Whenever a bridge-input voltage falls below the load voltage, the corresponding bridge gets decoupled from the load and conduction will then be through the series circuit consisting of the commutating inductance and the bridge input capacitor. When a bridge-input voltage becomes equal to the load voltage, the corresponding bridge starts conducting through the load. At this instant, there is an instantaneous transfer of current from the capacitor to the load in order to maintain the continuity of current through the commutating inductance. The duration of current flow through the capacitor is determined by the energy stored in the commutating inductance, the bridge-input capacitance, load voltage and the source voltage. For values of (X_L/R_ℓ) and (X_L/X_C) in the vicinity of 1.3 and 0.04 respectively, the angles γ and β will be small with their sum less than $(\pi/3)$. For values of (X_L/R_ℓ) and (X_L/X_C) in the vicinity of 2.0 and 0.18 respectively, the sum of angles γ and β will be greater than $(\pi/3)$. This latter case is shown in Figure 13(a). The general nature of the associated load current waveform is

shown in Figure 13(b). The load current is once again periodic with a period of $(\pi/3)$.

The significance of angles γ and β is evident from Figure 12(a). The transfer of conduction from one diode pair to the other of any one bridge is associated with a decoupling of that bridge from the other two for a duration given by (γ/ω). The angle β determines the time difference (equal to β/ω) between the zeros of the source voltage and the corresponding phase-current for given circuit parameter ratios (X_L/R_ℓ) and (X_L/X_C). The non-sinusoidal nature of the input waveform requires splitting the half-period into a number of segments as shown in Figure 12(a) for the purpose of analysis. Time intervals t_1, t_4 and t_7 in Figure 12(a) correspond to decoupling durations of phases a, c and b; time intervals t_2, t_3, t_5, t_6, t_8 and t_9 correspond to simultaneous conduction of all three bridges.

Two ranges of values for the sum $(\gamma + \beta)$ are identified for the purpose of analysis. They are:

Case (A) $\quad 0 < (\gamma + \beta) \leq (\pi/3)$; see Figure 12(a)

Case (B) $\quad (\pi/3) \leq (\gamma + \beta) \leq (2\pi/3)$; see Figure 13(a)

In Case (B), the start of the decoupling duration of a particular phase is assumed to be within the ramp portion of the corresponding source voltage waveform. This is reasonable for the normal operating range of circuit parameter ratios.

In the following sections, analysis of Case (A) is presented in detail. For the sake of brevity, only the specific differences between the analyses of Case (A) and Case (B) are summarized next. However, plots of theoretical vaules of angles γ and β, current and voltage waveforms are presented for both cases.

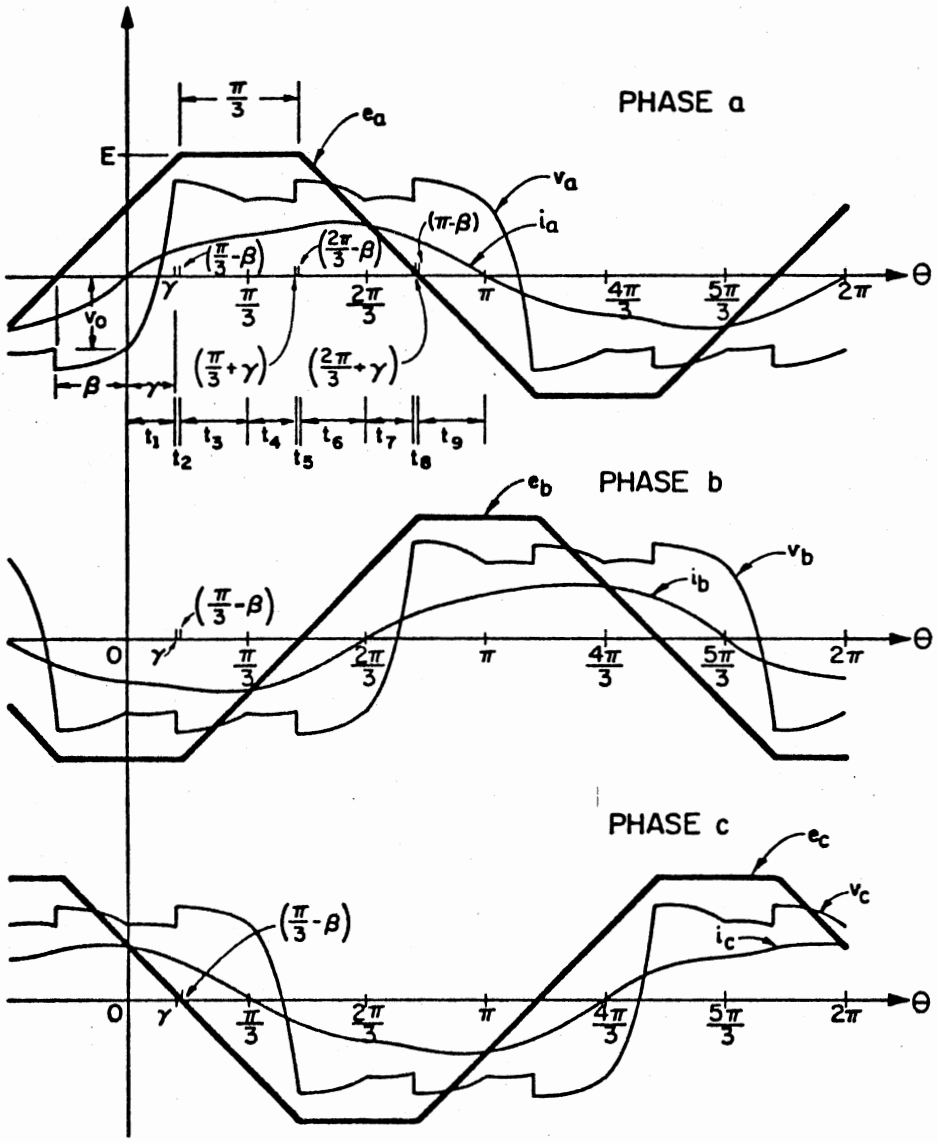

a.) e, v, and i waveforms in the three phases

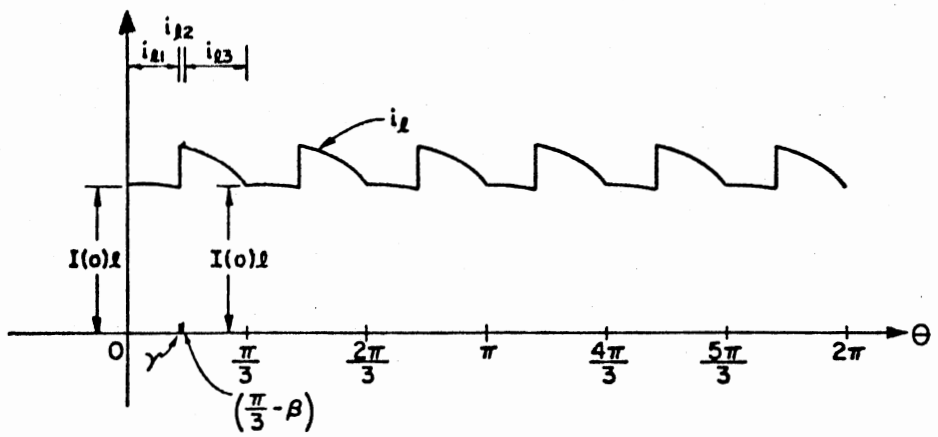

b.) Load current waveform

Figure 12. Voltage and Current Waveforms for $(\gamma+\beta) < \pi/3$

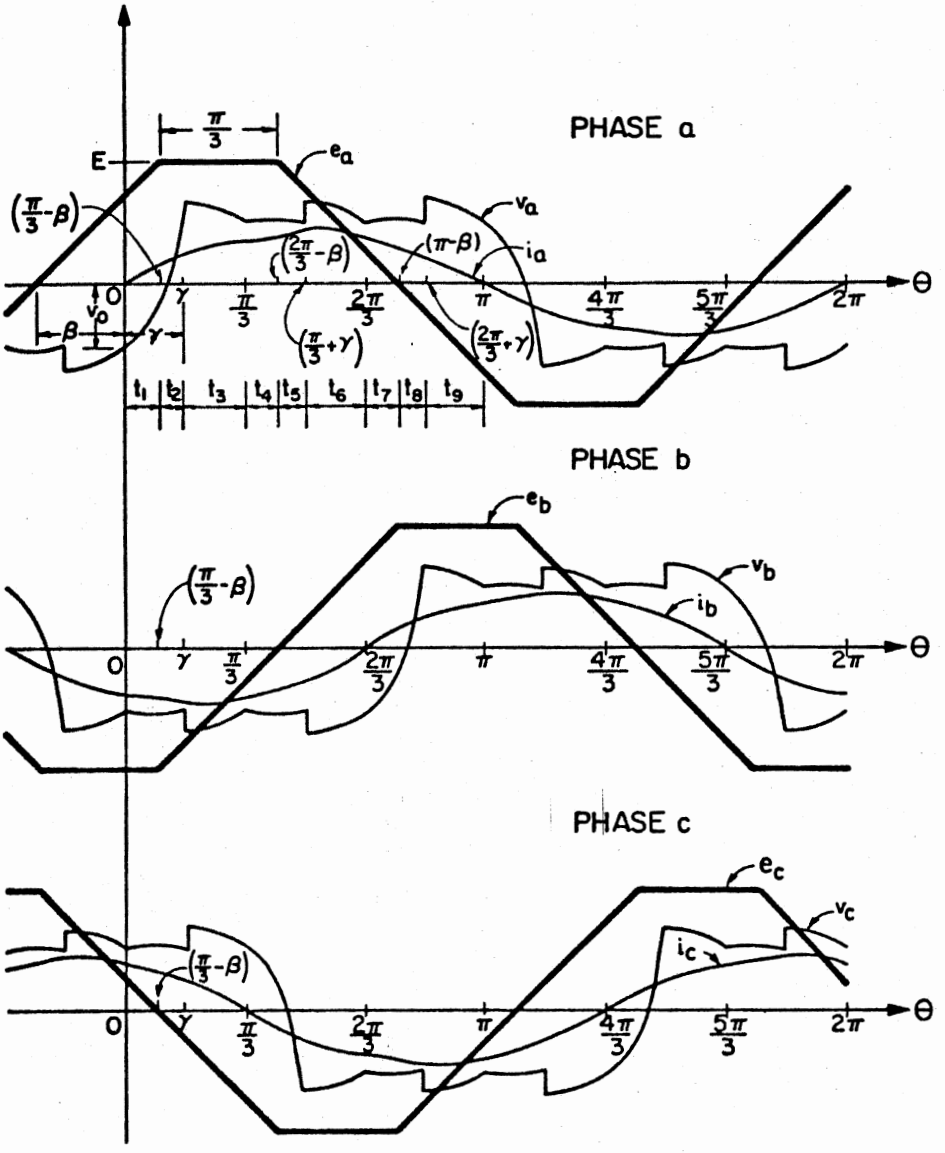

a.) e, v, and i waveforms in the three phases

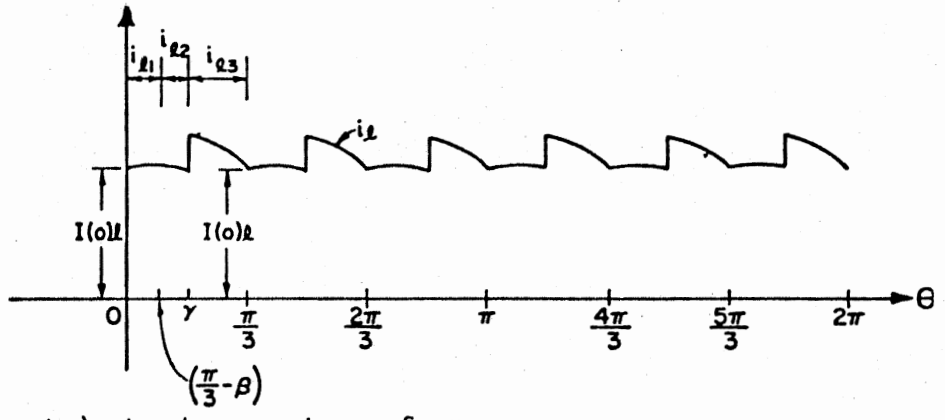

b.) Load current waveform

Figure 13. Voltage and Current Waveforms for $(\gamma+\beta) > \pi/3$

3.3 Analysis

3.3.1 Case (A) $0 < (\gamma + \beta) \leq (\pi/3)$

Figure 14 illustrates the voltage and current waveforms for the case under consideration. In the analysis, one need to consider only one half of a cycle (θ = 0 to π) corresponding to the source frequency. This is subdivided into nine segments and the quantities associated with these intervals are designated with subscripts 1 through 9 respectively. For convenience, the circuit of phase-a is considered. Waveforms for phases b and c will be similar, except for the inherent phase differences of $\pm(2\pi/3)$.

Expressions for various voltages and currents will be derived during each of the time intervals t_1 through t_9 with the restriction that there can be no jump in the current through the commutating inductance L. Since the load current is periodic with a period of $(\pi/3)$, the different expressions obtained for load current during this period can be used for the evaluation of the load current during other corresponding durations with a change in the time variable. Time zero is chosen such that at $t = 0^-$, diode pair 2 (in Figure 11) stops conducting.

3.3.1.1 Derivation of $i_{a1}(t_1)$ for $0^+ \leq t_1 \leq (\gamma/\omega^-)$. At the instant $t = 0$, phase-a circuit becomes decoupled from the other two ($i_{a\ell 1} = 0$) with zero initial current in L and with an initial voltage of $-V_o$ across C as shown in Figure 15. During this time interval the circuit equation is

$$\frac{E\beta}{\theta_1} + \frac{E\omega t_1}{\theta_1} - L\frac{di_{a1}}{dt_1} - \frac{1}{C}\int i_{a1}\, dt_1 = 0 \qquad (3.3.1)$$

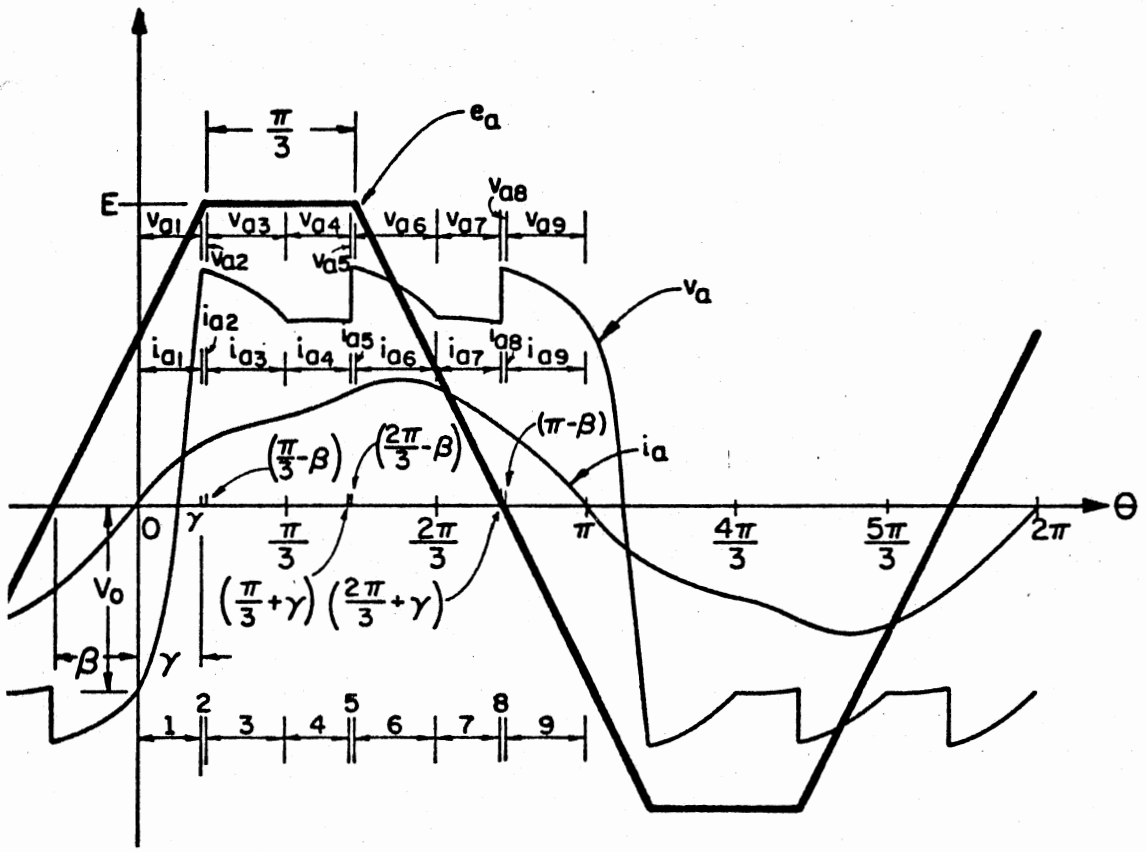

Figure 14. Illustrating the General Nature of Case (A) Waveforms for Phase-a, ($X_L/X_C \simeq 0.08$)

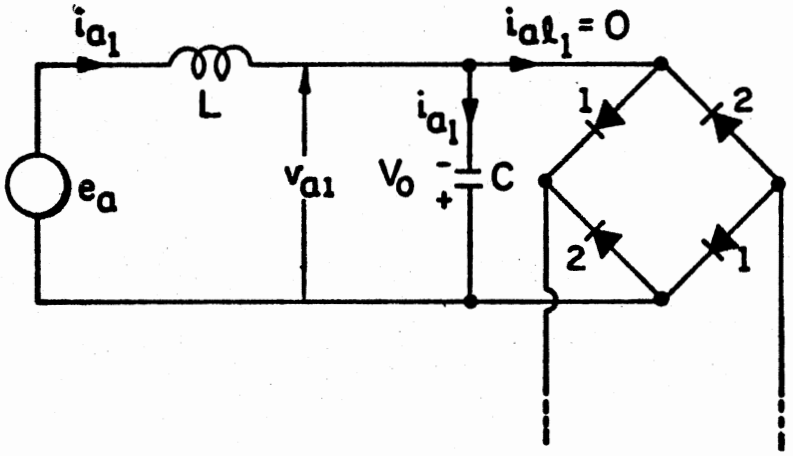

Figure 15. Illustrating the Status of Phase-a Circuit at $t = 0^+$

Solving (3.3.1) with proper initial conditions yields

$$i_{a1}(t_1) = \left(\frac{V_o}{1} + \frac{E\beta}{\Theta_1}\right)\sqrt{\frac{C}{L}}\ \sin\left(\frac{t_1}{\sqrt{LC}}\right) + \frac{E\omega C}{\Theta_1}\left(1 - \cos\frac{t_1}{\sqrt{LC}}\right) \qquad (3.3.2)$$

The phase-a current at $t_1 = (\gamma/\omega^-)$ is

$$I_{a1} = \left(\frac{V_o}{1} + \frac{E\beta}{\Theta_1}\right)\sqrt{\frac{C}{L}}\ \sin\frac{\gamma}{\omega\sqrt{LC}} + \frac{E\omega C}{\Theta_1}\left(1 - \cos\frac{\gamma}{\omega\sqrt{LC}}\right) \qquad (3.3.3)$$

The bridge-input voltage during this period is given by

$$v_{a1}(t_1) = \frac{E\beta}{\Theta_1} + \frac{E\omega t_1}{\Theta_1} - L\frac{di_{a1}}{dt_1} \qquad (3.3.4)$$

and the bridge input voltage at $t_1 = (\gamma/\omega^-)$ is

$$V_{a1} = \frac{E}{\Theta_1}(\gamma + \beta) - \left(\frac{V_o}{1} + \frac{E\beta}{\Theta_1}\right)\cos\frac{\gamma}{\omega\sqrt{LC}} - \frac{E\omega\sqrt{LC}}{\Theta_1}\sin\frac{\gamma}{\omega\sqrt{LC}} \qquad (3.3.5)$$

3.3.1.2 Derivation of the Load Current. During the time interval $0^+ \leq t_1 \leq (\gamma/\omega^-)$, only the bridges connected to phase-b and phase-c conduct through the load with phase-a decoupled from the load as shown in Figuare 16. Assuming ideal diodes, circuit equations for phases b and c are given as follows:

$$E + L\frac{di_{b1}}{dt_1} = i_{\ell 1}\,R_\ell \qquad (3.3.6)$$

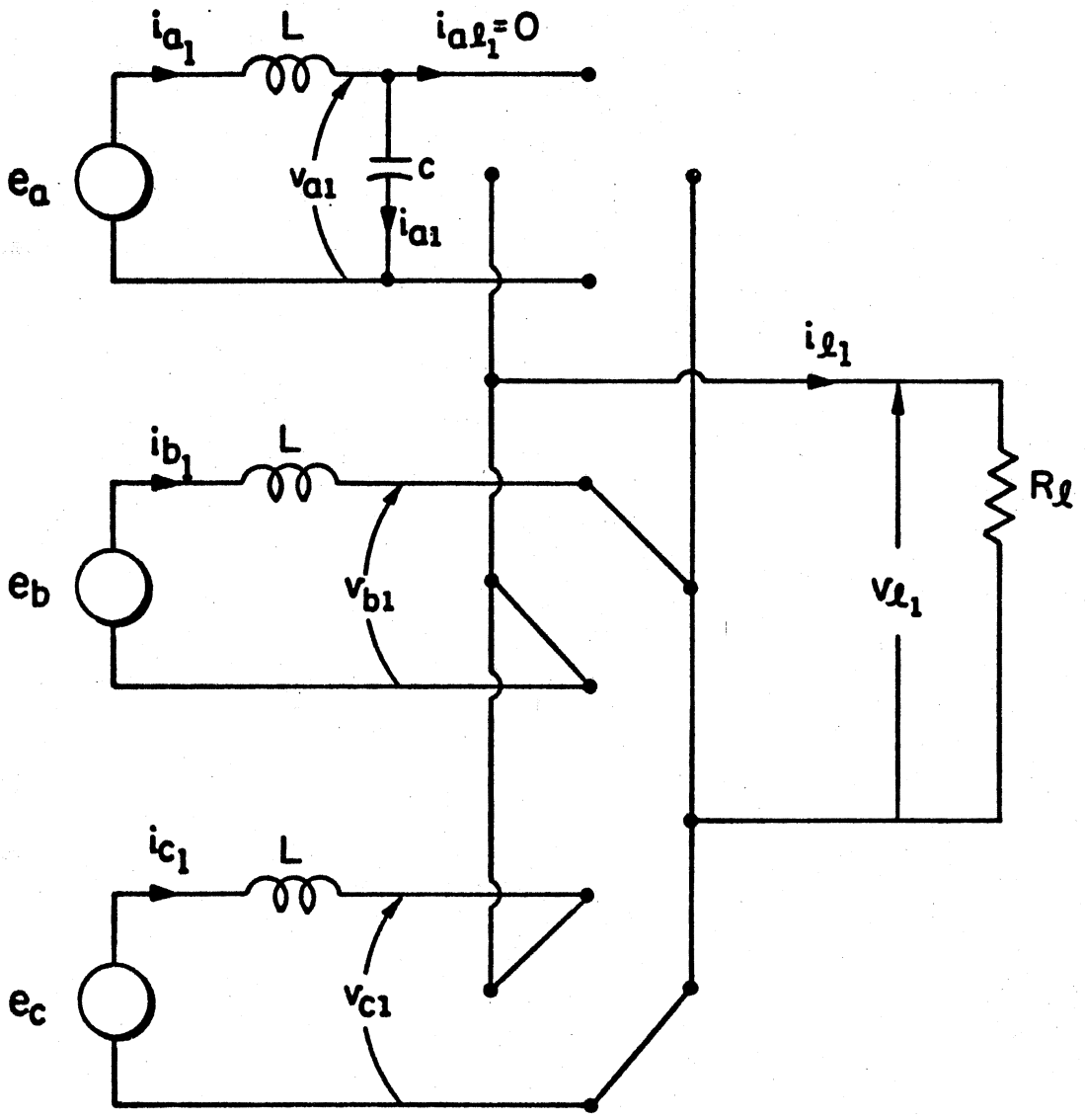

Figure 16. Illustrating the Assumed Status of the System During $0^+ \leq \theta \leq \gamma^-$

$$E - \frac{E\beta}{\Theta_1} - \frac{E\omega t_1}{\Theta_1} - L\frac{di_{c1}}{dt_1} = i_{\ell 1} R_\ell \qquad (3.3.7)$$

The load current $i_{\ell 1}(t_1)$ is given by

$$i_{\ell 1} = i_{c1} - i_{b1} \qquad (3.3.8)$$

Adding (3.3.6) and (3.3.7) and using (3.3.8), the following differential equation is obtained for $i_{\ell 1}$.

$$\frac{di_{\ell 1}}{dt_1} + \frac{2R_\ell}{L} i_{\ell 1} = \frac{2E}{L} - \frac{E\beta}{L\Theta_1} - \frac{E\omega t_1}{L\Theta_1} \qquad (3.3.9)$$

Solution of (3.3.9) is

$$i_{\ell 1}(t_1) = I(0)_\ell \, e^{\frac{-2R_\ell t_1}{L}} + \left(\frac{E}{R_\ell} - \frac{E\beta}{2\Theta_1 R_\ell} + \frac{E\omega L}{4\Theta_1 R_\ell^2}\right)\left(1 - e^{\frac{-2R_\ell t_1}{L}}\right) - \frac{E\omega t_1}{2\Theta_1 R_\ell} \qquad (3.3.10)$$

where $I(0)_\ell$ is the load current at $\omega t_1 = 0$. The load current at $\omega t_1 = (\gamma^-)$ is given by

$$I_{\ell 1}^- = I(0)_\ell \, e^{\frac{-2R_\ell \gamma}{\omega L}} + \left(\frac{E}{R_\ell} - \frac{E\beta}{2\Theta_1 R_\ell} + \frac{E\omega L}{4\Theta_1 R_\ell^2}\right)\left(1 - e^{\frac{-2R_\ell \gamma}{\omega L}}\right)$$

$$- \frac{E\gamma}{2\Theta_1 R_\ell} \tag{3.3.11}$$

At $t_1 = (\gamma/\omega^+)$, phase-a starts conducting through the load. Therefore, the total load current $I_{\ell 1}$ at $t_1 = (\gamma/\omega^+)$, which includes the current transferred from the capacitor branch, is given by

$$I_{\ell 1} = I_{\ell 1}^- + I_{a1} \tag{3.3.12}$$

Substituting for $I_{\ell 1}^-$ and I_{a1} from (3.3.11) and (3.3.3) respectively in (3.3.12), the expression for $I_{\ell 1}$ is obtained as follows:

$$\begin{aligned} I_{\ell 1} = {} & I(0)_\ell \, e^{\frac{-2R_\ell \gamma}{\omega L}} \\ & + \left(\frac{E}{R_\ell} - \frac{E\beta}{2\Theta_1 R_\ell} + \frac{E\omega L}{4\Theta_1 R_\ell^2}\right)\left(1 - e^{\frac{-2R_\ell \gamma}{\omega L}}\right) \\ & - \frac{E\gamma}{2\Theta_1 R_\ell} + \left(\frac{V_o}{1} + \frac{E\beta}{\Theta_1}\right)\sqrt{\frac{C}{L}} \sin \frac{\gamma}{\omega\sqrt{LC}} \\ & + \frac{E\omega C}{\Theta_1}\left(1 - \cos \frac{\gamma}{\omega\sqrt{LC}}\right) \end{aligned} \tag{3.3.13}$$

During the interval $\gamma \leq \Theta \leq (\pi/3 - \beta)$, define a new time variable t_2 such that

$$\omega t_2 = (\Theta - \gamma)$$

and the time interval of interest then becomes $0 \leq t_2 \leq (\pi/3 - \beta - \gamma)/\omega$. All three phases conduct through the load during this duration and the new circuit equations are given below.

$$\frac{E}{\Theta_1}(\beta + \gamma) + \frac{E}{\Theta_1}\omega t_2$$

$$- L \frac{di_{a2}}{dt_2} = i_{\ell 2} R_\ell \qquad (3.3.14)$$

$$E + L \frac{di_{b2}}{dt_2} = i_{\ell 2} R_\ell \qquad (3.3.15)$$

$$E - \frac{E}{\Theta_1}(\beta + \gamma)$$

$$- \frac{E\omega t_2}{\Theta_1} - L \frac{di_{c2}}{dt_2} = i_{\ell 2} R_\ell \qquad (3.3.16)$$

Substituting the relationship between phase currents and load current, the following differential equation is obtained for $i_{\ell 2}$.

$$\frac{di_{\ell 2}}{dt_2} + \frac{3R_\ell}{L} i_{\ell 2} = \frac{2E}{L} \qquad (3.3.17)$$

Solution of (3.3.17) with the initial condition $i_{\ell 2}(0^+) = I_{\ell 1}$ is

$$i_{\ell 2}(t_2) = I_{\ell 1} e^{\frac{-3R_\ell t_2}{L}} + \frac{2E}{3R_\ell}\left(1 - e^{\frac{-3R_\ell t_2}{L}}\right) \qquad (3.3.18)$$

The load current at $\omega t_2 = (\pi/3 - \beta - \gamma)$ is given by

$$I_{\ell 2} = I_{\ell 1}\left(e^{\frac{-3R_\ell}{\omega L}(\pi/3 - \beta - \gamma)}\right)$$

$$+ \frac{2E}{3R_\ell}\left(1 - e^{\frac{-3R_\ell}{\omega L}(\pi/3 - \beta - \gamma)}\right) \qquad (3.3.19)$$

During the interval $(\pi/3 - \beta) \leq \theta \leq (\pi/3)$, define a new time variable t_3 such that

$$\omega t_3 = [\theta - (\pi/3 - \beta)]$$

and the time interval becomes $0 \leq t_3 \leq (\beta/\omega)$. Phases a, b and c conduct through the load and the circuit equations are

$$E - L \frac{di_{a3}}{dt_3} = i_{\ell 3} R_\ell \tag{3.3.20}$$

$$E - \frac{E}{\theta_1} \omega t_3 + L \frac{di_{b3}}{dt_3} = i_{\ell 3} R_\ell \tag{3.3.21}$$

$$- \frac{E\omega t_3}{\theta_1} - L \frac{di_{c3}}{dt_3} = i_{\ell 3} R_\ell \tag{3.3.22}$$

Substituting the relationship between phase currents and load current, the following differential equation is obtained for $i_{\ell 3}$.

$$\frac{di_{\ell 3}}{dt_3} + \frac{3R_\ell}{L} i_{\ell 3} = \frac{2E}{L} - \frac{2E\omega t_3}{\theta_1 L} \tag{3.3.23}$$

Solution of (3.3.23) with the initial condition $i_{\ell 3}(0^+) = I_{\ell 2}$ is given below.

$$i_{\ell 3}(t_3) = I_{\ell 2} e^{\frac{-3R_\ell t_3}{L}} + \left(\frac{2E}{3R_\ell} + \frac{2E\omega L}{9R_\ell^2 \theta_1}\right)\left(1 - e^{\frac{-3R_\ell t_3}{L}}\right) - \frac{2E\omega t_3}{3R_\ell \theta_1} \tag{3.3.24}$$

The load current at $\omega t_3 = \beta$ is given by

$$I_{\ell 3} = I_{\ell 2}\, e^{\frac{-3R_\ell \beta}{\omega L}} + \left(\frac{2E}{3R_\ell} + \frac{2E\omega L}{9R_\ell^{\,2}\Theta_1}\right)\left(1 - e^{\frac{-3R_\ell \beta}{\omega L}}\right)$$

$$- \frac{2E\beta}{3R_\ell \Theta_1} \qquad (3.3.25)$$

Due to the symmetry of the source voltage and phase current waveforms, the load current i_ℓ is periodic with a period $(\pi/3)$. Therefore the load current at $\Theta = (\pi/3)$ should be equal to the load current at $\Theta = 0$. Equating (3.3.25) to $I(0)_\ell$ and substituting for $I_{\ell 2}$ and $I_{\ell 1}$ the expressions already obtained, the following equation is obtained.

$$I(0)_\ell\left[1 - e^{\frac{R_\ell}{\omega L}(\gamma - \pi)}\right] = \left(\frac{E}{R_\ell} - \frac{E\beta}{2\Theta_1 R_\ell} + \frac{E\omega L}{4\Theta_1 R_\ell^{\,2}}\right)$$

$$\cdot\left(e^{\frac{-3R_\ell}{\omega L}(\pi/3 - \gamma)} - e^{\frac{R_\ell}{\omega L}(\gamma - \pi)}\right)$$

$$- \frac{E\gamma}{2\Theta_1 R_\ell}\, e^{\frac{-3R_\ell}{\omega L}(\pi/3 - \gamma)}$$

$$+ \left(\frac{V_o}{1} + \frac{E\beta}{\Theta_1}\right)\sqrt{\frac{C}{L}}\, \sin\frac{\gamma}{\omega\sqrt{LC}}\, e^{\frac{-3R_\ell}{\omega L}(\pi/3 - \gamma)}$$

$$+ \frac{E\omega C}{\Theta_1}\left(1 - \cos\frac{\gamma}{\omega\sqrt{LC}}\right) e^{\frac{-3R_\ell}{\omega L}(\pi/3 - \gamma)}$$

$$+ \frac{2E}{3R_\ell}\left(e^{\frac{-3R_\ell \beta}{\omega L}} - e^{\frac{-3R_\ell}{\omega L}(\pi/3 - \gamma)}\right)$$

$$+\left(\frac{2E}{3R_\ell}+\frac{2E\omega L}{9R_\ell^{\,2}\Theta_1}\right)\left(1-e^{\frac{-3R_\ell\beta}{\omega L}}\right)-\frac{2E\beta}{3R_\ell\Theta_1} \tag{3.3.26}$$

in which

$$V_o = I(0)_\ell R_\ell$$

and

$$\Theta_1 = \pi/3$$

3.3.1.3 Derivation of Phase-a Current for $t > (\gamma/\omega^+)$. At the instant $t_1 = (\gamma/\omega^+)$, phase-a bridge starts conducting through the load, and simultaneously all the current through the capacitor circuit is diverted to the load circuit. With ideal diodes, the bridge input voltage should be equal to the load voltage when a pair of diodes conduct. During the time interval $0^+ \leq t_2 \leq (\pi/3 - \beta - \gamma)/\omega$, the PBRS circuit is shown in Figure 17 and the circuit equation for phase-a is

$$\frac{E}{\Theta_1}(\gamma+\beta)+\frac{E\omega t_2}{\Theta_1} - L\frac{di_{a2}}{dt_2} = i_{\ell 2}R_\ell \tag{3.3.27}$$

Substituting for $i_{\ell 2}$ from (3.3.18) in (3.3.27) and solving for i_{a2} with the initial condition $i_{a2}(0^+) = I_{a1}$ yields

$$i_{a2}(t_2) = \frac{E(\gamma+\beta)t_2}{\Theta_1 L}+\frac{E\omega t_2^{\,2}}{2\Theta_1 L}+\frac{I_{\ell 1}}{3}e^{\frac{-3R_\ell t_2}{L}}$$

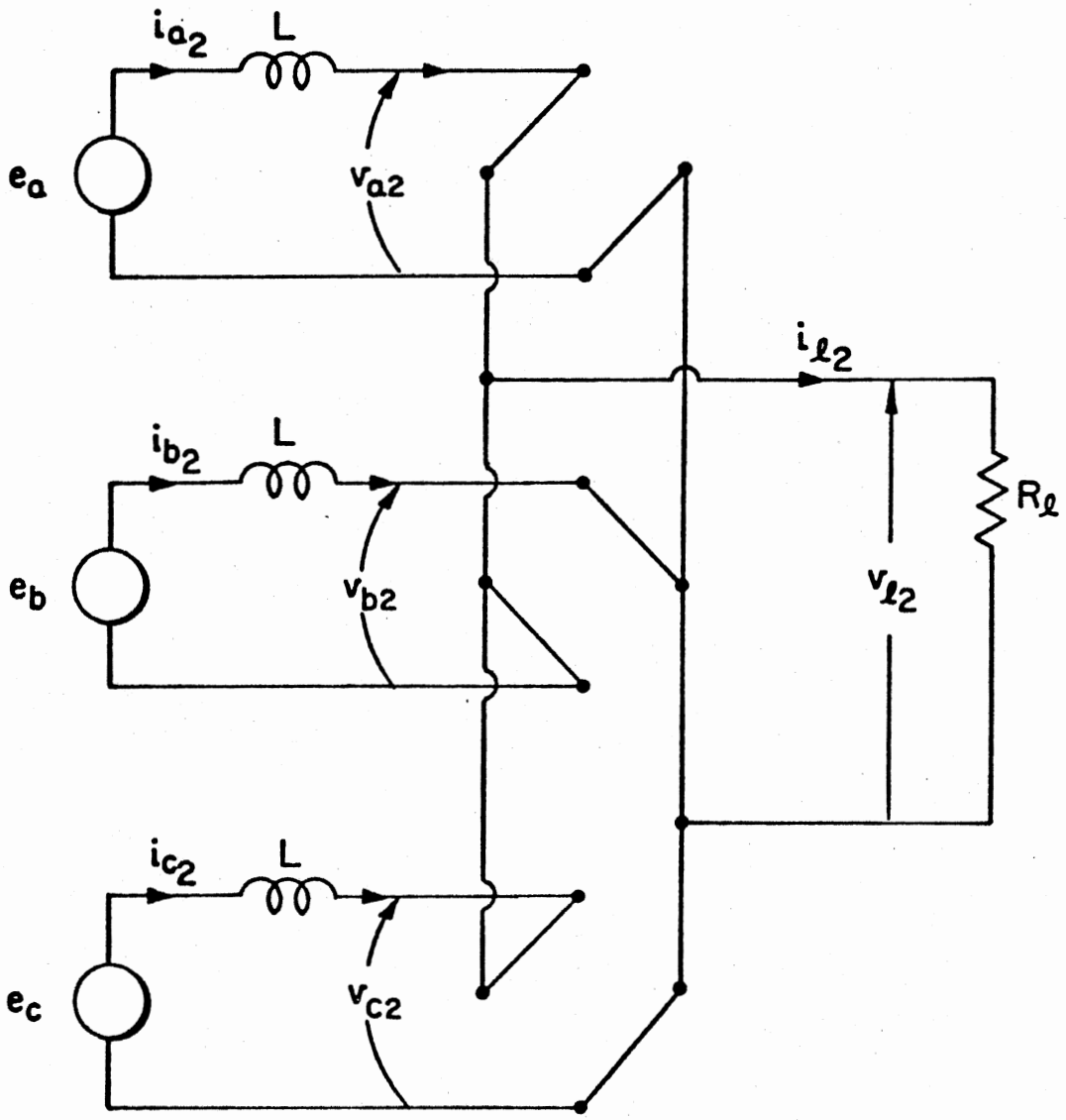

Figure 17. Illustrating the Assumed Status of the System During $\gamma \leq \theta \leq (\pi/3 - \beta)$

$$- \frac{2E}{3}\left(\frac{t_2}{L} + \frac{e^{\frac{-3R_\ell t_2}{L}}}{3R_\ell}\right) + I_{a1} - \frac{I_{\ell 1}}{3} + \frac{2E}{9R_\ell} \tag{3.3.28}$$

The phase-a current at $\omega t_2 = (\pi/3 - \beta - \gamma)$ is given by

$$I_{a2} = \frac{E(\gamma + \beta)(\pi/3 - \beta - \gamma)}{\Theta_1 L\omega} + \frac{E(\pi/3 - \beta - \gamma)^2}{2\Theta_1 L\omega}$$

$$+ \frac{I_{\ell 1}}{3} e^{\frac{-3R_\ell}{\omega L}(\pi/3 - \beta - \gamma)}$$

$$- \frac{2E}{3}\left(\frac{(\pi/3 - \beta - \gamma)}{\omega L} + \frac{e^{\frac{-3R_\ell}{\omega L}(\pi/3 - \beta - \gamma)}}{3R_\ell}\right)$$

$$+ I_{a1} - \frac{I_{\ell 1}}{3} + \frac{2E}{9R_\ell} \tag{3.3.29}$$

During the time interval $0 \leq t_3 \leq (\beta/\omega)$, the circuit equation for phase-a is

$$E - L\frac{di_{a3}}{dt_3} = i_{\ell 3} R_\ell \tag{3.3.30}$$

Substituting for $i_{\ell 3}$ from (3.3.24) in (3.3.30), the solution for i_{a3} with the initial condition $i_{a3}(0^+) = I_{a2}$ is given by

$$i_{a3}(t_3) = \frac{Et_3}{L} + \frac{I_{\ell 2}}{3} e^{\frac{-3R_\ell t_3}{L}}$$

$$- \left(\frac{2E}{3} + \frac{2E\omega L}{9R_\ell \Theta_1} \right) \left(\frac{t_3}{L} + \frac{e^{\frac{-3R_\ell t_3}{L}}}{3R_\ell} \right) + \frac{E\omega t_3^2}{3\Theta_1 L}$$

$$+ I_{a2} - \frac{I_{\ell 2}}{3} + \frac{2E}{9R_\ell} + \frac{2E\omega L}{27\Theta_1 R_\ell^2} \qquad (3.3.31)$$

The phase-a current at $\omega t_3 = \beta$ is given by

$$I_{a3} = \frac{E\beta}{\omega L} + \frac{I_{\ell 2}}{3} e^{\frac{-3R_\ell \beta}{\omega L}}$$

$$- \left(\frac{2E}{3} + \frac{2E\omega L}{9R_\ell \Theta_1} \right) \left(\frac{\beta}{\omega L} + \frac{e^{\frac{-3R_\ell \beta}{\omega L}}}{3R_\ell} \right) + \frac{E\beta^2}{3\Theta_1 L\omega}$$

$$+ I_{a2} - \frac{I_{\ell 2}}{3} + \frac{2E}{9R_\ell} + \frac{2E\omega L}{27\Theta_1 R_\ell^2} \qquad (3.3.32)$$

During the time interval $0 \leq t_4 \leq (\gamma/\omega)$, the circuit equation for phase-a is

$$E - L \frac{di_{a4}}{dt_4} = i_{\ell 4} R_\ell \qquad (3.3.33)$$

Since the load current is periodic with a period $(\pi/3)$, the expression for load current $i_{\ell 4}$ is the same as $i_{\ell 1}$ with a change in time variable from t_1 to t_4. Substituting for $i_{\ell 4}$ in (3.3.33), the solution for i_{a4} with the initial condition $i_{a4}(0^+) = I_{a3}$ is

$$i_{a4}(t_4) = \frac{Et_4}{L} + \frac{I(0)_\ell}{2} e^{\frac{-2R_\ell t_4}{L}}$$

$$- \left(\frac{E}{1} - \frac{E\beta}{2\Theta_1} + \frac{E\omega L}{4\Theta_1 R_\ell}\right)\left(\frac{t_4}{L} + \frac{e^{\frac{-2R_\ell t_4}{L}}}{2R_\ell}\right)$$

$$+ \frac{E\omega t_4^{\,2}}{4\Theta_1 L} + I_{a3} - \frac{I(0)\ell}{2} + \frac{E}{2R_\ell} - \frac{E\beta}{4\Theta_1 R_\ell}$$

$$+ \frac{E\omega L}{8\Theta_1 R_\ell^{\,2}} \qquad (3.3.34)$$

The phase-a current at $\omega t_4 = \gamma$ is given by

$$I_{a4} = \frac{E\gamma}{\omega L} + \frac{I(0)\ell}{2} e^{\frac{-2R_\ell \gamma}{\omega L}}$$

$$- \left(\frac{E}{1} - \frac{E\beta}{2\Theta_1} + \frac{E\omega L}{4\Theta_1 R_\ell}\right)\left(\frac{\gamma}{\omega L} + \frac{e^{\frac{-2R_\ell \gamma}{\omega L}}}{2R_\ell}\right)$$

$$+ \frac{E\gamma^2}{4\Theta_1 \omega L} + I_{a3} - \frac{I(0)\ell}{2} + \frac{E}{2R_\ell} - \frac{E\beta}{4\Theta_1 R_\ell}$$

$$+ \frac{E\omega L}{8\Theta_1 R_\ell^{\,2}} \qquad (3.3.35)$$

During the time interval $0 \leq t_5 \leq (\pi/3 - \beta - \gamma)/\omega$, the circuit equation for phase-a is

$$E - L\frac{di_{a5}}{dt_5} = i_{\ell 5} R_\ell \qquad (3.3.36)$$

The expression for load current $i_{\ell 5}$ is obtained by replacing t_2 with t_5 in equation (3.3.18). Substituting for $i_{\ell 5}$ in (3.3.36), the solution for i_{a5} with initial condition $i_{a5}(0^+) = I_{a4}$ is

$$i_{a5}(t_5) = \frac{Et_5}{L} + \frac{I_{\ell 1}}{3} e^{\frac{-3R_\ell t_5}{L}} - \frac{2E}{3}\left(\frac{t_5}{L} + \frac{e^{\frac{-3R_\ell t_5}{L}}}{3R_\ell}\right)$$

$$+ I_{a4} - \frac{I_{\ell 1}}{3} + \frac{2E}{9R_\ell} \qquad (3.3.37)$$

The phase-a current at $\omega t_5 = (\pi/3 - \beta - \gamma)$ is

$$I_{a5} = \frac{E(\pi/3 - \beta - \gamma)}{\omega L} + \frac{I_{\ell 1}}{3} e^{\frac{-3R_\ell(\pi/3 - \beta - \gamma)}{\omega L}}$$

$$- \frac{2E}{3}\left(\frac{(\pi/3 - \beta - \gamma)}{\omega L} + \frac{e^{\frac{-3R_\ell(\pi/3 - \beta - \gamma)}{\omega L}}}{3R_\ell}\right)$$

$$+ I_{a4} - \frac{I_{\ell 1}}{3} + \frac{2E}{9R_\ell} \qquad (3.3.38)$$

During the interval $0 \leq t_6 \leq (\beta/\omega)$, the circuit equation for phase-a is

$$E - \frac{E\omega t_6}{\Theta_1} - L\frac{di_{a6}}{dt_6} = i_{\ell 6} R_\ell \qquad (3.3.39)$$

The expression for load current $i_{\ell 6}$ is obtained by replacing t_3 with t_6 in equation (3.3.24). Substituting for $i_{\ell 6}$ in (3.3.39), the solution is obtained for i_{a6} with initial condition $i_{a6}(0^+) = I_{a5}$.

$$i_{a6}(t_6) = \frac{Et_6}{L} - \frac{E\omega t_6^2}{2\Theta_1 L} + \frac{I_{\ell 2}}{3} e^{\frac{-3R_\ell t_6}{L}}$$

$$- \left(\frac{2E}{3} + \frac{2E\omega L}{9R_\ell \Theta_1}\right)\left(\frac{t_6}{L} + \frac{e^{\frac{-3R_\ell t_6}{L}}}{3R_\ell}\right) + \frac{E\omega t_6^2}{3\Theta_1 L}$$

$$+ I_{a5} - \frac{I_{\ell 2}}{3} + \frac{2E}{9R_\ell} + \frac{2E\omega L}{27\Theta_1 R_\ell^2} \qquad (3.3.40)$$

The phase-a current at $\omega t_6 = \beta$ is

$$I_{a6} = \frac{E\beta}{\omega L} - \frac{E\beta^2}{2\Theta_1 L\omega} + \frac{I_{\ell 2}}{3} e^{\frac{-3R_\ell \beta}{\omega L}}$$

$$- \left(\frac{2E}{3} + \frac{2E\omega L}{9R_\ell \Theta_1}\right)\left(\frac{\beta}{\omega L} + \frac{e^{\frac{-3R_\ell \beta}{\omega L}}}{3R_\ell}\right) + \frac{E\beta^2}{3\Theta_1 L\omega}$$

$$+ I_{a5} - \frac{I_{\ell 2}}{3} + \frac{2E}{9R_\ell} + \frac{2E\omega L}{27\Theta_1 R_\ell^2} \qquad (3.3.41)$$

During the interval $0 \leq t_7 \leq (\gamma/\omega)$, the phase-a circuit equation is

$$E - \frac{E\beta}{\Theta_1} - \frac{E\omega t_7}{\Theta_1} - L\frac{di_{a7}}{dt_7} = i_{\ell 7} R_\ell \qquad (3.3.42)$$

The expression for $i_{\ell 7}$ is obtained by replacing t_1 with t_7 in (3.3.10). Substituting for $i_{\ell 7}$ in (3.3.42), the solution for i_{a7} with the initial condition $i_{a7}(0^+) = I_{a6}$ to maintain smooth flow of current through L is obtained as follows:

$$i_{a7}(t_7) = \frac{Et_7}{L} - \frac{E\beta t_7}{\Theta_1 L} - \frac{E\omega t_7^2}{2\Theta_1 L} + \frac{I(0)_\ell}{2} e^{\frac{-2R_\ell t_7}{L}}$$

$$- \left(\frac{E}{1} - \frac{E\beta}{2\Theta_1} + \frac{E\omega L}{4\Theta_1 R_\ell}\right)\left(\frac{t_7}{L} + \frac{e^{\frac{-2R_\ell t_7}{L}}}{2R_\ell}\right)$$

$$+ \frac{E\omega t_7^2}{4\Theta_1 L} + I_{a6} - \frac{I(0)\ell}{2} + \frac{E}{2R_\ell} - \frac{E\beta}{4\Theta_1 R_\ell}$$

$$+ \frac{E\omega L}{8\Theta_1 R_\ell^2} \qquad (3.3.43)$$

The phase-a current at $\omega t_7 = \gamma$ is

$$I_{a7} = \frac{E\gamma}{\omega L} - \frac{E\beta\gamma}{\Theta_1 L\omega} - \frac{E\gamma^2}{2\Theta_1 L\omega} + \frac{I(0)\ell}{2} e^{\frac{-2R_\ell\gamma}{\omega L}}$$

$$- \left(\frac{E}{1} - \frac{E\beta}{2\Theta_1} + \frac{E\omega L}{4\Theta_1 R_\ell}\right)\left(\frac{\gamma}{\omega L} + \frac{e^{\frac{-2R_\ell\gamma}{\omega L}}}{2R_\ell}\right)$$

$$+ \frac{E\gamma^2}{4\Theta_1 L\omega} + I_{a6} - \frac{I(0)\ell}{2} + \frac{E}{2R_\ell} - \frac{E\beta}{4\Theta_1 R_\ell}$$

$$+ \frac{E\omega L}{8\Theta_1 R_\ell^2} \qquad (3.3.44)$$

During the time interval $0 \leq t_8 \leq (\pi/3 - \beta - \gamma)/\omega$, the circuit equation for phase-a is

$$E - \frac{E(\gamma+\beta)}{\Theta_1} - \frac{E\omega t_8}{\Theta_1} - L\frac{di_{a8}}{dt_8} = i_{\ell 8} R_\ell \qquad (3.3.45)$$

The expression for $i_{\ell 8}$ is the same as $i_{\ell 2}$ with a change in time variable from t_2 to t_8. Substituting for $i_{\ell 8}$ in (3.3.45) the solution for i_{a8} is obtained with the initial condition $i_{a8}(0^+) = I_{a7}$ as

$$i_{a8}(t_8) = \frac{Et_8}{L} - \frac{E(\gamma+\beta)t_8}{\Theta_1 L} - \frac{E\omega t_8^2}{2\Theta_1 L} + \frac{I_{\ell 1}}{3} e^{\frac{-3R_\ell t_8}{L}}$$

$$- \frac{2E}{3}\left(\frac{t_8}{L} + \frac{e^{\frac{-3R_\ell t_8}{L}}}{3R_\ell}\right) + I_{a7} - \frac{I_{\ell 1}}{3} + \frac{2E}{9R_\ell} \tag{3.3.46}$$

The phase-a current at $\omega t_8 = (\pi/3 - \beta - \gamma)$ is

$$I_{a8} = \frac{E(\pi/3 - \beta - \gamma)}{\omega L} - \frac{E(\gamma + \beta)(\pi/3 - \beta - \gamma)}{\Theta_1 L\omega}$$

$$- \frac{E(\pi/3 - \beta - \gamma)^2}{2\Theta_1 L\omega} + \frac{I_{\ell 1}}{3} e^{\frac{-3R_\ell(\pi/3 - \beta - \gamma)}{\omega L}}$$

$$- \frac{2E}{3}\left(\frac{(\pi/3 - \beta - \gamma)}{\omega L} + \frac{e^{\frac{-3R_\ell(\pi/3 - \beta - \gamma)}{\omega L}}}{3R_\ell}\right)$$

$$+ I_{a7} - \frac{I_{\ell 1}}{3} + \frac{2E}{9R_\ell} \tag{3.3.47}$$

During the time interval $0 \leq t_9 \leq (\beta/\omega)$, the circuit equation for phase-a is

$$- \frac{E\omega t_9}{\Theta_1} - L\frac{di_{a9}}{dt_9} = i_{\ell 9} R_\ell \tag{3.3.48}$$

The expression for $i_{\ell 9}$ is the same as $i_{\ell 3}$ with a change in time variable from t_3 to t_9. Substituting for $i_{\ell 9}$ in (3.3.48) and solving for i_{a9} with the initial condition $i_{a9}(0^+) = I_{a8}$ yields

$$i_{a9}(t_9) = - \frac{E\omega t_9^2}{2\Theta_1 L} + \frac{I_{\ell 2}}{3} e^{\frac{-3R_\ell t_9}{L}}$$

$$- \left(\frac{2E}{3} + \frac{2E\omega L}{9R_\ell \Theta_1}\right)\left(\frac{t_9}{L} + \frac{e^{\frac{-3R_\ell t_9}{L}}}{3R_\ell}\right) + \frac{E\omega t_9^2}{3\Theta_1 L}$$

$$+ I_{a8} - \frac{I_{\ell 2}}{3} + \frac{2E}{9R_\ell} + \frac{2E\omega L}{27\Theta_1 R_\ell^2} \qquad (3.3.49)$$

The phase-a current at $\omega t_9 = \beta$ is

$$I_{a9} = - \frac{E\beta^2}{2\Theta_1 L\omega} + \frac{I_{\ell 2}}{3} e^{\frac{-3R_\ell \beta}{\omega L}}$$

$$- \left(\frac{2E}{3} + \frac{2E\omega L}{9R_\ell \Theta_1}\right)\left(\frac{\beta}{\omega L} + \frac{e^{\frac{-3R_\ell \beta}{\omega L}}}{3R_\ell}\right) + \frac{E\beta^2}{3\Theta_1 L\omega}$$

$$+ I_{a8} - \frac{I_{\ell 2}}{3} + \frac{2E}{9R_\ell} + \frac{2E\omega L}{27\Theta_1 R_\ell^2} \qquad (3.3.50)$$

The phase current I_{a9} at $\omega t_9 = \beta$ is equal to zero as shown in Figure 12(a) at $\Theta = \pi$.

3.3.1.4 Determination of Angles 'γ' and 'β'. To evaluate the two angles 'γ' and 'β', the following two boundary conditions are applied.

$$i_{\ell 1}(0^+) = -i_{b1}(0^+) + i_{c1}(0^+) \qquad (3.3.51)$$

$$i_{\ell 1}(\gamma/\omega^+)\, R_\ell = v_{a1}(\gamma/\omega^+) \qquad (3.3.52)$$

The load current at $\omega t_1 = 0$ given by $I(0)_\ell$ can be determined from (3.3.26) and is represented by

$$I(0)_\ell = -i_{b1}(0^+) + i_{c1}(0^+) \qquad (3.3.53)$$

From the symmetry of current and voltage waveforms, it can be observed from Figure 12(a) that

$$-i_{b1}(0^+) = I_{a3} \tag{3.3.54}$$

$$i_{c1}(0^+) = I_{a6} \tag{3.3.55}$$

Therefore,

$$I(0)\ell = I_{a3} + I_{a6} \tag{3.3.56}$$

Substituting the expressions obtained for I_{a3} and I_{a6} in (3.3.56), an expression involving load current $I(0)\ell$ at $\omega t_1 = 0$ is obtained as follows:

$$\begin{aligned} I(0)\ell\left(1 + e^{\frac{-2R_\ell\gamma}{\omega L}}\right) = {} & \frac{E}{\omega L}\left[\frac{2\beta}{1} + \frac{\beta^2}{\Theta_1} + \frac{\gamma^2}{2\Theta_1} + \frac{4(\gamma+\beta)(\pi/3-\beta-\gamma)}{\Theta_1}\right. \\ & \left. + \frac{2(\pi/3-\beta-\gamma)^2}{\Theta_1} - \frac{2(\pi/3-\beta-\gamma)}{1} + \frac{\beta\gamma}{\Theta_1}\right] \\ & + \frac{E\gamma}{2\Theta_1 R_\ell} + 2\left(\frac{V_o}{1} + \frac{E\beta}{\Theta_1}\right)\sqrt{\frac{C}{L}}\ \sin\frac{\gamma}{\omega\sqrt{LC}} \\ & + \frac{2E\omega C}{\Theta_1}\left(1 - \cos\frac{\gamma}{\omega\sqrt{LC}}\right) \\ & + \left(\frac{E}{R_\ell} - \frac{E\beta}{2\Theta_1 R_\ell} + \frac{E\omega L}{4\Theta_1 R_\ell^2}\right)\left(e^{\frac{-2R_\ell\gamma}{\omega L}} - 1\right) \end{aligned} \tag{3.3.57}$$

where $V_o = I(0)\ell\ R_\ell$.

Substituting for $I(0)\ell$ from equation (3.3.26) into (3.3.57), the following relationship involving circuit parameter ratios (X_L/R_ℓ),

(X_L/X_C) and angles γ and β is obtained.

$$\frac{F\left(1 + e^{\frac{-2R_\ell\gamma}{X_L}} - 2\frac{R_\ell}{X_L}\sqrt{X_L/X_C}\ \sin\frac{\gamma}{\sqrt{X_L/X_C}}\right)}{\left(1 - e^{\frac{R_\ell(\gamma - \pi)}{X_L}} - \frac{R_\ell}{X_L}\sqrt{X_L/X_C}\ \sin\frac{\gamma}{\sqrt{X_L/X_C}}\ e^{\frac{-3R_\ell(\pi/3 - \gamma)}{X_L}}\right)}$$

$$= \frac{2\beta}{1} + \frac{\beta^2}{\Theta_1} + \frac{\gamma^2}{2\Theta_1} + \frac{4(\gamma + \beta)(\pi/3 - \beta - \gamma)}{\Theta_1}$$

$$+ \frac{2(\pi/3 - \beta - \gamma)^2}{\Theta_1} - \frac{2(\pi/3 - \beta - \gamma)}{1}$$

$$+ \frac{\gamma X_L}{2\Theta_1 R_\ell} + \frac{2\beta}{\Theta_1}\sqrt{X_L/X_C}\ \sin\frac{\gamma}{\sqrt{X_L/X_C}}$$

$$+ \frac{2X_L/X_C}{\Theta_1}\left(1 - \cos\frac{\gamma}{\sqrt{X_L/X_C}}\right) + \frac{\beta\gamma}{\Theta_1}$$

$$+ \left(\frac{X_L}{R_\ell} - \frac{\beta X_L}{2\Theta_1 R_\ell} + \frac{(X_L)^2}{4\Theta_1 R_\ell^2}\right)\left(e^{\frac{-2R_\ell\gamma}{X_L}} - 1\right) \qquad (3.3.58)$$

in which

$$F = \left(\frac{X_L}{R_\ell} - \frac{\beta X_L}{2\Theta_1 R_\ell} + \frac{(X_L)^2}{4\Theta_1 R_\ell^2}\right)$$

$$\cdot \left(e^{\frac{-3R_\ell(\pi/3 - \gamma)}{X_L}} - e^{\frac{R_\ell(\gamma - \pi)}{X_L}}\right)$$

$$+\left[\frac{\beta\sqrt{X_L/X_C}}{\Theta_1}\sin\frac{\gamma}{\sqrt{X_L/X_C}}\right.$$

$$\left.+\frac{X_L/X_C}{\Theta_1}\left(1-\cos\frac{\gamma}{\sqrt{X_L/X_C}}\right)-\frac{\gamma X_L}{2\Theta_1 R_\ell}-\frac{2X_L}{3R_\ell}\right]$$

$$\cdot e^{\frac{-3R_\ell(\pi/3-\gamma)}{X_L}}+\frac{2(X_L)^2}{9\Theta_1 R_\ell^2}\left(1-e^{\frac{-3R_\ell\beta}{X_L}}\right)$$

$$+\frac{2X_L}{3R_\ell}\left(1-\frac{\beta}{\Theta_1}\right) \qquad (3.3.59)$$

$$\Theta_1 = \pi/3$$

$$X_L = \omega L$$

$$\text{and } X_C = 1/\omega C$$

At $\omega t_1 = (\gamma^+)$, phase-a starts conducting through the load. Therefore at $\omega t_1 = \gamma^+$, the bridge-input voltage V_{a1} is equal to the load voltage $I_{\ell 1} R_\ell$.

$$I_{\ell 1} R_\ell = V_{a1} \qquad (3.3.60)$$

Substituting for V_{a1} and $I_{\ell 1}$ from equations (3.3.5) and (3.3.13) into (3.3.60) and substituting for $I(0)_\ell$ from equation (3.3.26), a transcendental expression involving angles γ, β and circuit parameter ratios (X_L/R_ℓ) and (X_L/X_C) is obtained and it is given below.

$$\frac{P\left(e^{\frac{-2R_\ell\gamma}{X_L}} + \frac{R_\ell\sqrt{X_L/X_C}}{X_L}\sin\frac{\gamma}{\sqrt{X_L/X_C}} + \cos\frac{\gamma}{\sqrt{X_L/X_C}}\right)}{\left(1 - e^{\frac{R_\ell(\gamma-\pi)}{X_L}} - \frac{R_\ell\sqrt{X_L/X_C}}{X_L}\sin\frac{\gamma}{\sqrt{X_L/X_C}}\, e^{\frac{-3R_\ell(\pi/3-\gamma)}{X_L}}\right)}$$

$$+\left(1 - \frac{\beta}{2\Theta_1} + \frac{X_L}{4\Theta_1 R_\ell}\right)\left(1 - e^{\frac{-2R_\ell\gamma}{X_L}}\right) - \frac{\gamma}{2\Theta_1} + \frac{\beta R_\ell\sqrt{X_L/X_C}}{\Theta_1 X_L}\sin\frac{\gamma}{\sqrt{X_L/X_C}}$$

$$+ (X_L/X_C)\frac{R_\ell}{X_L\Theta_1}\left(1 - \cos\frac{\gamma}{\sqrt{X_L/X_C}}\right)$$

$$= \frac{(\beta+\gamma)}{\Theta_1} - \frac{\beta}{\Theta_1}\cos\frac{\gamma}{\sqrt{X_L/X_C}}$$

$$- \frac{\sqrt{X_L/X_C}}{\Theta_1}\sin\frac{\gamma}{\sqrt{X_L/X_C}} \qquad (3.3.61)$$

where

$$\Theta_1 = \pi/3$$

$$X_L = \omega L$$

$$X_C = 1/\omega C \quad \text{and}$$

$$P = \left(1 - \frac{\beta}{2\Theta_1} + \frac{X_L}{4\Theta_1 R_\ell}\right)$$

$$\left(e^{\frac{-3R_\ell(\pi/3-\gamma)}{X_L}} - e^{\frac{R_\ell(\gamma-\pi)}{X_L}}\right)$$

$$+\left[\frac{\beta R_\ell \sqrt{X_L/X_C}}{\Theta_1 X_L}\sin\frac{\gamma}{\sqrt{X_L/X_C}}\right.$$

$$+\frac{R_\ell(X_L/X_C)}{X_L\Theta_1}\left(1-\cos\frac{\gamma}{\sqrt{X_L/X_C}}\right)$$

$$\left.-\frac{2}{3}-\frac{\gamma}{2\Theta_1}\right]e^{\frac{-3R_\ell(\pi/3-\gamma)}{X_L}}$$

$$+\frac{2X_L}{9R_\ell\Theta_1}\left(1-e^{\frac{-3R_\ell\beta}{X_L}}\right)+\frac{2}{3}\left(1-\frac{\beta}{\Theta_1}\right)$$

(3.3.62)

The non-linear equations (3.3.58) and (3.3.61) involving the two unknown angles γ and β are solved simultaneously using standard sub-routines [40] and an IBM 370/158 digital computer. A set of values for angles γ and β is obtained by varying the parameter ratios (X_L/R_ℓ) and (X_L/X_C). The equations in this section are valid for the range of $(\gamma + \beta)$ given by $0 \leq (\gamma + \beta) \leq (\pi/3)$. In the evaluation of angles γ and β, the maximum value for the sum of angles γ and β in each iteration is limited to $(\pi/3)$.

Calculated results are presented in Figure 18 as a family of curves showing the values of γ and β for different parameter ratios (X_L/R_ℓ) and (X_L/X_C). The ratio (X_L/X_C) approaching zero corresponds to the case $C = 0$. For this case, the angle γ should be zero. The waveforms of phase-a bridge-input voltage v_a, phase current i_a and load current i_ℓ for $(X_L/R_\ell) = 2.2$; $(X_L/X_C) = 0.08$ (with corresponding angles $\beta = 33.4°$ and $\gamma = 26.4°$) are shown in Figure 19. The two components of phase

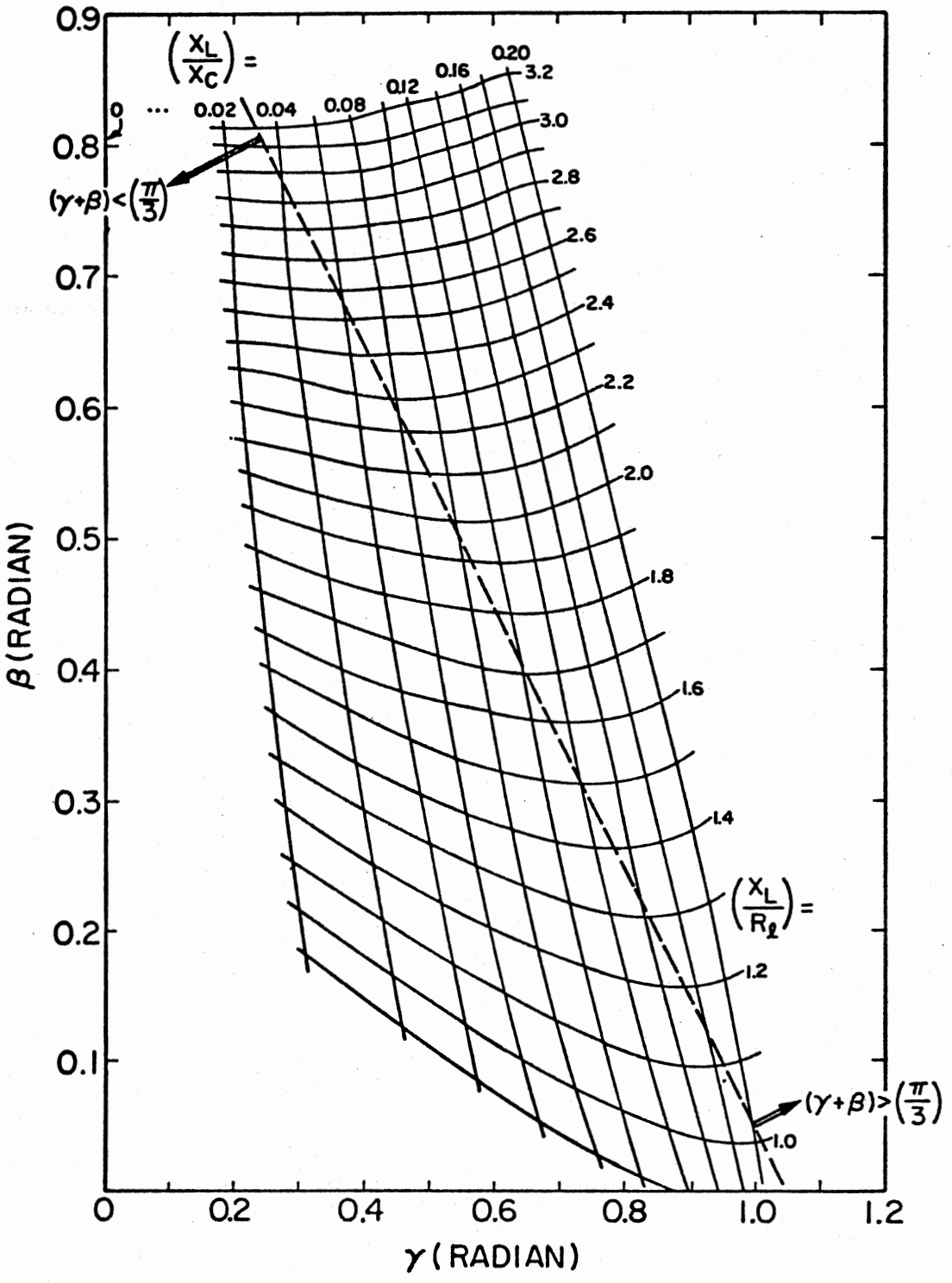

Figure 18. Theoretical Values of γ and β

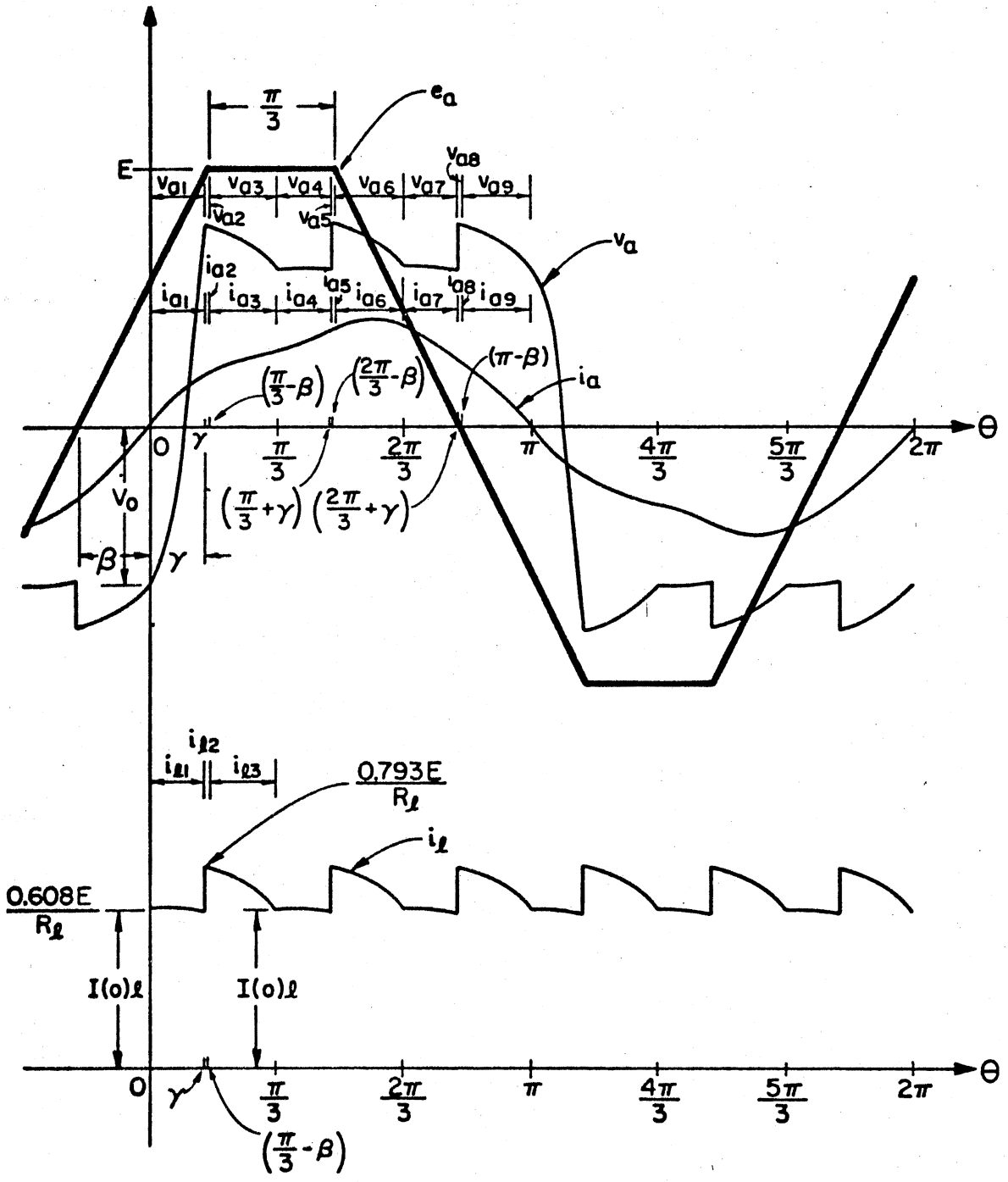

Figure 19. e_a, v_a, i_a, and i_ℓ Waveforms for $X_L/R_\ell = 2.2$, $X_L/X_C = 0.08$ and $(\gamma+\beta) < (\pi/3)$

current, namely the capacitor current and the bridge input current, are shown separately for the purpose of illustration in Figure 20 along with phase current i_a.

3.3.2 Case (B) $(\pi/3) \leq (\gamma + \beta) \leq (2\pi/3)$

Figure 13 shows the general nature of the voltage and current waveforms for this case. The start of the decoupling of a particular phase is assumed to be within the ramp portion of the source voltage waveform. This is a valid assumption for the normal operating range of the circuit parameter ratios (X_L/R_ℓ) and (X_L/X_C). The range for β in this case is given by $0 < \beta \leq (\pi/3)$. It can be seen from Figure 21 that the decoupled duration of phase-a continues well within the flat portion of the source voltage waveform. Intervals 1-2, 4-5 and 7-8 correspond to the decoupling durations of phases a, c and b respectively. Intervals 3, 6 and 9 correspond to simultaneous conduction of all three bridges. During the period a bridge is decoupled from the other two, the series circuit consisting of commutating inductance L and the bridge-input capacitor C provides the closed path necessary for current flow. The voltage across the capacitor changes from $-V_o$ to V_{a2} during the decoupled duration. At $\Theta = \gamma$ the bridge input voltage is equal to the load voltage and the bridge starts conducting through the load with the current through the capacitor instantaneously transferred to the load. This accounts for the jump in the load current (see Figure 13(b)) at $\Theta = \gamma$. It can be observed that though there is a jump in the load current at the instant the decoupled bridge starts conducting, the current flow through the commutating inductance L remains continuous. The non-sinusoidal nature of the input waveform requires subdividing the half-period (0 to π) into

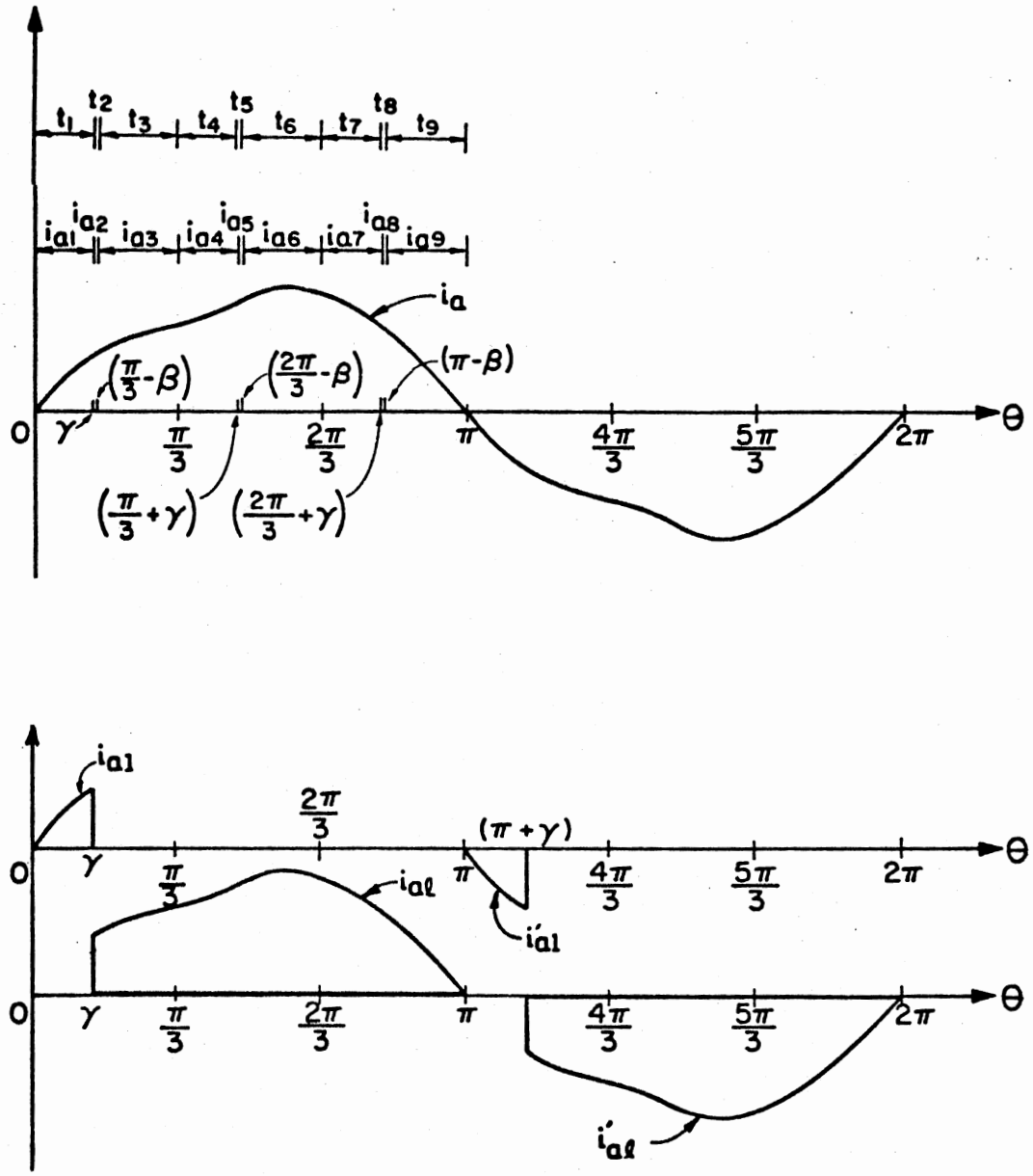

Figure 20. Theoretical Waveforms of Phase-Current i_a, Capacitor Current i_{a1} and Bridge-Input Current $i_{a\ell}$ for Case (A)

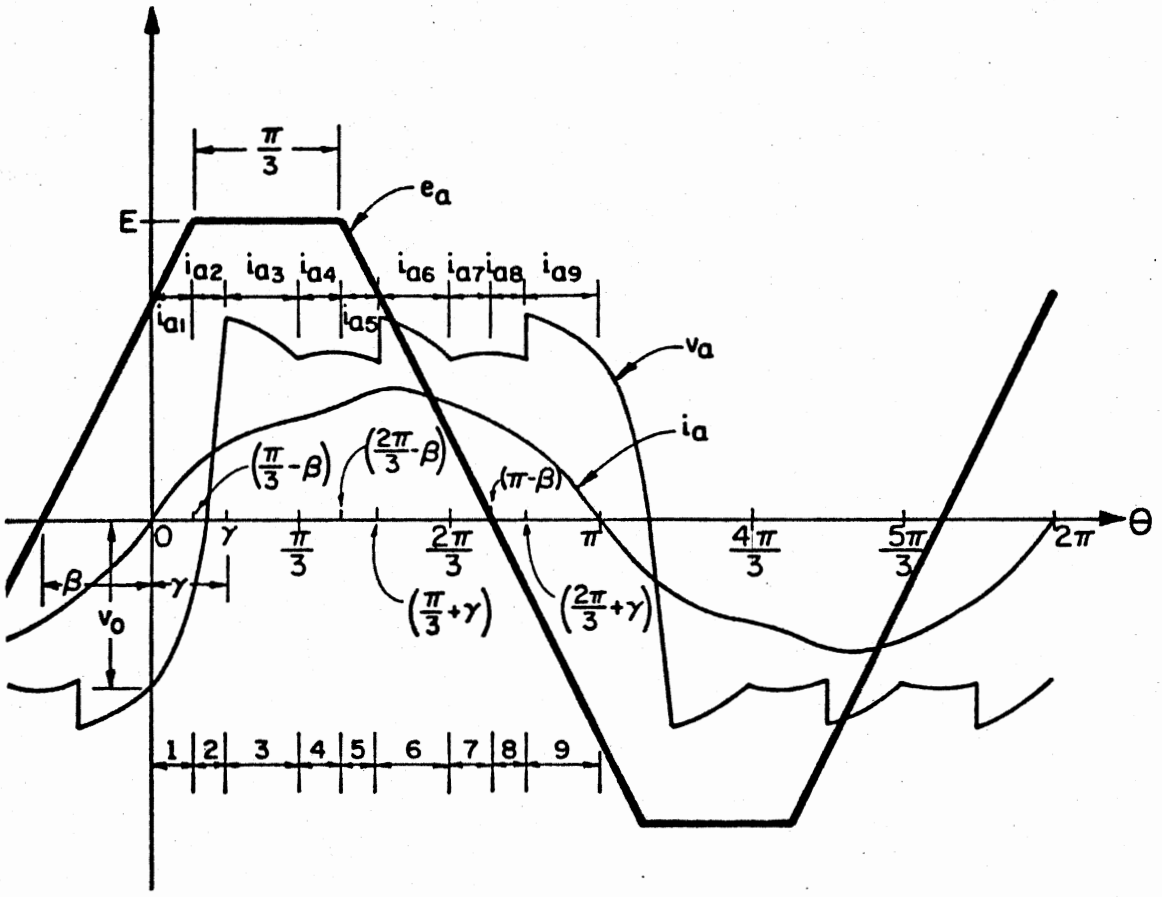

Figure 21. Typical Phase-a Waveforms for Case (B), ($X_L/X_C \simeq 0.14$)

nine segments as before for the purpose of analysis. The analysis for this case is very similar to the one presented for case (A).

After obtaining the expressions for load current i_ℓ and phase current i_a over one half-period, the following boundary conditions are applied to obtain the two equations necessary to evaluate the angles γ and β.

$$i_{\ell 1}(0^+) = -i_{b1}(0^+) + i_{c1}(0^+) \tag{3.3.63}$$

$$i_{\ell 2}(\gamma/\omega^+)\, R_\ell = v_{a2}(\gamma/\omega^-) \tag{3.3.64}$$

$$i_{\ell 1}(0^+) = i_{\ell 3}(\pi/3\omega^-) \tag{3.3.65}$$

$$V_o = i_{\ell 1}(0^+)\, R_\ell \tag{3.3.66}$$

The two equations to be solved simultaneously to obtain γ and β for this case are given below.

$$\frac{G_1\left(1 + e^{\frac{-2R_\ell\gamma}{X_L}} - \frac{2R_\ell\sqrt{X_L/X_C}}{X_L}\sin\frac{\gamma}{\sqrt{X_L/X_C}}\right)}{\left(1 - e^{\frac{R_\ell(\gamma-\pi)}{X_L}} - \frac{R_\ell\sqrt{X_L/X_C}}{X_L}\sin\frac{\gamma}{\sqrt{X_L/X_C}}\; e^{\frac{-3R_\ell(\pi/3-\gamma)}{X_L}}\right)}$$

$$= \frac{R_\ell}{\Theta_1 X_L}\left[(\pi/3 - \gamma)^2 - 2(\gamma + \beta - \pi/3)(\pi/3 - \gamma)\right.$$

$$+ \frac{(\pi/3 - \beta)^2}{2} + \beta(\pi/3 - \beta)$$

$$+ 4(\gamma + \beta)(\pi/3 - \gamma)$$

$$\left. + 2\beta\sqrt{X_L/X_C}\sin\frac{\gamma}{\sqrt{X_L/X_C}}\right]$$

$$+ 2(X_L/X_C)$$

$$\left\{\left(1 - \frac{\cos(\pi/3 - \beta)}{\sqrt{X_L/X_C}}\right)\frac{\cos(\gamma + \beta - \pi/3)}{\sqrt{X_L/X_C}}\right.$$

$$\left. + \frac{\sin(\pi/3 - \beta)}{\sqrt{X_L/X_C}}\left(\frac{\sin(\gamma + \beta - \pi/3)}{\sqrt{X_L/X_C}}\right)\right\}\Bigg]$$

$$+ (\gamma + \beta - \pi/3)\left(\frac{R_\ell}{X_L} + \frac{1}{\Theta_1}\right) - \frac{1}{2}$$

$$+ \frac{X_L}{2\Theta_1 R_\ell}\left(\frac{e^{\frac{-2R_\ell(\gamma + \beta - \pi/3)}{X_L}}}{2} - 1\right)$$

$$+ \left(1 - \frac{\beta}{2\Theta_1} + \frac{X_L}{4\Theta_1 R_\ell}\right)e^{\frac{-2R_\ell\gamma}{X_L}}$$

$$- \frac{2(\pi/3 - \gamma)R_\ell}{X_L} \qquad (3.3.67)$$

$$G_1\left\{e^{\frac{-2R_\ell\gamma}{X_L}} + \frac{R_\ell}{X_L}\sqrt{X_L/X_C}\sin\frac{\gamma}{\sqrt{X_L/X_C}} - \frac{\sin(\pi/3 - \beta)}{\sqrt{X_L/X_C}}\,\frac{\sin(\gamma + \beta - \pi/3)}{\sqrt{X_L/X_C}}\right.$$

$$\left. + \frac{\cos(\pi/3 - \beta)}{\sqrt{X_L/X_C}}\,\frac{\cos(\gamma + \beta - \pi/3)}{\sqrt{X_L/X_C}}\right\} - \frac{(\pi/3 - \beta)}{2\Theta_1}e^{\frac{-2R_\ell(\gamma + \beta - \pi/3)}{X_L}}$$

$$+ \left(1 - \frac{\beta}{2\Theta_1} + \frac{X_L}{4\Theta_1 R_\ell}\right)\left(e^{\frac{-2R_\ell(\gamma + \beta - \pi/3)}{X_L}} - e^{\frac{-2R_\ell\gamma}{X_L}}\right)$$

$$+\left(\frac{1}{2}+\frac{X_L}{2\Theta_1 R_\ell}\right)\left(1-e^{\frac{-2R_\ell(\gamma+\beta-\pi/3)}{X_L}}\right)-(\gamma+\beta-\pi/3)/\Theta_1$$

$$+\frac{\beta}{\Theta_1}\frac{R_\ell}{X_L}\sqrt{X_L/X_C}\ \sin\frac{\gamma}{\sqrt{X_L/X_C}}+\frac{(X_L/X_C)}{\Theta_1}\frac{R_\ell}{X_L}$$

$$\left\{\left(1-\frac{\cos(\pi/3-\beta)}{\sqrt{X_L/X_C}}\right)\frac{\cos(\gamma+\beta-\pi/3)}{\sqrt{X_L/X_C}}+\frac{\sin(\pi/3-\beta)}{\sqrt{X_L/X_C}}\frac{\sin(\gamma+\beta-\pi/3)}{\sqrt{X_L/X_C}}\right\}$$

$$=1+\frac{\beta}{\Theta_1}\frac{\sin(\pi/3-\beta)}{\sqrt{X_L/X_C}}\frac{\sin(\gamma+\beta-\pi/3)}{\sqrt{X_L/X_C}}$$

$$+\frac{\sqrt{X_L/X_C}}{\Theta_1}\left(1-\frac{\cos(\pi/3-\beta)}{\sqrt{X_L/X_C}}\right)$$

$$\cdot\frac{\sin(\gamma+\beta-\pi/3)}{\sqrt{X_L/X_C}}$$

$$-\frac{\beta}{\Theta_1}\frac{\cos(\pi/3-\beta)}{\sqrt{X_L/X_C}}\frac{\cos(\gamma+\beta-\pi/3)}{\sqrt{X_L/X_C}}$$

$$-\frac{\sqrt{X_L/X_C}}{\Theta_1}\frac{\sin(\pi/3-\beta)}{\sqrt{X_L/X_C}}\frac{\cos(\gamma+\beta-\pi/3)}{\sqrt{X_L/X_C}}$$

(3.3.68)

where

$$G_1=\left(1-\frac{\beta}{2\Theta_1}+\frac{X_L}{4\Theta_1 R_\ell}\right)$$

$$\cdot\left(e^{\frac{R_\ell(\gamma-\pi/3-2\beta)}{X_L}}-e^{\frac{R_\ell(\gamma-\pi)}{X_L}}\right)$$

$$- \frac{(\pi/3 - \beta)}{2\Theta_1} e^{\frac{R_\ell(\gamma - \pi/3 - 2\beta)}{X_L}}$$

$$- \frac{(\gamma + \beta - \pi/3)}{\Theta_1} e^{\frac{-3R_\ell(\pi/3 - \gamma)}{X_L}}$$

$$+ \left(\frac{1}{2} + \frac{X_L}{2\Theta_1 R_\ell}\right)$$

$$\cdot \left(e^{\frac{-3R_\ell(\pi/3 - \gamma)}{X_L}} - e^{\frac{R_\ell(\gamma - \pi/3 - 2\beta)}{X_L}} \right)$$

$$+ \left(\frac{4}{3} - \frac{2(\gamma + \beta)}{3\Theta_1} + \frac{2X_L}{9\Theta_1 R_\ell}\right)$$

$$\cdot \left(1 - e^{\frac{-3R_\ell(\pi/3 - \gamma)}{X_L}}\right) - \frac{2(\pi/3 - \gamma)}{3\Theta_1}$$

$$+ \frac{\beta}{\Theta_1} \frac{R_\ell}{X_L} \sqrt{X_L/X_C} \sin \frac{\gamma}{\sqrt{X_L/X_C}} e^{\frac{-3R_\ell(\pi/3 - \gamma)}{X_L}}$$

$$+ e^{\frac{-3R_\ell(\pi/3 - \gamma)}{X_L}} \frac{(X_L/X_C)}{\Theta_1} \frac{R_\ell}{X_L}$$

$$\cdot \left\{ \left(1 - \frac{\cos(\pi/3 - \beta)}{\sqrt{X_L/X_C}}\right) \frac{\cos(\gamma + \beta - \pi/3)}{\sqrt{X_L/X_C}} \right.$$

$$\left. + \frac{\sin(\pi/3 - \beta)}{\sqrt{X_L/X_C}} \frac{\sin(\gamma + \beta - \pi/3)}{\sqrt{X_L/X_C}} \right\}$$

(3.3.69)

$$\theta_1 = \pi/3$$

$$X_L = \omega L$$

and $$X_C = 1/\omega C$$

The non-linear algebraic equations (3.3.67) and (3.3.68) involving γ and β are solved using standard sub-routines and an IBM 370 digital computer. A set of values for angles γ and β is obtained by varying the parameter ratio (X_L/R_ℓ) and (X_L/X_C). The equations in the present analysis are valid for the range of $(\gamma + \beta)$ given by $\pi/3 \leq (\gamma + \beta) \leq (2\pi/3)$ and for values of β between 0 and $(\pi/3)$.

Calculated results are plotted in Figure 18 as a family of curves for $(\gamma + \beta) > \pi/3$ showing the values of γ and β for different parameter ratios (X_L/R_ℓ) and (X_L/X_C). The waveforms of phase-a bridge input voltage v_a, phase current i_a and load current i_ℓ for $(X_L/R_\ell) = 3.0$ and $(X_L/X_C) = 0.14$ (with corresponding angles $\beta = 45.5°$ and $\gamma = 30.6°$) are shown in Figure 22.

3.4 Results and Discussion

Theoretical values of angles γ and β are plotted in Figure 18 as a function of the circuit parameter ratios (X_L/R_ℓ) and (X_L/X_C). Two ranges of values for the sum of angles γ and β, given by $0 < (\gamma + \beta) \leq (\pi/3)$ and $(\pi/3) \leq (\gamma + \beta) \leq (2\pi/3)$, have been considered. In the analysis of the range for $(\gamma + \beta)$ given by $\pi/3 \leq (\gamma + \beta) \leq (2\pi/3)$, the beginning of decoupling of a phase is assumed to be within the ramp portion of the source voltage waveform. Therefore, the variation of β in this case is limited to the range bounded by 0 and $(\pi/3)$.

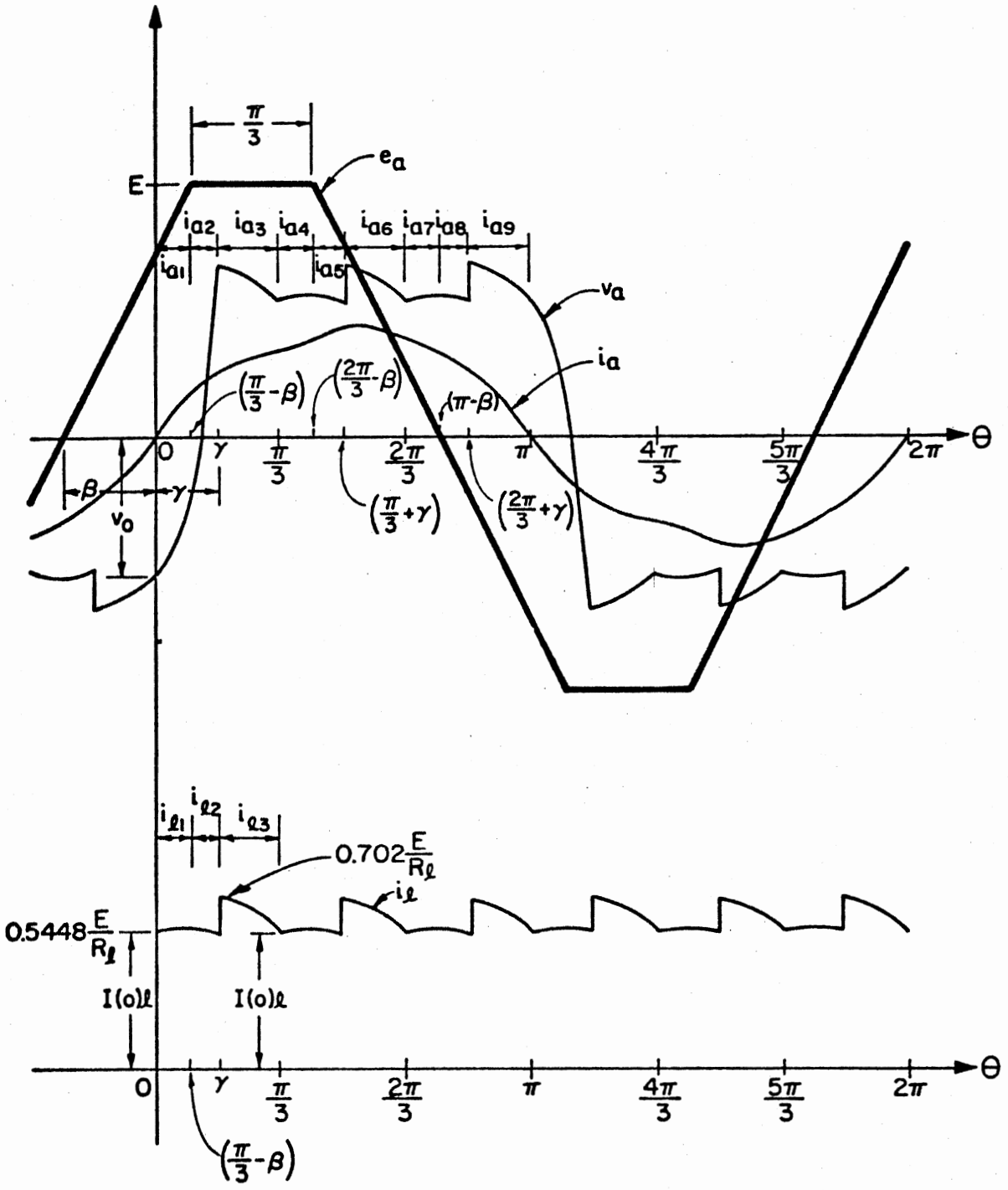

Figure 22. e_a, v_a, i_a, and i_ℓ Waveforms for $(X_L/R_\ell) = 3.0$, $(X_L/X_C) = 0.14$ and $(\gamma+\beta)>(\pi/3)$

The "on" and "off" durations of various diode pairs depend on the angles 'γ' and 'β', which in turn depend on the load resistance R_ℓ, the commutating inductance L, the bridge-input capacitance C and the source voltage frequency f. For values of (X_L/R_ℓ) and (X_L/X_C) in the vicinity of 1.3 and 0.04 respectively, the sum of angles γ and β will be less than $(\pi/3)$. In this region it can be observed from Figure 18 that angle β increases with a decrease in load resistance R_ℓ and decreases with an increase in capacitance C. For a given parameter ratio (X_L/R_ℓ), a variation in (X_L/X_C) gives different values for γ and β. Around the region $(\gamma + \beta) = (\pi/3)$, it can be seen from Figure 18 that the variation of β with parameter ratio (X_L/X_C) is minimum. A minimum value for β, for a given parameter ratio (X_L/R_ℓ) occurs in the region where $(\gamma + \beta)$ is approximately equal to $(\pi/3)$.

For values of (X_L/R_ℓ) and (X_L/X_C) in the vicinity of 2.0 and 0.18 respectively, the sum of angles γ and β will be greater than $(\pi/3)$. In this region, angle β increases with an increase in capacitance C and decreases with an increase in load resistance R_ℓ.

The angle γ increases with an increasing value of load resistance R_ℓ and an increasing value of capacitance C.

For a given parameter ratio (X_L/R_ℓ), the parameter ratio (X_L/X_C) corresponding to the cases (A) and (B) for $(\gamma + \beta) = \pi/3$ should be the same. This has been verified for different ratios of (X_L/R_ℓ) by separately setting $(\gamma + \beta) = \pi/3$ in the respective non-linear algebraic equations. The ratio (X_L/X_C) approaching zero corresponds to the case C = 0. For this case, $\gamma = 0$. It can also be seen that with $(X_L/R_\ell) = 0.9$, the maximum allowable ratio for (X_L/X_C) is 0.13 to keep γ and β positive.

The phase-a bridge-input voltage v_a, source voltage e_a, phase current i_a and the load current i_ℓ waveforms are shown in Figures 19 and 22 for the cases (A) and (B) respectively. The effect of adding capacitors at bridge inputs on the bridge-input voltage v_a can be seen by comparing the bridge-input voltage waveforms in Figure 10 and in Figure 19. With no capacitors, conduction is transferred from diode pair 2 to diode pair 1 at the instant of switching. This results in a bridge input voltage which is essentially a rectangular wave. But with capacitors present, when conduction in diodes 2-2 stops at $t = 0^-$, phase-a gets decoupled from the other two phases. The transfer of conduction from one diode pair to the other of any one bridge is associated with decoupling of that bridge from the other two for a duration denoted as (γ/ω). The bridge-input voltage changes from $-V_o$ to V_{a1} or V_{a2} [depending on case (A) or case (B)] during the decoupled duration of phase-a. The bridge-input voltage will swing above and below the source voltage under light load conditions (large R_ℓ) and/or for large value of capacitance. Similar behavior was observed with sinusoidal source voltage waveforms also [41]. With $(X_L/R_\ell) = 1.0$ and $(X_L/X_C) = 0.2$, the bridge-input voltage value at $\Theta = 0$ is determined as 1.519 times the peak value of source voltage.

The capacitor current waveform for case (A) is shown in Figure 20. The duration of capacitor current increases with an increase in the decoupled duration (γ/ω). When the decoupled duration (γ/ω) becomes equal to $(\pi/3)$, only two of the three bridges conduct through the load at any one time.

The influence of bridge-input capacitors on the source current can be seen in the phase current (i_a) waveform. The provision of an additional path through the capacitor for current flow contributes to the

formation of an additional crest (during $0 \leq \Theta \leq \gamma$) in the phase current waveform.

The load current i_ℓ effectively remains constant during the decoupled duration of any phase. Therefore, the bridge-input capacitor current in the conducting phases during this duration is negligibly small. At $\Theta = \gamma$, diode pair 1 starts to conduct. At this instant there is an instantaneous transfer of current from the capacitor to the load. This jump in the bridge-input current $i_{a\ell}$ and load current i_ℓ at $\Theta = \gamma$ is evident in Figures 20 and 19 respectively for phase-a.

For case (A), with $(X_L/R_\ell) = 2.2$ and $(X_L/X_C) = 0.09$, the angles β and γ are determined as 33.4° and 26.4° respectively. The bridge-input voltage v_a waveform is the same as the load current v_ℓ waveform as long as the bridge conducts. The phase current i_a continues to increase until the source voltage is equal to the bridge input voltage.

For case (B), with $(X_L/R_\ell) = 3.0$ and $(X_L/X_C) = 0.14$, the angles β and γ are determined as 45.5° and 30.6°. The general character of i_a, i_ℓ and v_a waveforms is similar to the corresponding waveforms in case (A). The peak amplitude of the capacitor current in this case is higher than in case (A) due to a higher value of γ. The initial value of the load current at $\Theta = 0$ and the amplitude of the load current in this case are smaller than in case (A).

CHAPTER IV

WAVEFORM EFFECTS ON THE OPERATION OF THE FIELD MODULATED GENERATOR SYSTEM AND DEVELOPMENT OF DESIGN GUIDELINES

4.1 Introduction

This chapter deals with the task of studying the waveform effects on the operation of the field modulated generator system, leading to the development of some basic design guidelines. The parallel-bridge rectifier system with bridge-input capacitors and resistive loads has been analyzed in Chapter III for trapezoidal source voltage waveforms. The results of this analysis are employed to derive a relationship between the average (dc) value of the load voltage (normalized with respect to the maximum value of the source voltage per phase) and the various circuit parameter ratios. Appropriate modulation factors are used to extend the results to the field modulated (ac excitation) case. Finally, some design guidelines of practical significance are developed for the FMGS in terms of its output specifications on the assumption that the machine is operating with non-sinusoidal waveforms of the type discussed. The general design approach is illustrated with an example.

Section 4.2 presents the analysis leading to the relationship between the normalized average (dc) load voltage and the different circuit parameter ratios under dc excitation.

Section 4.3 details the assumptions and the procedure involved in

the extension of the parallel-bridge rectifier system studies made under dc excitation to the field modulated case (ac excitation).

Section 4.4 deals with the development of some basic design guidelines of practical importance. They are based on the relationship between the load voltage, induced voltage in the stator windings and circuit parameter values for given output specifications. A numerical example is used to illustrate the design procedure.

4.2 Relationship Between V_d and E With dc Excitation

Expressions for various currents and voltages have been obtained in Chapter III for the parallel-bridge rectifier system with bridge-input capacitors and resistive loads for trapezoidal source voltage waveforms. It can be seen in Figures 19 and 22 that the load current waveform (which is the same as the load voltage waveform for resistive loads) is essentially dc. The average value of the load voltage can be determined from the output voltage waveform.

In the system shown in Figure 11, the output of the three stator-phases of a high-frequency alternator is processed using a parallel-bridge rectifier system with bridge-input capacitors to obtain a dc output. A relationship between the average load voltage, peak value of the source voltage (which is the same as the peak value of the induced voltage in the alternator windings per phase) and different circuit parameter ratios is essential to develop design guidelines for the FMGS. In this section such a relationship is derived.

Since the load current is periodic with a period of $(\pi/3)$, it is sufficient to compute the average voltage across the load over the interval $t = 0$ to $t = (\pi/3\omega)$. This duration is divided into three segments

and the expression for the load current during each segment is obtained from the analysis of Chapter III for different cases.

Case (A): $0 < (\gamma + \beta) \leq (\pi/3)$

The voltage across the load for this case during the time interval $0 \leq t_1 < (\gamma/\omega)^-$ is given by (see Equation (3.3.10))

$$v_{\ell 1}(t_1) = I(0)_\ell R_\ell \, e^{-2R_\ell t_1/L} + \left(\frac{E}{1} - \frac{E\beta}{2\theta_1} + \frac{E\omega L}{4\theta_1 R_\ell}\right)\left(1 - e^{-2R_\ell t_1/L}\right) - \frac{E\omega t_1}{2\theta_1} \tag{4.2.1}$$

The voltage across the load during the time interval $0 \leq t_2 \leq (\pi/3 - \beta - \gamma)/\omega$ is given by (see Equation (3.3.18))

$$v_{\ell 2}(t_2) = I_{\ell 1} \, R_\ell \, e^{-3R_\ell t_2/L} + \frac{2E}{3}\left(1 - e^{-3R_\ell t_2/L}\right) \tag{4.2.2}$$

The voltage across the load during the time interval $0 \leq t_3 \leq (\beta/\omega)$ is given by (see Equation (3.3.24))

$$v_{\ell 3}(t_3) = I_{\ell 2} \, R_\ell \, e^{-3R_\ell t_3/L} + \left(\frac{2E}{3} + \frac{2E\omega L}{9R_\ell \theta_1}\right)\left(1 - e^{-3R_\ell t_3/L}\right) - \frac{2E\omega t_3}{3\theta_1} \tag{4.2.3}$$

The expressions for $I(0)_\ell$, $I_{\ell 1}$ and $I_{\ell 2}$ are given by Equations (3.3.26), (3.3.13) and (3.3.19), respectively. The area under the load voltage curve from $\theta = 0$ to $\pi/3$ is obtained by integrating the three expressions given above between proper time limits and adding the results. The average (dc) value of the load voltage can then be obtained by dividing the area under the load voltage curve from 0 to $(\pi/3)$ by the

time duration ($\pi/3\omega$). The expression for the average load voltage V_d for Case (A) is given below.

$$V_d = \frac{3}{\pi}\Bigg\{\frac{I(0)\ell\,\omega L}{2}\left(1 - e^{-2R_\ell\gamma/\omega L}\right) + \left(\frac{E}{1} - \frac{E\beta}{2\theta_1} + \frac{E\omega L}{4\theta_1 R_\ell}\right)\left[\frac{\gamma}{1} + \frac{\omega L}{2R_\ell}\left(e^{-2R_\ell\gamma/\omega L} - 1\right)\right] - \frac{E\gamma^2}{4\theta_1} + \frac{I_{\ell 1}\,\omega L}{3}\left(1 - e^{-3R_\ell(\pi/3 - \beta - \gamma)/\omega L}\right) + \frac{2E}{3}\left[\left(\frac{\pi}{3} - \beta - \gamma\right) + \frac{\omega L}{3R_\ell}\left(e^{-3R_\ell/\omega L(\pi/3 - \beta - \gamma)} - 1\right)\right] + \frac{I_{\ell 2}\,\omega L}{3}\left(1 - e^{-3R_\ell\beta/\omega L}\right) + \left(\frac{2E}{3} + \frac{2E\omega L}{9R_\ell\theta_1}\right)\left[\beta + \frac{\omega L}{3R_\ell}\left(e^{-3R_\ell\beta/\omega L} - 1\right)\right] - \frac{E\beta^2}{3\theta_1}\Bigg\} \tag{4.2.4}$$

Case (B): $(\pi/3) \le (\gamma + \beta) \le (2\pi/3)$

The approach to determine the average voltage across the load in this case is very similar to the one used for Case (A). The expression for the average voltage across the load V_d in this case is:

$$V_d = \frac{3}{\pi}\Bigg\{\frac{I(0)\ell\,\omega L}{2}\left(1 - e^{-2R_\ell/\omega L(\pi/3 - \beta)}\right) - \frac{E(\pi/3 - \beta)^2}{4\theta_1} + \left(\frac{E}{1} - \frac{E\beta}{2\theta_1} + \frac{E\omega L}{4\theta_1 R_\ell}\right)\left[\frac{\pi}{3} - \beta + \frac{\omega L}{2R_\ell}\left(e^{-2R_\ell/\omega L(\pi/3 - \beta)} - 1\right)\right] + \frac{I_{\ell 1}\,\omega L}{2}\left(1 - e^{-2R_\ell/\omega L(\gamma + \beta - \pi/3)}\right) - \frac{E(\gamma + \beta - \pi/3)^2}{2\theta_1} + \left(\frac{E}{2} + \frac{E\omega L}{2\theta_1 R_\ell}\right)\left[(\gamma + \beta - \frac{\pi}{3}) + \frac{\omega L}{2R_\ell}\left(e^{-2R_\ell/\omega L(\gamma + \beta - \pi/3)} - 1\right)\right]$$

$$+ \frac{I_{\ell 2}\,\omega L}{3}\left(1 - e^{-3R_\ell/\omega L(\pi/3 - \gamma)}\right) - \frac{E(\pi/3 - \gamma)^2}{3\theta_1}$$

$$+ \left(\frac{4E}{3} - \frac{2E(\gamma + \beta)}{3\theta_1} + \frac{2E\omega L}{9R_\ell\theta_1}\right)\left[\left(\frac{\pi}{3} - \gamma\right)\right.$$

$$\left. + \frac{\omega L}{3R_\ell}\left(e^{-3R_\ell/\omega L(\pi/3 - \gamma)} - 1\right)\right] \Bigg\} \qquad (4.2.5)$$

After substituting for $I(0)_\ell$, $I_{\ell 1}$ and $I_{\ell 2}$, the respective expressions for the corresponding cases in Equations (4.2.4) and (4.2.5), an expression for the average (dc) value of the load voltage (normalized with respect to the maximum value of the induced voltage in the stator windings) in terms of circuit parameter ratios (X_L/R_ℓ), (X_L/X_C) and angles γ and β can be obtained. The values for angles γ and β are determined from Figure 18 for chosen values of (X_L/R_ℓ) and (X_L/X_C). The ratio (V_d/E) is evaluated in both cases for different values of parameter ratios.

Figure 23 shows the ratio (V_d/E) plotted against (X_L/R_ℓ) for different values of (X_L/X_C). It can be observed from the plots that for a given value of (X_L/X_C), as (X_L/R_ℓ) increases, the ratio (V_d/E) decreases. The plots tend to converge as (X_L/R_ℓ) increases, indicating less and less dependence on (X_L/X_C) under heavy load conditions (small R_ℓ). For the range of $(\gamma + \beta)$ given by $0 < (\gamma + \beta) \leq \pi/3$ which corresponds to Case (A), the dependence of (V_d/E) on (X_L/R_ℓ) for a given (X_L/X_C) is almost linear. For the range of $(\gamma + \beta)$ given by $\pi/3 \leq (\gamma + \beta) \leq (2\pi/3)$ corresponding to Case (B), the dependence of (V_d/E) on (X_L/R_ℓ) for a given (X_L/X_C) is nonlinear. The ratio (V_d/E) is not determined for values of $(X_L/R_\ell) < 0.9$ and $(X_L/X_C) > 0.14$, since angle β becomes negative for these parameter ratios. Figure 23 gives a direct relationship

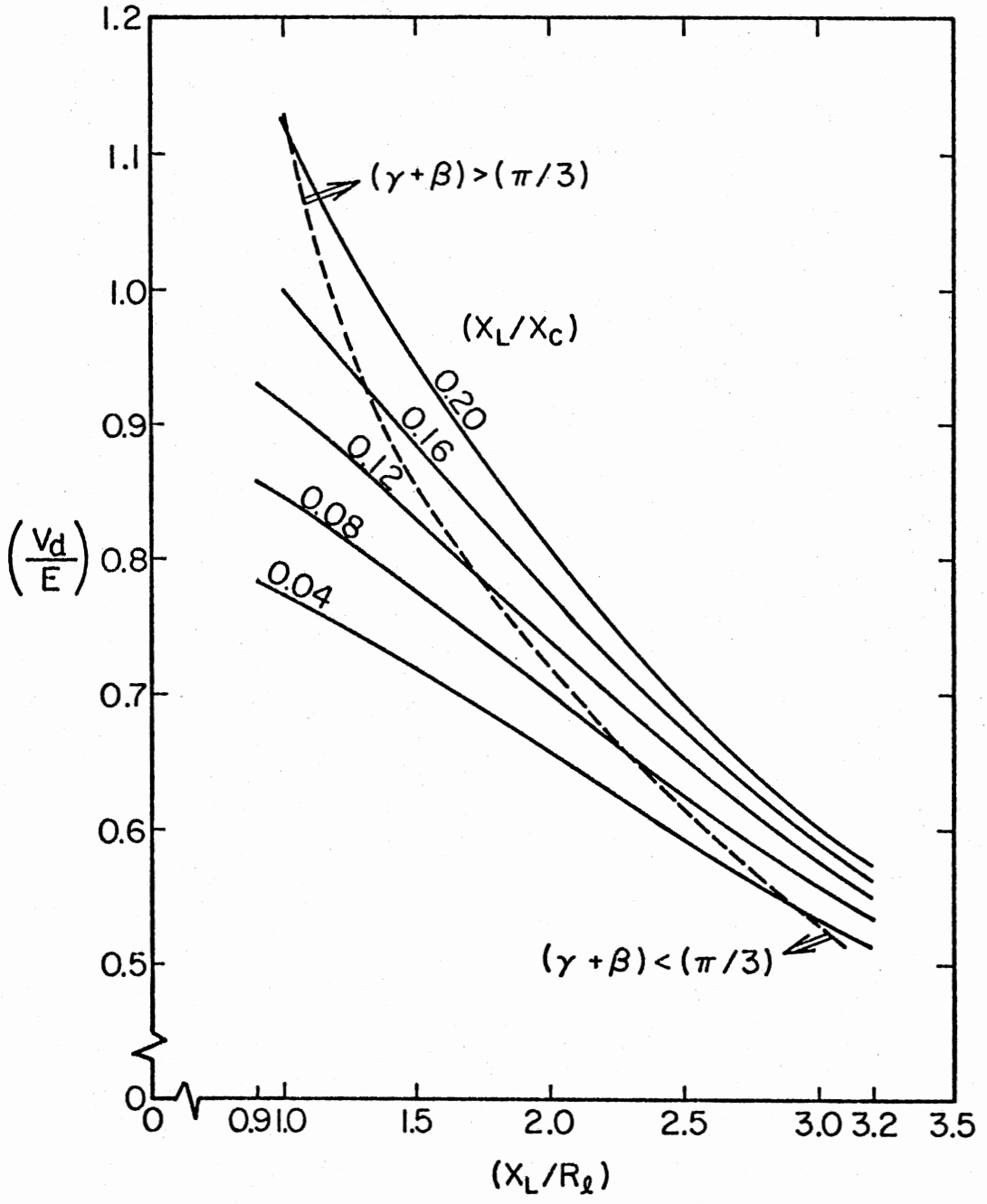

Figure 23. Theoretical Values of (V_d/E)

between the average load voltage and the maximum induced voltage per phase in the stator winding for different circuit parameter values.

4.3 Extension of PBRS Studies to the Field Modulated Case

Field modulation techniques use an electromagnetic modulator in the form of exciting the rotating field coil of an alternator with alternating current at the required low frequency to obtain a variety of desired output. When a conventional three-phase synchronous machine of basic frequency f is excited with a sinusoidal alternating current of frequency f_m, $f > f_m$, induced voltages in the stator of frequencies $(f + f_m)$ and $(f - f_m)$ result. When such three-phase voltages are individually fullwave rectified and their output tied in parallel, an output voltage across the PBRS containing a fullwave rectified ac corresponding to the frequency f_m along with a ripple of frequency six times the basic machine frequency results. The ripple in the output voltage across the PBRS will be small for values of (f/f_m) greater than ten. In addition, flat topped induced voltage waveforms in the stator windings also contribute to ripple reduction. The ripple can be filtered out of the FMGS output using a low-pass filter.

The waveforms and the results obtained in Chapters II and III are valid for an alternator-PBRS combination under dc excitation. Based on these, the field modulated generator system waveforms under resistive loads and sinusoidal ac excitation (field modulation) can be approximated by using proper modulation factors. In this section the assumptions and the procedure involved in the extension of PBRS studies to the field modulated case are discussed.

The following assumptions are made in considering the field modulation effects.

1. The modulation frequency is much smaller (less than ten percent) than the basic rotational frequency of the machine throughout the operating speed range.

2. Transformer voltages are neglected as small in comparison with the speed voltages in the stator windings.

3. The maximum values of bridge-input voltage and load voltage occur at the same instant of time.

4. Stator and rotor winding resistances are negligibly small.

5. Saturation effects are neglected.

6. Ideal filtering conditions are assumed at the output of the PBRS.

In the expressions derived in Chapters II and III with dc excitation, the alternator electrical angular frequency ω corresponding to the basic rotational machine frequency was used in determining reactances and associated angles. When the field is (modulated) excited with an alternating current of frequency f_m, all electrical angles at the machine frequency will be scaled down by the factor "m" when viewed from the (rotor) low-frequency side. The factor "m," called the modulation frequency ratio, is the ratio of the basic machine frequency to the field modulation frequency.

Let the sinusoidal voltage applied to the excitation coil of an alternator at the modulation angular frequency ω_m be

$$v_f = -V_f \sin \omega_m t \tag{4.3.1}$$

Assuming the excitation coil to be purely inductive, the excitation current will then be given by

$$i_f = I_f \cos \omega_m t \qquad (4.3.2)$$

in which V_f and I_f are the peak values of the excitation voltage and current, respectively. In any rotating electrical machine, under loaded conditions, the resultant flux distribution in the air-gap is set up by the interaction of the field magneto-motive-force (MMF) and the armature MMF. The voltages induced in the stator windings are due to this resultant flux distribution in the air-gap. As discussed earlier, in the case of the FMGS with the special magnetic circuit, the resultant field-form under full-load conditions with bridge-input capacitors and resistive loads with dc excitation is very close to a symmetric trapezoid with top width equal to one-third of the half-period. Therefore, with field modulation, the voltages induced in the stator windings will be sinusoidally-modulated trapezoidal waveforms of the type shown in Figure 24(a). It can be seen that, with dc excitation, the modulation frequency is zero and therefore the amplitude of the trapezoidal waveform remains constant, as shown in Figure 24(b). Neglecting transformer voltages, the instantaneous value of the induced voltage in each phase with field-modulation under full load conditions can be obtained by using the modulation factor $\cos \omega_m t$. If e_a, e_b and e_c represent the instantaneous values of the induced voltages in the three stator phases a, b and c, respectively, under full load conditions with dc excitation, then the expressions for the instantaneous values of the induced voltages (e_{am}, e_{bm} and e_{cm}) with field-modulation in the three stator windings will take the form given below:

$$e_{am} = e_a \cos \omega_m t \qquad (4.3.3)$$

$$e_{bm} = e_b \cos \omega_m t \qquad (4.3.4)$$

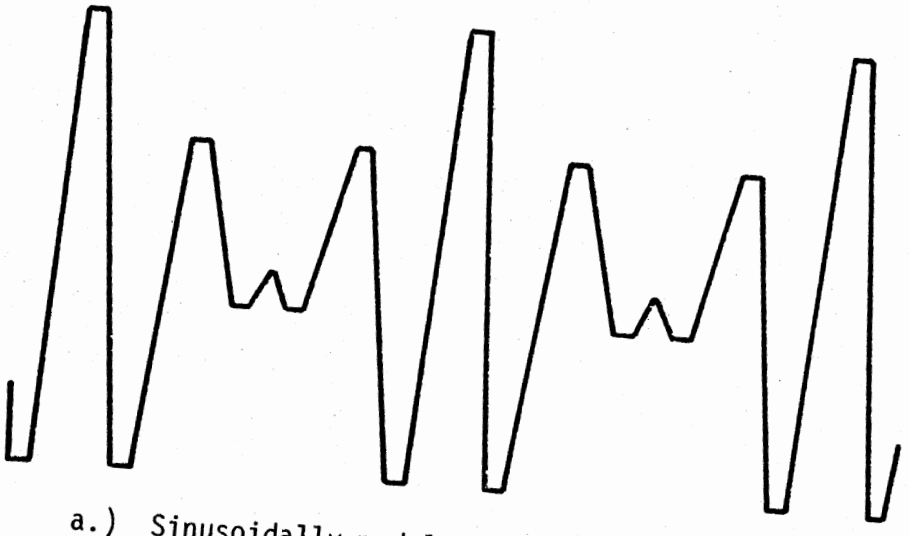

a.) Sinusoidally-modulated trapezoidal waveform

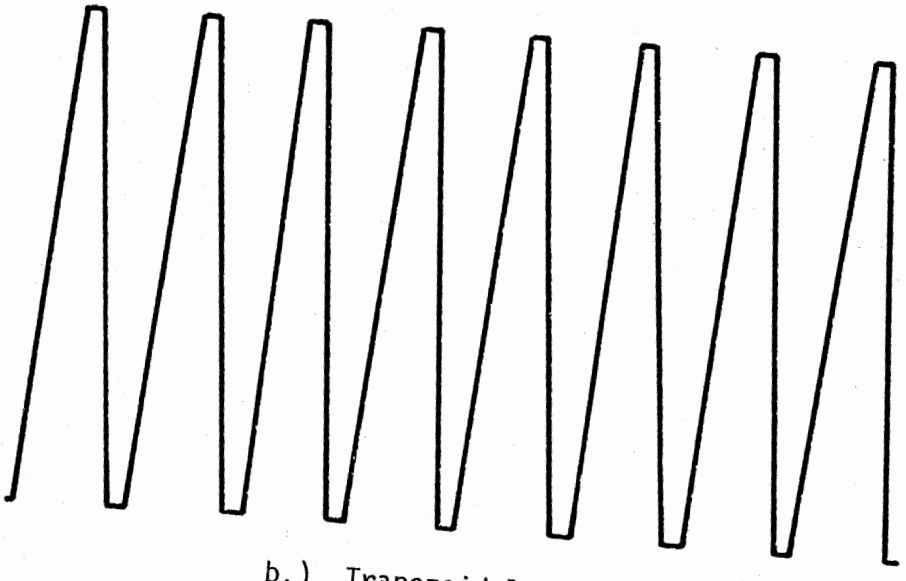

b.) Trapezoidal waveform

Figure 24. Modulated and Un-modulated Trapezoidal Waveforms

$$e_{cm} = e_c \cos \omega_m t \qquad (4.3.5)$$

The expressions for the currents in the three phases can be determined from the PBRS analysis by considering the induced voltages as given above as the source voltages. In essence, the effect of modulation can be considered as the equivalent of a slowly-varying dc.

4.4 Design Guidelines

The starting point in the design of any electrical machine is the output specifications which the machine must meet. The field modulated generator system is a variable speed adjustable frequency electrical power system. Depending on the type of electrical output desired at the application end, the specifications for the FMGS vary. If the electrical output desired at the application end is constant-voltage constant-frequency utility grade ac for direct insertion into an existing grid (without an intermediate energy storage and reconversion system), then the output voltage and frequency of the FMGS are fixed corresponding to normal utility grade ac specifications. If direct coupling of the field modulated generator to prime-movers operating in the variable-speed mode is required, then the power rating should be specified over the entire operating speed range.

In general, the rating of an electrical machine will vary almost nearly linearly with the rotor speed. Since the field modulated generator system operates with rotor speeds varying over a range of values, the output specifications must be met at both ends of the speed range. The requirement that the modulation frequency ratio "m" be at least 10, therefore, must be satisfied at the lowest speed of operation. The choice of the number of poles is thus determined by "m" and the lowest

speed of operation. The field modulated generator must be designed such that the output voltage and the output power specifications are met at the lowest speed. This means the number of turns per phase in the stator winding and the main dimensions of the machine are determined based on the lowest speed. However, the cross sectional area of the conductors in the stator windings, the winding insulation, and the peripheral speed limitations need to be determined by the rating corresponding to the highest speed of operation. In effect, the design must satisfy the output specifications at the lowest speed and should be able to deliver the higher output at the highest operating speed. In other words, the amount of iron and rotor copper in the machine are determined by the lowest speed of operation and the amount of stator copper is determined by the highest speed of operation. Therefore, at no speed will the iron and copper be subject to full utilization. Any electrical apparatus designed to operate over a range of speeds will have this drawback. As such, compromises are necessary in designing the magnetic and the electrical circuits in the machine.

Since the circuit parameter ratios depend on the speed of operation of the machine, the angles α and β which determine the conduction duration of the diodes and the time differences between the zero crossovers of source voltages and currents and the angle γ which determines the decoupled duration of a bridge vary with the speed of operation of the FMGS.

The overall physical size of a field-modulated generator will be a little larger than a conventional alternator operating at the same speed and output specifications. The reason for this is the field modulation and the resulting inefficient utilization of the magnetic circuit as can

be understood by referring to Figure 24 in which a sinusoidally modulated trapezoidal wave and a regular trapezoidal wave are shown. Assuming the waveforms represent the flux distribution in the air-gap under full load conditions for the field modulated and dc excitation cases, it can be observed that the average value of the flux density in the air-gap with modulated wave is less when compared with the regular trapezoidal wave. Since the peak flux density in a machine is fixed by the magnetic circuit characteristics, it is obvious that the magnetic circuit utilization is not as good with field modulation as it is with dc excitation. In order to compensate for the lower value of the average flux density in the air-gap with field-modulation, the physical size of the machine should be increased appropriately.

With modulated current waveforms, the root-mean-square (rms) value of the current is lower than the rms value of the current for the unmodulated current wave. Therefore, with the same maximum peak current density and conductor size, the copper losses in the stator are less with field modulation. Thus the effect of poor magnetic circuit utilization is partly compensated by the fact that higher peak currents and correspondingly higher output can be allowed without exceeding the limit on the stator copper losses. Rotor iron losses in the field modulated generator (FMG) will be slightly higher due to ac excitation. These facts, coupled with the employment of proper stator and rotor tuning capacitors, result in high efficiencies for the FMGS without substantial penalties in size.

The procedure for the determination of the main dimensions of the field modulated generator is very similar to that of a conventional three-phase synchronous machine. However, the effect of field modulation

must be carefully incorporated. In the following paragraphs a brief description of the design procedure is given.

4.4.1 Main Dimensions

The output coefficient of a rotating electrical machine is proportional to the volt-ampere output per unit volume of the stator bore per revolution. It can be evaluated by choosing proper values for the specific magnetic loading, specific electric loading, form factor for the air-gap flux distribution, and the winding factor for the stator winding. The D^2L_C product for the machine can be evaluated once the output coefficient is determined. As discussed earlier, the magnetic circuit utilization is poor with field modulation. The D^2L_C product obtained is based on the specific magnetic loading, which is simply the average value of the flux density in the air-gap. Since the peak flux density in a machine is tied to the magnetic circuit characteristics, the FMG must be designed to operate at the same values of peak flux density as a conventional machine. With reference to the specific electric loading, the presence of modulated current waveforms will result in a reduction of conductor cross sectional area in the stator or an increase in the output power capability without exceeding the limit on stator copper losses.

One approach to incorporate the sinusoidal field modulation effect on the magnetic circuit and on the D^2L_C product is to increase the value obtained by the conventional approach by the ratio (peak value/average value) corresponding to a sinusoidal waveform. To include the difference in the rms values of unmodulated and modulated stator currents, an additional factor is warranted. This factor will obviously be between 1 and $(1/\sqrt{2})$, the latter being the ratio of the rms values of the

unmodulated and modulated waveforms having the same maximum peak value. Thus, these two effects considered together yield a factor which is between $(\pi/2)$ and $(\pi/2\sqrt{2})$ or between 1.57 and 1.11. The realistic value will be closer to 1.11, especially because of the transfer of some of the rotor copper losses to the stator by the use of stator tuning capacitors. Based on this discussion, it is suggested to use a value in the range of 1.15 to 1.2 in the preliminary design calculations.

After choosing a value for the modulation frequency ratio "m" greater than ten, the basic rotational frequency for the FMG is obtained. The number of poles in the machine is determined from the lowest speed of operation and the minimum basic rotational frequency required. For high-speed machines, a nearly square pole with pole pitch equal to 90 percent of the core length gives good electrical design [42].

The use of PBRS eliminates line-to-line short circuits and tends to present a balanced load to three-phase power sources with high commutating reactances. In order to take advantage of this characteristic, the FMG is designed in such a way as to increase the commutating reactance, which is very nearly equal to the leakage reactance. Provision of deep slots and larger winding overhangs in the stator are some of the design features that can lead to the required goal.

From the improved D^2L_C product (to include field modulation effect), the expression for pole pitch and the number of poles required, the diameter of the stator bore and core length can be determined. The flux per pole based on specific magnetic loading and pole area, the length of the air-gap and the peripheral speed of the rotor are determined next. For high speed machines with rotating windings, the peripheral speed of the rotor should not exceed 150 meters per second.

4.4.2 Induced Voltage and Turns Per Phase

The commutating inductance L of a properly designed field modulated generator is expected to be slightly larger than that of an alternator having the same physical size and output power. However, due to the high basic machine frequency, the commutating reactance is large in the case of field modulated generators. In order to pick an initial value for the commutating inductance L for the FMG, the normal value of the commutating inductance per phase for a conventional alternator of the same physical size and power output can be chosen. The load resistance under full-load conditions can be calculated from the machine rating and the output voltage, assuming the load to be purely resistive.

In general, the use of capacitors at the bridge-input terminals improves the regulation. However, with too large a value of capacitance, under light loads (large load resistance), resonance conditions may occur, leading to overvoltages. Therefore, the initial value of the bridge-input capacitance C should be chosen judiciously. It has been observed in practice that, for satisfactory operation of the FMGS, the normal range with most of the practical machines, for the ratio (X_L/X_C) is 0.02 to 0.2.

Once the values of L and C are chosen and the value of R_ℓ is determined, the parameter ratios (X_L/R_ℓ) and (X_L/X_C) corresponding to an average basic machine angular frequency can be calculated. The peak value of the output voltage can be determined from the output voltage specification.

In order to get a relationship between the peak value of the output voltage and the corresponding maximum peak value of the induced voltage per phase required in the stator winding, the effect of modulation

can be considered as equivalent to a slowly-varying dc. A relationship between circuit parameter ratios (X_L/R_ℓ), (X_L/X_C) and the ratio of average (dc) value of the load voltage V_d to the maximum value of the induced voltage per phase E has already been obtained in section 4.2 for dc excitation. Therefore, to obtain the maximum peak induced voltage per phase required in the stator for a given peak output voltage and circuit parameter ratios, the peak output voltage is correlated with the average (dc) value of the load voltage V_d discussed earlier for dc excitation.

With the parameter ratios (X_L/R_ℓ) and (X_L/X_C) known, the ratio (V_d/E) is determined from Figure 23. Associating the peak output voltage to the average (dc) voltage V_d, the maximum peak value of the induced voltage per phase required under full load conditions can be determined. The number of turns per phase required in the stator can now be calculated using the voltage induced per turn.

The design procedure to be followed after obtaining the main dimensions and the number of turns per phase in the stator is well established for alternators. A similar design procedure can be followed to complete the rest of the field modulated generator design.

4.4.3 Design Procedure

The basic design procedure discussed in sections 4.4.1 and 4.4.2 for the FMGS is formulated in the form of equations in the following paragraphs.

Specifications:

f_m = modulating frequency, Hz;

N = minimum speed of operation, r/min;

P_o = power output, kW;

V_{rms} = rms value of output voltage, V;

Nomenclature:

B = specific magnetic loading, Wb/m^2;

C = stator tuning (bridge-input) capacitance per phase, F;

D = stator bore diameter, m;

E = maximum peak induced voltage/phase in stator, V;

E_{ph} = induced rms voltage/phase, V;

f = basic machine frequency, Hz;

G = output coefficient, $KW\text{-}second/m^3$;

I_p = phase current (rms), A;

K_f = form factor;

K_{ff} = filter factor;

K_v = ratio of V_d to E read from Figure 23;

K_w = winding factor;

L = stator commutating inductance per phase; H;

L_C = stator core length, m;

ℓ_g = radial air-gap length, m;

m = modulation frequency ratio (f/f_m);

n = minimum rotor speed, r/s;

2p = total number of poles;

q = specific electric loading, ampere-conductors/m;

R_ℓ = load resistance, Ω;

T = turns per phase in stator;

u = rotor peripheral speed, meters per second;

V_d = average (dc) load voltage for PBRS model, V;

V_p = peak value of output voltage, V;

X_C = capacitive reactance of bridge-input capacitor, Ω;

X_L = commutating reactance of stator per phase, Ω;

Y = pole pitch ($\pi D/2p$), m;

ϕ = magnetic flux per pole, Wb;

ω_a = average machine electrical angular frequency, rad/s.

4.4.3.1 Main Dimensions. The D^2L_C product is obtained first by the procedures of conventional three-phase machine design. Then the modulation effect is incorporated and an improved value is determined for the field modulated generator. Assuming a trapezoidal flux distribution in the air-gap as shown in Figure 25, the rms value of the induced voltage in the stator phase is given by

$$E_{ph} = 4\ K_f\ K_w\ \phi\ f\ T \tag{4.4.1}$$

The form factor for any periodic waveform is

$$K_f = (\text{rms value/average value}) \tag{4.4.2}$$

The form factor for the trapezoidal wave shown in Figure 25 is obtained as 1.12. The output of all three phases, each carrying an rms current of I_p amperes with resistive loads, is given by

$$P_o = 3\ E_{ph}\ I_p\ 10^{-3} \tag{4.4.3}$$

Substituting for E_{ph} from Equation (4.4.1) in Equation (4.4.3) and writing

$$\phi = B\ \pi D L_C/2p \tag{4.4.4}$$

$$I_p T = q\ \pi D/6 \tag{4.4.5}$$

The output of a three-phase machine can be written as

$$P_o = 9.87\ K_f\ K_w\ B\ q\ D^2L_C\ n\ 10^{-3} \tag{4.4.6}$$

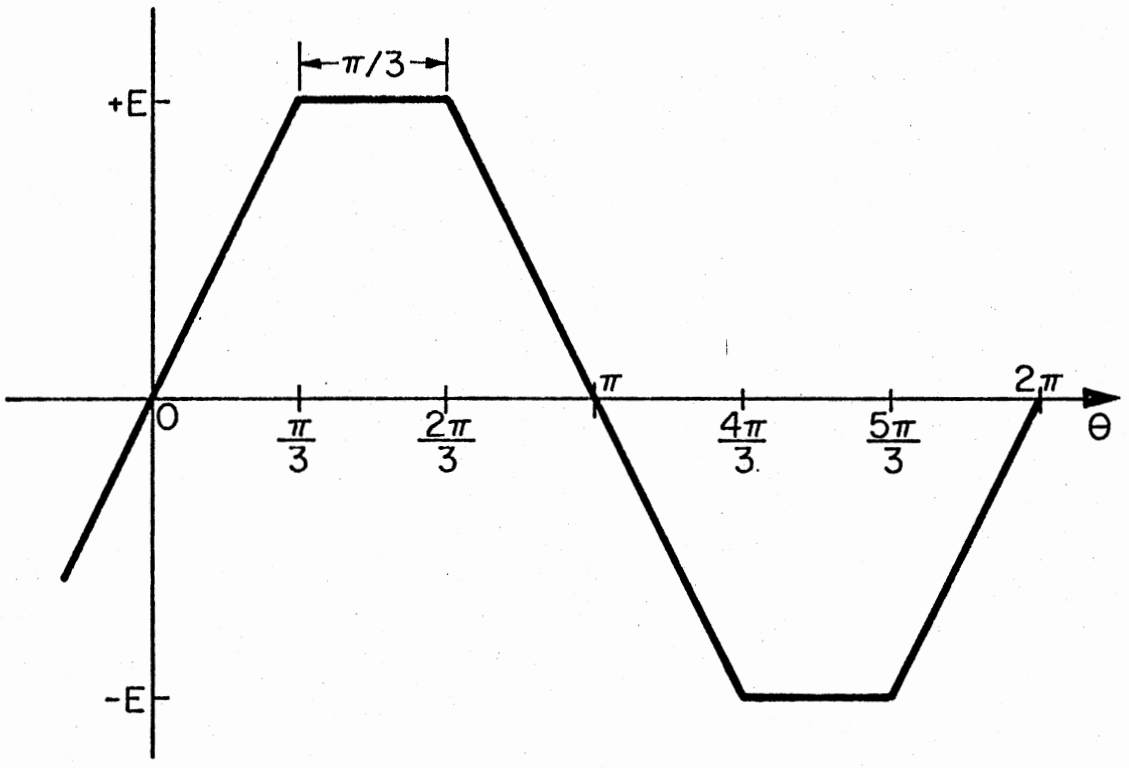

Figure 25. Idealized Field Form Under Full Load

The output coefficient G is defined as

$$G = P_o/D^2L_C\ n \tag{4.4.7}$$

The output coefficient can be expressed in terms of specific loadings, K_f and K_w, as follows:

$$G = 9.87\ K_f\ K_w\ B\ q\ 10^{-3} \tag{4.4.8}$$

Normally the value of B varies between 0.4 and 0.5 Wb/m^2 and q varies between 15000 and 45000 ampere-conductors/m [43]. For uniformly distributed windings with full-pitch coils and three slots per pole per phase, the winding factor is 0.955. Choosing proper values for B and q within the ranges mentioned, the output coefficient and the D^2L_C product can be determined for a given output rating of the machine.

To include the field modulation effect, the D^2L_C product is increased by a factor 1.2 as discussed earlier. Therefore, the improved D^2L_C product is given by

$$D^2L_C = 1.2\ P_o/G\ n \tag{4.4.9}$$

The requirement that the modulation frequency ratio "m" be greater than ten for satisfactory operation of FMGS fixes the basic machine frequency f and is given by

$$f = m\ f_m \tag{4.4.10}$$

Based on the basic machine frequency and the lowest rotor speed, the number of poles for the machine is given by

$$2p = 2f/n \tag{4.4.11}$$

Choosing roughly square poles, the core length L_C is determined as

$$L_C = 1.1\ \pi D/2p \tag{4.4.12}$$

Substituting for L_C in Equation (4.4.9) from Equation (4.4.12) the values for D and L_C can be determined.

The pole pitch Y is given by

$$Y = (\pi D/2p) \tag{4.4.13}$$

The flux per pole ϕ in the modulated case should correspond to the peak excitation current and can be determined from the following expression.

$$\phi = B\ Y\ L_C \tag{4.4.14}$$

The air-gap length for small machines is given by

$$\ell_g = [0.14 + 2\sqrt{D\ L_C}]\ 10^{-3} \tag{4.4.15}$$

The rotor diameter is $(D - 2\ell_g)$ and the peripheral speed of the rotor is given by

$$u = \pi(D - 2\ell_g)\ n \tag{4.4.16}$$

Typically, the peripheral speed should not exceed a value of 150 meters per second.

4.4.3.2 Stator Induced Voltage and Turns Per Phase. A field modulated generator system takes the three-phase high-frequency electrical output of a machine and provides single-phase power output at the required low frequency. Thus the load resistance under full-load conditions can be determined from the output power and voltage and is given by

$$R_\ell = (V^2_{rms}/P_o) \tag{4.4.17}$$

After choosing the values of L and C and determining the average basic

machine angular frequency ω_a, the inductive and capacitive reactances can be determined.

$$X_L = \omega_a L \tag{4.4.18}$$

$$X_C = 1/\omega_a C \tag{4.4.19}$$

For sinusoidal output voltage, the peak value of the output voltage is obtained as

$$V_p = \sqrt{2}\, V_{rms} \tag{4.4.20}$$

For chosen parameter ratios (X_L/R_ℓ) and (X_L/X_C), the ratio (V_d/E) is obtained from Figure 23 and is defined as

$$K_v = (V_d/E) \tag{4.4.21}$$

With the peak output voltage correlated with the average (dc) value of the load voltage under dc excitation, the relationship between V_d and V_p is given by

$$V_p = V_d\, K_{ff} \tag{4.4.22}$$

Substituting for V_d in Equation (4.4.21) from Equation (4.4.22), the expression for the maximum peak value of the induced voltage per phase under full load conditions is given by

$$E = (V_p/K_{ff}\, K_v) \tag{4.4.23}$$

The maximum peak value of the induced voltage in each phase under full load conditions corresponds to maximum excitation current in the field coil with field modulation. Since the flux per pole ϕ with field modulation corresponds to the peak excitation current in the rotor field coil, the number of turns in series per phase required in the stator, in terms

of the flux per pole, basic machine frequency, form factor, and winding factor for a maximum peak induced voltage E in the stator is given by

$$T = (E/4\ K_f\ K_w\ \phi\ f) \qquad (4.4.24)$$

4.4.4 Example

Determination of the main dimensions and stator turns per phase for a field-modulated generator rated at 10 kW and operating at a minimum speed of 7000 r/min (with 12 kW at maximum speed of 8500 r/min), single phase, 220V, with output at a frequency of 60 Hz.

4.4.4.1 Main Dimensions. Choosing

$K_f = 1.12$

$K_w = 0.955$

$B = 0.43\ Wb/m^2$

$q = 20000$ ampere-conductors/m

the output coefficient G from Equation (4.4.8) is obtained as

$$G = 90.789\ kW\text{-}sec/m^3$$

The D^2L_C product from Equation (4.4.9) is obtained as

$$D^2L_C = (1.1329)\ 10^{-3}\ m^3$$

Choosing a value of m between 15 and 16, the basic machine frequency f from Equation (4.4.10) is obtained as

$$f = 930\ Hz$$

The number of poles for the field-modulated generator is obtained using Equation (4.4.11).

$2p = 16$

Making the core length L_C equal to 1.1 times the pole pitch, the values (rounded off) for the diameter and core length of the stator bore are

$D = 0.17$ m

$L_C = 0.04$ m

The pole pitch, the flux per pole corresponding to peak excitation current, the length of the air-gap, and rotor peripheral speed (for the maximum operating speed) are obtained next.

$Y = 0.03338$ m

$\phi = 0.5741$ m Wb

$\ell_g = 3 \times 10^{-4}$ m

$u = 75$ meters per second

4.4.4.2 Stator Induced Voltage and Turns Per Phase.

$V_{rms} = 220$ volts

$V_p = 220\sqrt{2}$ volts

The load resistance using Equation (4.4.17) is obtained as

$R_\ell = 4.84$ ohms

Choosing L = 0.69 mH and C = 5μF, the circuit parameter ratio values are

$X_L/R_\ell = 0.925$

$X_L/X_C = 0.14$

From Figure 23 the ratio (V_d/E) is obtained as 0.945 for the chosen parameter ratios. Therefore,

$$K_v = 0.945$$

Assuming $K_{ff} = 1$ corresponding to ideal filtering, the maximum peak value of the induced voltage per phase in stator using Equation (4.4.23) is obtained as

$$E = 330 \text{ volts}$$

The number of turns per phase using Equation (4.4.24) is obtained as

$$T = 145$$

The main dimensions obtained and the number of turns per phase determined for the 10 kW, 220 V, 60 Hz, 7000 r/min field-modulated generator are in close agreement with the corresponding values for the experimental prototype FMGS built for the same rating at Oklahoma State University.

Figure 26 shows (not to scale) the rotor and stator laminations for the 10 kW prototype. A flat topped field form is obtained by designing a uniformly slotted round rotor with a winding arrangement that resulted in magnetic neutral planes in the centers of teeth rather than in the centers of slots. The no-load field form which represents a rectangular pulse as a consequence of the magnetic circuit design of the machine is shown in Figure 26. Unlike conventional alternators, the stator and rotor slots in the field-modulated generator are made deep to increase the commutating reactance, so that the advantages of PBRS operation in conjunction with high reactance machines can be fully realized.

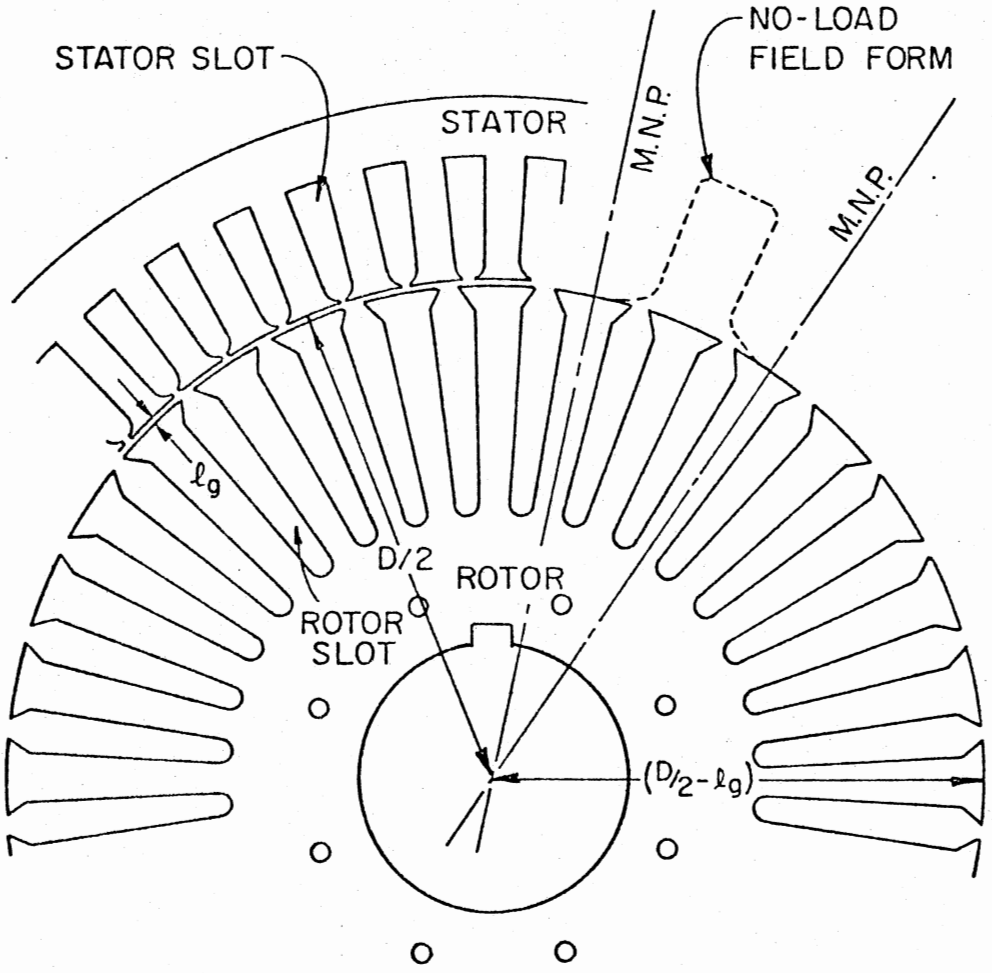

Figure 26. Illustrating the Stator and Rotor Laminations and the No-Load Field Form for the Experimental Prototype FMG

CHAPTER V

EXPERIMENTAL VERIFICATION

5.1 Introduction

Theoretical developments related to the idealized parallel-bridge rectifier system model, the basis for the selection of specific flat-topped source voltage waveforms both under no-load and full-load conditions and the results of Chapter III corresponding to the PBRS operation with bridge-input capacitors and resistive loads--all of these require some experimental verification to assess the validity of the assumptions made and to establish the usefulness of the theoretical results. The purpose of this chapter is to present the results of the experimental investigations undertaken using the available experimental prototype field modulated generator system and to discuss the results.

Experimental investigations are designed to:

1. Verify the validity of the flat-topped source voltage waveforms chosen under no-load and full-load conditions for the FMGS, compare the current and voltage waveforms at different points in the parallel-bridge rectifier system with the theoretical waveforms obtained, and study the effect of varying the load resistance on the current and voltage waveforms.

2. Establish an indirect method of determining the effective commutating reactance (X_L) of the field modulated generator by measuring the angles γ and β in the bridge-input voltage oscillograms.

3. Compare the experimental and theoretical values of angles γ and β for different values of load resistance and compare the theoretical values of the bridge-input voltage v_a at $\theta = \gamma$ for different loads (based on the design guidelines developed) with the experimental results.

The laboratory setup and testing methods are described and the oscillograms are recorded for each investigation. Sample calculations to obtain the value of the commutating reactance and the theoretical value of the bridge-input voltage are presented. A general discussion of the experimental results obtained is presented in the end.

Section 5.2 describes the experiments performed for the verification of the voltage and the current waveforms in the PBRS analysis. An indirect method of determining the commutating reactance is presented. A comparison of the experimental and theoretical values of angles γ, β and the bridge-input voltage v_a at $\theta = \gamma$ for different values of load resistance is also presented.

The chapter concludes with an overall discussion of the experimental results in section 5.3.

5.2 Description of the Experiments and the Results Obtained

5.2.1 Experimental Setup

A 10 kW, 220 volt, 16 pole, 7000 revolutions per minute, experimental prototype field modulated generator system belt driven by a 20 hp induction motor is used in the experimental investigations. The sinusoidal excitation voltage and current are at the modulation frequency of 60 hertz for the tests. Therefore, the output of the system is also at the same frequency. It can be seen that, with field modulation at 60

Hz, the modulation frequency ratio is at least 15, well above the minimum value of ten desirable for satisfactory operation. Appropriate shunts were installed at various points in the circuitry to observe and record current waveforms. With trapezoidal source voltage waveforms under full load conditions and field modulation, the bridge-input voltages are sinusoidally-modulated trapezoids. The output of the PBRS with field modulation is nearly a full wave rectified sine wave at the modulation frequency with some ripple (lowest order being at six times the basic machine frequency) superimposed. Since the idealized model assumes ideal solid state switching and filtering, the effect of the load connected across the PBRS or across the filter should be the same. However, in the experimental prototype FMGS, the load is connected across the filter. A lamp bank is used as the load in the experiments. A general view of the laboratory setup is shown in Figure 27.

5.2.2 Experimental Procedure

A full-pitch search coil located in the stator slots can be used to observe the waveform of the induced voltage in the stator windings. The search coil voltage oscillograms have been recorded (see Reference [32]) under no-load conditions without bridge-input capacitors and under full-load conditions with bridge-input capacitors. The bridge-input voltage and the FMGS output voltage oscillograms were also recorded under full-load conditions.

For a fixed value of the bridge-input capacitance (five micro farads), the load was varied by changing the number of light bulbs (6 through 10 bulbs; each rated at 1500 watts at 120 volts) in the lamp bank. The bulbs were connected in pairs to match the output voltage

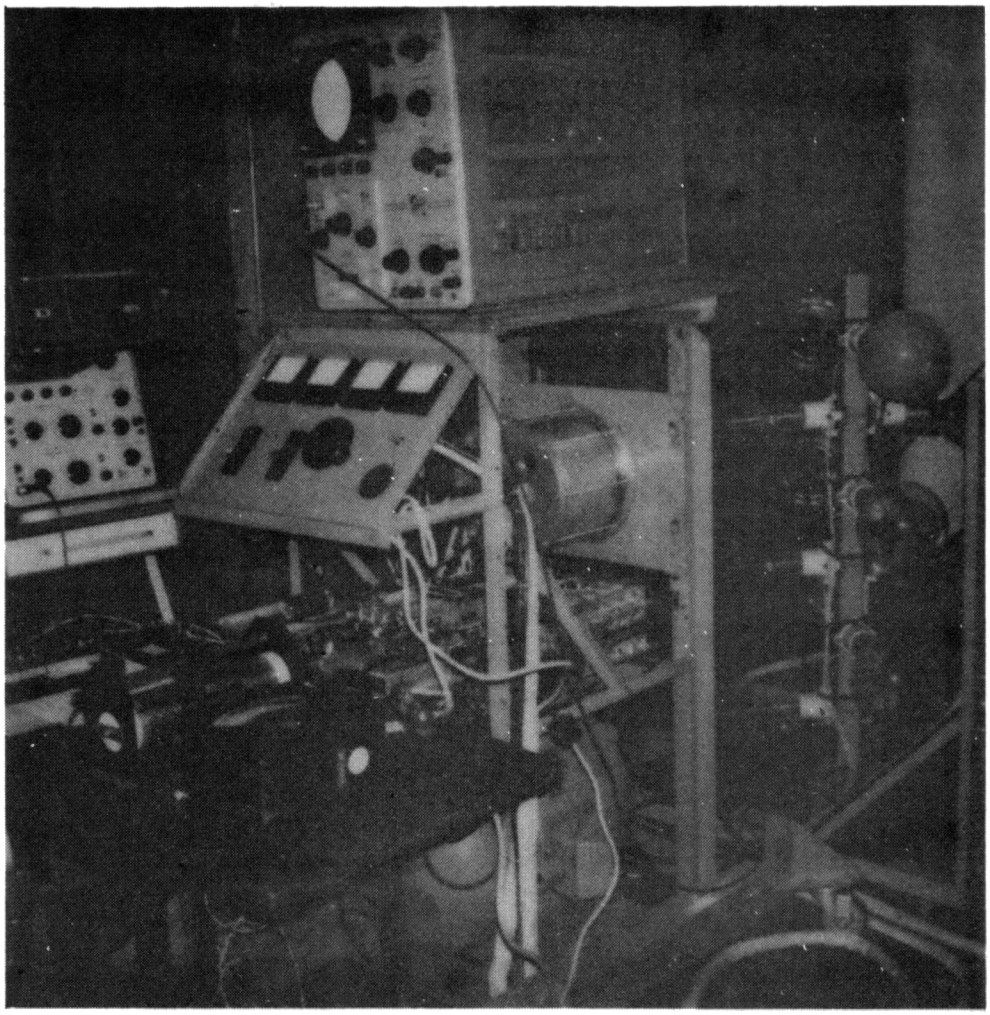

Figure 27. General View of the Experimental Setup

rating. With a load of 33A, oscillograms of bridge-input voltage, capacitor current, stator winding current and bridge-input current were recorded. The angles γ and β can be determined from the bridge input voltage waveform. In order to improve the accuracy of the values of γ and β, oscillograms of bridge-input voltage were recorded for two different time scales. Under full-load conditions (with a load current of 45A), oscillograms of bridge-input voltage, capacitor current and phase current were recorded. In the overload case (with a load current of 54A), the bridge-input voltage oscillograms were recorded for three different time scales for accurate determination of the angles γ and β.

5.2.3 Experimental Results

The basic high-frequency voltage waveform generated by the machine with no bridge-input capacitors and dc excitation is shown in Figure 28(a). The no-load induced voltage waveform can be represented by a series of positive and negative rectangular pulses. With field modulation, the no-load induced voltage waveform will be a sinusoidally-modulated rectangular pulse train.

Figure 28(b) shows the voltage induced in the search coil under full-load conditions with field modulation for a bridge-input capacitance of five micro farads. It can be seen that, in the presence of bridge-input capacitors, under full-load conditions, the source voltage waveform can be approximated by a symmetric trapezoid. As discussed earlier, this is the result of the special magnetic circuit design (with magnetic neutral planes in the centers of the teeth instead of in the centers of the slots) and armature reaction effects. Analysis of the

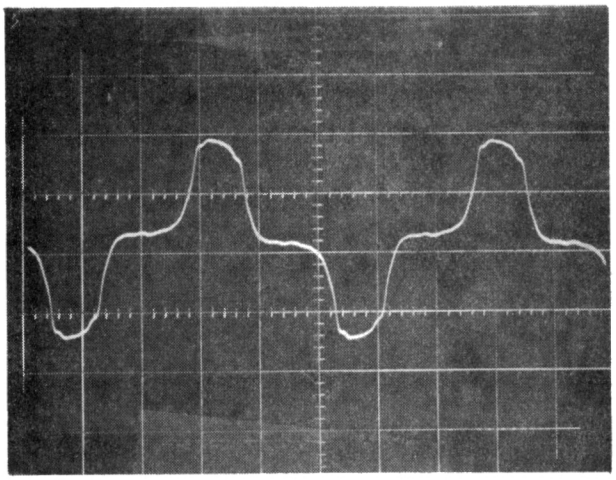

a.) High frequency voltage waveform for dc excitation with no bridge input capacitors

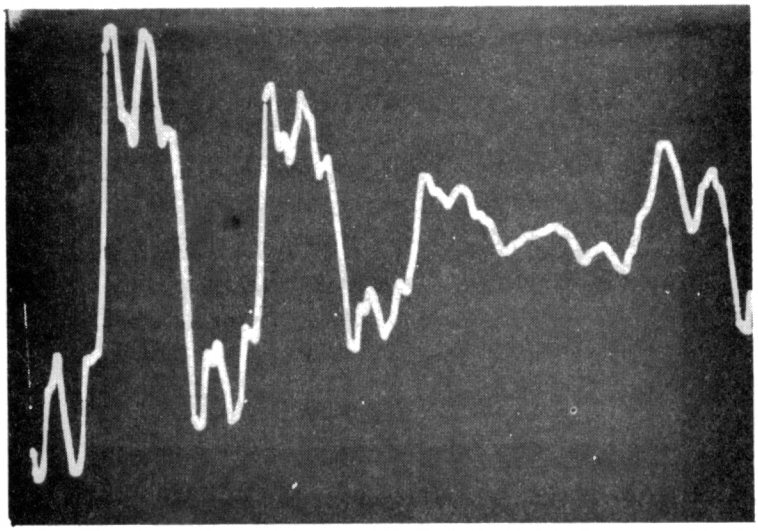

b.) Search coil voltage under full load conditions with field modulation and C = 5μF

Figure 28. Search Coil Voltage Without and With Bridge Input Capacitors Under dc Excitation and Field Modulation, Respectively

PBRS with bridge-input capacitors and trapezoidal source voltage waveforms was presented in Chapter III.

With trapezoidal source voltage waveforms under full-load conditions, the bridge-input voltage with sinusoidal field modulation will be approximately a sinusoidally-modulated trapezoid. An oscillogram of the bridge-input voltage waveform is shown in Figure 29(a), which justifies the statement just made. The output voltage waveform of the FMGS is a sinusoid at the modulation frequency as shown in Figure 29(b).

Figure 30 shows the oscillograms of phase-a bridge-input voltage (v_a), capacitor current (i_{ac}), phase current (i_a), and bridge-input current ($i_{a\ell}$) for a load current of 33A. The bridge-input voltage waveform is shown for two different time scales to improve the accuracy in the determination of the angles γ and β.

The bridge-input voltage (v_a) waveform is a trapezoid with very small voltage variations in the flat portion. The sloping edges of the trapezoid correspond to the decoupled (from the load) durations of a phase. During these durations, conduction of a phase is through the series circuit consisting of the commutating inductance and the bridge-input capacitor (see Figure 15). A significant capacitor current flows during this duration as shown in the oscillogram of the capacitor current i_{ac}. The current through the capacitor during the rest of the time is small. Whenever a bridge is decoupled, the bridge-input current ($i_{a\ell}$) is zero. When a bridge starts conducting through the load, there is an instantaneous transfer of current from the capacitor to the load. This instantaneous transfer can be seen in the oscillogram of $i_{a\ell}$ and a simultaneous sudden drop in the capacitor current can also be seen in the oscillogram of i_{ac}. As required, the current flow through the

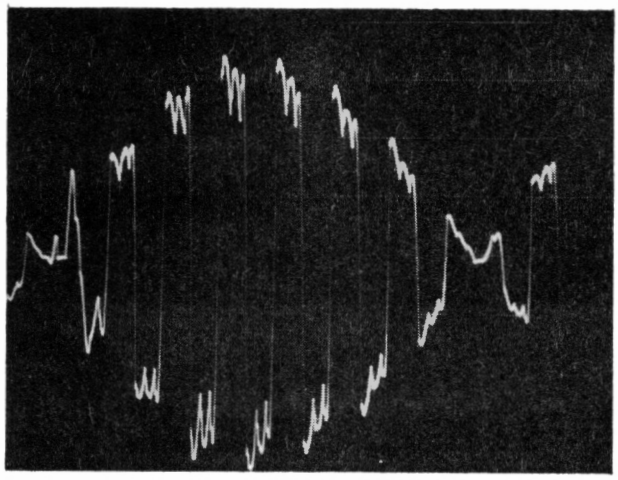

v_a envelope for I_ℓ = 45A
Scales x : 0.01 ms/cm; y : 100V/cm

a.) Sinusoidally modulated trapezoidal bridge input voltage waveform

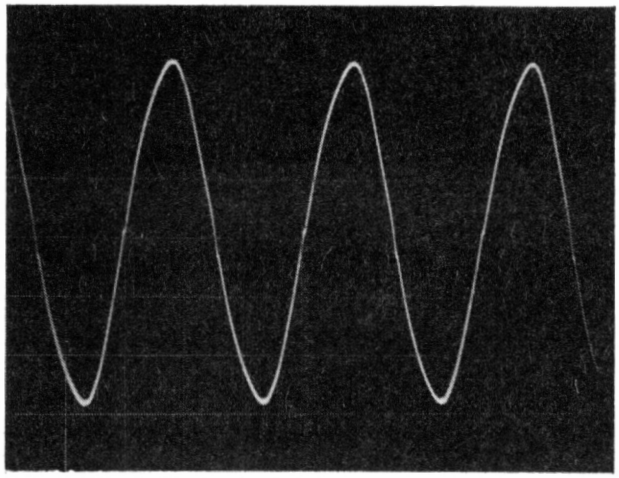

V_{rms} for I_ℓ = 45A
Scales x : 5ms/cm; y : 50V/cm

b.) Sinusoidal output voltage waveform of the FMGS

Figure 29. Bridge Input Voltage Envelope and Output Sinusoidal Waveform

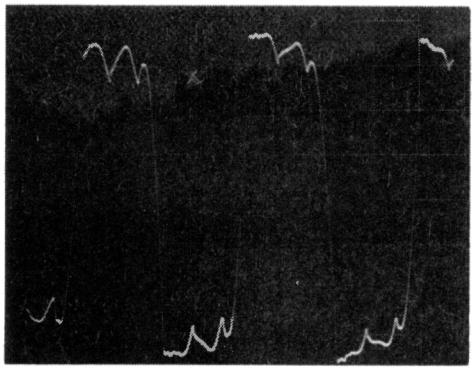

v_a for I_ℓ = 33A
Scales x : 0.2 ms/cm; y : 100V/cm

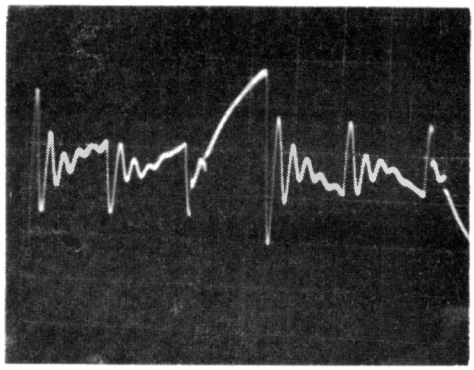

i_{ac} for I_ℓ = 33A
Scales x: 0.1ms/cm ; y: 10A/cm

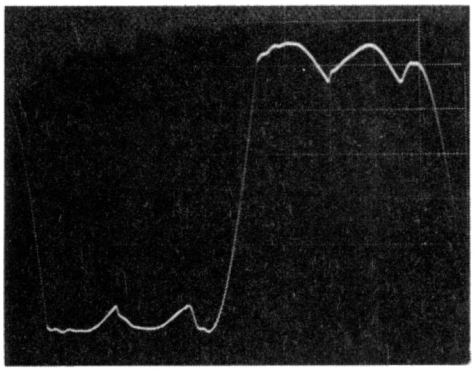

v_a for I_ℓ = 33A
Scales x : 0.1 ms/cm; y : 100V/cm

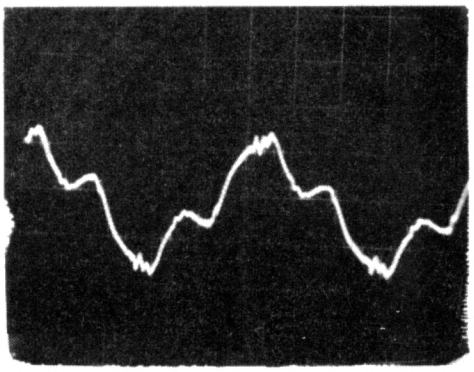

i_a for I_ℓ = 33A
Scales x: 0.2ms/cm ; y: 10A/cm

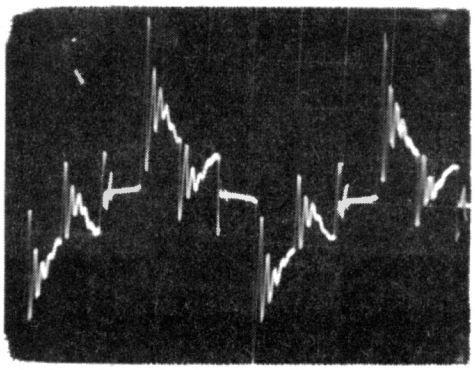

$i_{a\ell}$ for I_ℓ = 33A
Scales x: 0.2ms/cm ; y: 10A/cm

Figure 30. v_a, i_{ac}, i_a and $i_{a\ell}$ Oscillograms for I_ℓ = 33A

commutating inductance (i_a), which is the sum of i_{ac} and $i_{a\ell}$, is smooth and without jumps as shown in the oscillogram of i_a. Theoretical waveforms of phase current, capacitor current and bridge-input current are shown in Figure 20. The sudden transfer of capacitor current to the load gives rise to a small jump in the bridge-input voltage as seen in the oscillograms of v_a. The decoupled duration (γ/ω) of a phase can be obtained from the sloping edge of the trapezoid. The sum of the decoupled duration and the duration of the first hump in the bridge-input voltage should be equal to ($\pi/3\omega$).

Figure 31 shows the oscillograms of v_a, i_{ac} and i_a under full-load conditions (load current = 45A). The oscillograms for bridge-input voltage are shown for two different time scales. A substantial amount of capacitor current flows only during the decoupled duration of that phase. The bridge-input voltage waveforms are sinusoidally modulated trapezoidal waves. The phase current waveform is smooth as expected. Figure 32 shows the oscillograms of the bridge-input voltage for three different time scales with a load current of 54A.

It can be observed from the oscillograms that as the load current increases (which corresponds to a decrease in the load resistance), the ratio (X_L/R_ℓ) increases and the angle γ representing the decoupled duration of a phase decreases. The angle β increases with a decrease in the load resistance. The amplitude of the bridge input voltage decreases with an increase in the load current, indicating larger voltage drops in the commutating reactance. The peak value of the capacitor current increases with an increase in the load current. The humps in the bridge-input voltage become more prominent with an increase in the load current.

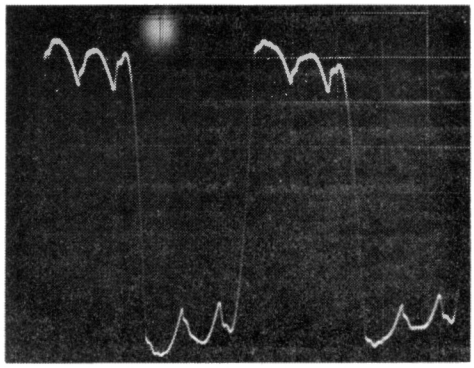

v_a for I_ℓ = 45A
Scales x : 0.2 ms/cm; y : 100V/cm

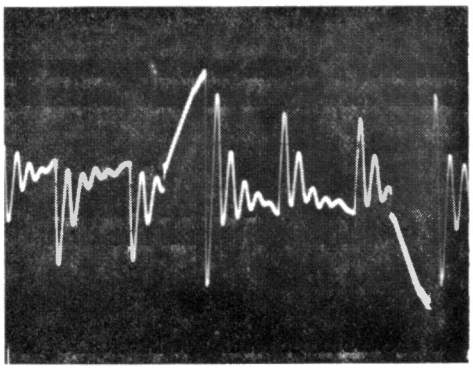

i_{ac} for I_ℓ = 45A
Scales x : 0.1ms/cm ; y: 10A/cm

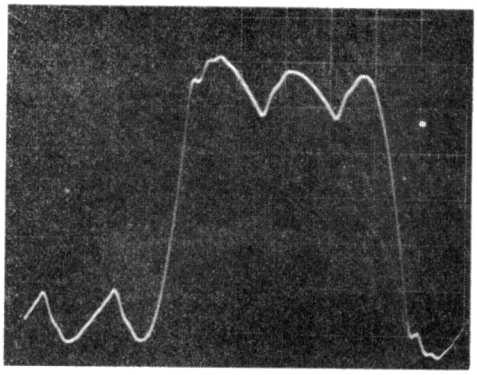

v_a for I_ℓ = 45A
Scales x : 0.1 ms/cm; y : 100V/cm

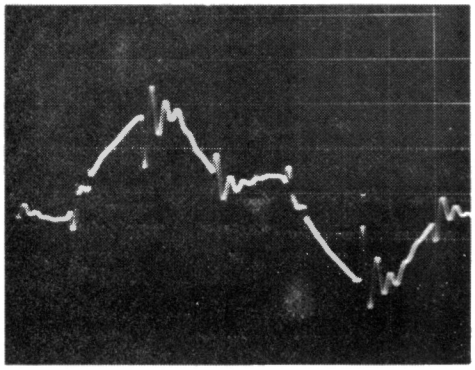

i_a for I_ℓ = 45A
Scales x: 0.1ms/cm ; y: 10A/cm

Figure 31. v_a, i_{ac}, and i_a Oscillograms for I_ℓ = 45A

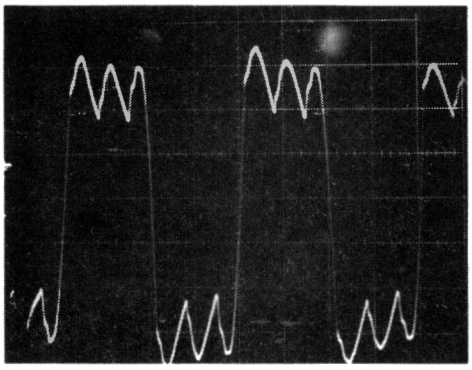

v_a for I_ℓ = 54A
Scales x : 0.1 ms/cm; y : 100V/cm

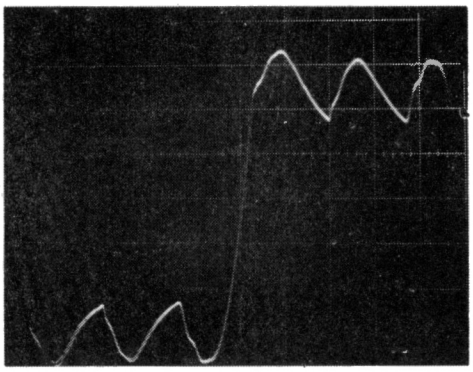

v_a for I_ℓ = 54A
Scales x : 0.1 ms/cm; y : 100Vcm

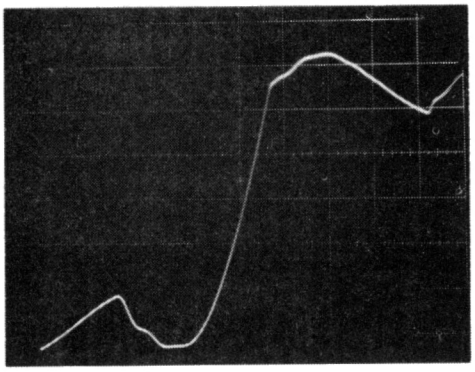

v_a for I_ℓ = 54A
Scales x : 0.05 ms/cm; y : 100V/cm

Figure 32. v_a Oscillograms With Different Time Scales for I_ℓ = 54A

5.2.4 Determination of the Commutating Reactance

The angles γ and β can be determined from the bridge-input voltage oscillogram shown in Figure 31 under full-load conditions. The angle γ corresponds to the decoupled duration of a bridge. This can also be obtained from the capacitor current waveform. The decoupled duration of a bridge and the duration of the first hump in the bridge-input voltage should sum up to $(\pi/3\omega)$. From the theoretical waveforms obtained for the bridge-input voltage v_a (see Figure 19), with $(\gamma + \beta) < \pi/3$, the duration $(\pi/3\omega)$ is divided into three segments--(γ/ω), (β/ω) and $((\pi/3) - \beta - \gamma)/\omega$. Comparing the general theoretical bridge-input voltage waveform with the bridge-input voltage oscillogram, the angles γ and β are obtained as 0.74 radian and 0.055 radian, respectively. Corresponding to these values of γ and β, the ratios (X_L/R_ℓ) and (X_L/X_C) are read from Figure 18 as

$$X_L/R_\ell = 0.91$$

$$X_L/X_C = 0.114$$

The value of the load resistance R_ℓ under full load is 4.66 ohms. The value of X_C at the machine frequency of 900 Hz and a capacitance value of five microfarad is 35.36 ohms.

The value of X_L derived from the ratio (X_L/R_ℓ) is 4.24 ohms and the value of X_L obtained from the ratio (X_L/X_C) is 4.03 ohms. Taking an average of these two values of X_L, the commutating reactance of the field modulated generator is estimated as 4.1 ohms. Accordingly, the commutating inductance L per-phase of the stator winding (with a basic machine frequency of 900 Hz) is 0.73 mH.

5.2.5 Comparison of Theoretical and Experimental Values of γ, β and v_a (at $\theta = \gamma$)

For three different values of the load resistance R_ℓ, with a constant bridge-input capacitance value of 5 μF, and from the computed value of the commutating reactance X_L, the parameter ratios (X_L/R_ℓ) and (X_L/X_C) were computed. The theoretical values of γ and β corresponding to the calculated parameter ratios were obtained from Figure 18. The experimental values for γ and β were determined from the oscillograms as mentioned in an earlier section. Theoretical and experimental values of γ and β are listed in Table I. Maximum deviations in the magnitudes of γ and β are 13.8 and 11.1 percent, respectively.

At $\theta = \gamma$, the decoupled bridge of phase-a starts conducting through the load. Whenever a bridge conducts, assuming ideal diodes, the bridge input voltage is equal to the load voltage. The load current $I_{\ell 1}$ at $\theta = \gamma$ with $(\gamma + \beta) < (\pi/3)$, is given by Equation (3.3.13). With the value of R_ℓ known, the voltage across the load resistance can be determined in terms of the maximum peak value of the voltage induced per phase (E) in the stator winding.

For a given rms output voltage V_{rms} of the FMGS, the peak value of the output voltage V_p for sinusoidal waveform was determined. The relationship between V_p and V_d (the load voltage normalized with respect to the maximum peak induced voltage per phase (E) in the stator) is given by

$$V_p = V_d \, K_{ff}$$

where the filtering factor K_{ff} is unity for ideal filtering conditions.

For given parameter ratios (X_L/R_ℓ) and (X_L/X_C), the ratio (V_d/E) was determined from Figure 23. The value of E and thus the theoretical

TABLE I

THEORETICAL AND EXPERIMENTAL VALUES OF γ, β AND v_a (AT $\theta = \gamma$)

Number of Lamps in Parallel at 1500 kW, 120 V	6	8	10
C (μF)	5	5	5
$I_{\ell_{rms}}$ A	33	45	54
V_{rms} V	200	210	210
R_ℓ (ohm)	6.06	4.66	3.88
X_L/R_ℓ	0.68	0.89	1.06
X_L/X_C	0.11	0.11	0.11
Theoretical Value of Angle γ (degree)	43.50	43.00	41.00
Experimental Value of Angle γ (degree)	48.10	42.00	36.00
Deviation in γ (percent)	-9.56	+2.38	+13.80
Theoretical Value of Angle β (degree)	0.028	1.95	5.73
Experimental Value of Angle β (degree)	0.031	2.15	6.45
Deviation in β (percent)	-9.67	-9.30	-11.10
Theoretical Value of v_a (at $\theta = \gamma$), V	388	382	380
Experimental Value of V_a (at $\theta = \gamma$), V	370	350	345
Deviation in v_a (percent)	4.86	9.14	10.14

value of the bridge-input voltage at $\theta = \gamma$ was determined. The experimental values of the bridge input voltage at $\theta = \gamma$ were obtained from the oscillograms. Theoretical and experimental values of the bridge-input voltage v_a at $\theta = \gamma$ for different loads are listed in Table I. It can be seen that the maximum deviation is 10.14 percent.

The primary conclusions drawn from this experimental study are listed below:

1. The nonsinusoidal source voltage waveforms for which the PBRS has been analyzed in Chapters II and III agree fairly well with the source voltage waveforms obtained with the special magnetic circuit employed in the FMGS.

2. The general character of the capacitor current, the bridge-input current, the phase current, and the bridge-input voltage waveforms obtained from the experimental study agree well with the corresponding theoretical waveforms, thereby validating the assumptions made in the analysis.

3. The theoretical and experimental values of angles γ and β agree well and the maximum deviation is less than 14 percent.

4. With (X_L/X_C) constant, decreasing the load resistance decreases γ and increases β.

5. The bridge input voltage decreases with an increase in the load current. The humps in the bridge-input voltage become more prominent with an increase in the load current. This is due to the increase in the peak value of the capacitor current associated with an increase in the load current.

6. Determination of the commutating reactance by conventional methods is difficult and not completely valid because of the

nonsinusoidal nature of the voltage and current waveforms. An indirect and experimental method of determining the commutating reactance has been suggested.

7. The bridge-input voltage values obtained at $\theta = \gamma$ for different loads using the theoretical analysis and the design guidelines developed agree fairly well with the experimental values, thereby validating the design approach.

These conclusions taken in total appear to confirm the theoretical analysis presented in Chapter III and the design guidelines developed in Chapter IV.

5.3 Discussion

The series of experimental investigations was designed on the basis of the study of the operation of the PBRS with bridge-input capacitors under resistive loads for nonsinusoidal source voltage waveforms. The experimental results obtained confirmed the theoretical predictions and the assumptions made in the analysis. Theoretical and experimental current and voltage waveforms at different locations in the PBRS circuit agree fairly well, except for the additional ripple due to the harmonic effects not included in the analysis. The basic assumptions made are justified by the experimental results. Experimental values of angles γ, β and the bridge-input voltage v_a (at $\theta = \gamma$) agree fairly well with the theoretical values, with maximum deviations of 13.8, 11.1 and 10.14 percent, respectively.

The main sources of disparity are: (1) the assumption that the source voltage waveform is a perfect trapezoid under full-load conditions; (2) harmonics in the machine (source) waveform; (3) neglecting

the capacitor current during the conduction duration of a bridge; (4) the assumption that filtering conditions are ideal; (5) errors involved in the determination of the angles γ and β from the oscillograms recorded; (6) numerical errors inherent in the evaluation of angles γ and β; (7) instrumentation and measurement errors; and (8) errors inherent in the other idealizing assumptions.

In spite of the many sources of errors, correlation between theory and experiment is reasonably good and the departures are within acceptable limits.

CHAPTER VI

SUMMARY AND CONCLUSIONS

6.1 Summary of Results and Conclusions

The primary objective of this thesis research was to study the influence of non-sinusoidal (especially flat-topped) source voltage waveforms on the operation of the parallel-bridge rectifier system and the field modulated generator system, leading to the development of some practical design guidelines for the FMGS.

During the past nine years, several prototype FMGS have been designed, fabricated and successfully tested at Oklahoma State University. It was observed during this process that, certain variations in the magnetic circuit design yielded significant advantages by way of reducing the excitation requirements and improving the overall efficiency and power output capability. The variations in the magnetic circuit design changed the induced voltage waveform in the stator windings under both no-load and loaded conditions. In particular, a round (slotted) rotor with magnetic neutral planes in the centers of alternate teeth (instead of being in centers of slots) corresponding to a no-load induced voltage waveform which is flat topped (esentially a rectangular pulse) resulted in the best performance, manifested in terms of high efficiency, improved output voltage waveform (less filtering) and decreased excitation requirements. Absence of any previous theoretical study based on this phenomenon prompted this research.

The waveform of the voltage induced in the stator windings of an alternator changes with the load due to the associated armature reaction effects. Incorporation of solid-state power-conditioning devices at the outputs of rotating machines further distorts the waveforms and introduces harmonics in different parts of the system. In addition, the presence of stator tuning capacitors provides closed paths for harmonic currents to circulate. A rigorous analysis of the PBRS - alternator combination based on the initial source voltage waveform and its dependence on the load is extremely involved. Therefore, in this thesis, as a first step, some judicious approximations are made to enable the study of the basic behavior of the PBRS and the FMGS with non-sinusoidal flat-topped waveforms.

In the absence of bridge input capacitors, the induced voltage waveform in the stator windings of the FMGS is essentially a rectangular pulse. This suggested the first step in the theoretical development--namely the analysis of the parallel-bridge rectifier system with rectangular-pulse source-waveform and resistive load. The induced voltage waveform in the stator windings under full-load conditions with bridge-input capacitors and resistive load is very close to a symmetric trapezoid with top width approximately equal to one-third of the half-period. This is the net result of the no-load field form, magnetic circuit configuration and armature reaction effects. Hence the PBRS is analyzed next with such trapezoidal source voltages, bridge-input capacitors and resistive loads.

From the results of the PBRS analysis with trapezoidal source voltages, a relationship between the normalized (with respect to the maximum source voltage) load voltage and circuit parameters is derived. Using

this as the starting point and by considering the low-frequency output as equivalent to a slowly-varying dc, extension of the PBRS studies to the field modulated case is discussed. Although the basic design approach for the field modulated generator is similar to that of a conventional three-phase synchronous machine, the effect of field modulation and operation at different speeds must be carefully incorporated in the machine design. These topics are discussed in detail.

Experimental investigations conducted using an available prototype show good agreement with the theoretical results. Deviations are within allowable limits, in spite of the many idealizing assumptions made. Thus the results of this research have led to the development of sound design guidelines for the FMGS and have laid a viable foundation for further work.

Chapter II considers the effect of rectangular-pulse source-voltage waveforms on the operation of the parallel-bridge rectifier system without bridge-input capacitors. The two angles α and β related to the on and off conditions of various diodes determine the number of phases conducting simultaneously through the load and the stagger between the zeros of the source voltage and the corresponding phase current. Numerical values of these angles are obtained as functions of the circuit parameter ratio (X_L/R_ℓ) and the pulse width ratio (K). The non-sinusoidal nature of the input waveform requires splitting the conduction duration into a number of segments for the purpose of analysis. Different ranges of values for the angles α and β must be considered due to the overlapping of current and voltage waveforms. The dependence of α and β on (X_L/R_ℓ) and K is observed to be smooth and without jumps. Theoretical waveforms of different voltages and currents are obtained for specific

values of K and the parameter ratio (X_L/R_ℓ). For a given pulse width ratio K, as (X_L/R_ℓ) increases, both the angles α and β increase but the peak amplitudes of the load current and the phase current decrease.

Chapter III introduces the assumptions made in the analysis of the PBRS with bridge-input capacitors and resistive loads for symmetric trapezoidal source voltages with top width equal to one-third of the half-period. The key assumption that simplifies the analysis involves the capacitor current during the conduction duration of a bridge. It is neglected as small in comparison with the load component of the bridge-input current. In this case, the angles γ and β determine the decoupled duration of a bridge and the time difference between the zeros of the source voltage and the corresponding phase current, respectively. Two ranges of values for the sum $(\gamma+\beta)$ are identified to include most of the practical cases of interest. Standard subroutines for the solution of simultaneous non-linear algebraic equations are employed in the determination of the angles γ and β. Numerical values of γ and β are presented as functions of the circuit constant ratios (X_L/R_ℓ) and (X_L/X_C). Typical theoretical current and voltage waveforms are shown for a set of parameter ratios chosen.

The parameter ratios (X_L/R_ℓ) and (X_L/X_C) play a vital role in determining the on and off durations of the bridges. The transfer of conduction from one diode pair to the other of any one bridge is associated with a decoupling of that bridge for a duration (γ/ω). During the decoupled duration of a bridge, the current flow is completed through the series circuit consisting of the commutating inductance and the bridge-input capacitance. With large values of the bridge-input capacitance and the load resistance, over-voltages occur at the bridge-input termi-

nals. With $(\gamma+\beta)<\pi/3$, the angle β increases with a decrease in the load resistance and with a decrease in the bridge-input capacitance. In the region $(\gamma+\beta)>\pi/3$, the angle β increases with a decrease in the load resistance and with an increase in the bridge-input capacitance. The angle γ increases with increases in the load resistance and capacitance. The peak amplitude of the capacitor current increases with an increase in the load current. This has a tendency to make the humps in the bridge input voltage prominent. For given parameter ratios (X_L/R_ℓ) and (X_L/X_C), the angles γ and β obtained with trapezoidal source voltage waveform are a little larger than the corresponding values obtained with sinusoidal source-voltage waveforms.

Chapter IV discusses the assumptions involved in the extension of the PBRS studies to the field modulated case. The results of Chapter III are first employed to derive a relationship between E, V_d and the circuit parameter ratios (X_L/R_ℓ) and (X_L/X_C). Assuming that the low-frequency output can be considered as equivalent to a slowly-varying dc, the results of Chapter III are then extended to the field modulated case.

Because of the modulation of the field, the magnetic circuit utilization is poor in the FMGS. With the same peak value, the rms value of the currents with field modulation is lower than the rms value of the currents for the unmodulated case. Therefore, with the same maximum peak current density and conductor size, the copper losses in the stator will be less with field modulation. Thus the effect of poor magnetic circuit utilization is partly compensated by the fact that higher peak currents and correspondingly higher outputs can be allowed without exceeding the limit on the stator copper lossses in the field modulated generator.

It is appropriate at this point to formulate a rule-of-thumb to incorporate the field modulation effect in the determination of the main dimensions for the field modulated generator. If it is possible to arrive at a factor by which the D^2L_c product obtained by the conventional machine design approach could be multiplied to include the modulation effects, then the design procedure will be considerably simplified. The two effects, namely, the poor magnetic circuit utilization and the capability to carry higher peak currents, considered together, yield a factor which is between $\pi/2$ and $\pi/2\sqrt{2}$. A realistic value for the factor will be closer to $\pi/2\sqrt{2}$ especially because of the transfer of some of the rotor copper losses to the stator by the use of stator tuning capacitors. A value in the range of 1.15 to 1.2 is suggested in this thesis for this factor.

The magnetic circuit and the excitation coil of the FMG should be designed on the basis of the peak value of the output voltage. In order to develop a relationship between the peak value of the output voltage and the corresponding maximum value of the induced voltage per phase in the stator winding, the effect of modulation can be considered as equivalent to a slowly-varying dc. Then the number of turns per phase in the stator can be determined based on the relationship between E, V_d, (X_L/R_ℓ) and (X_L/X_C). A numerical example is included in Chapter IV to illustrate the design procedure.

Chapter V starts with a description of the experimental investigations conducted with the available 10kW, 220V, 7000r/min, 60Hz prototype field modulated generator system. The objective of the investigations was to determine the effect of varying the load resistance on the various current and voltage waveforms under resistive load conditions. An in-

direct method for the determination of the commutating reactance by using a combination of theoretical and experimental results was developed. Three values of load resistance were employed to correlate the experimental and the theoretical values of γ, β and v_a(at $\theta=\gamma$). Maximum deviations in γ, β and v_a(at $\theta=\gamma$) were 13.8, 11.1 and 10.14 percent respectively. All the oscillograms taken are documented, sample calculations are presented and the sources of errors are discussed in detail. Finally, the good overall agreement between the theoretical and the experimental results confirms the validity of the assumptions made in the theoretical analysis presented and in the design guidelines developed.

6.2 Scope for Further Work

Extension of this thesis research is recommended in several areas. Symmetric trapezoidal source-voltage waveform effects on the operation of the parallel-bridge rectifier system with bridge-input capacitors and resistive loads should be extended to include; a) non-resistive (both inductive and capacitive) loads to encompass situations that will occur in practice; b) the effect of varying the top-width of the trapezoid on angles γ, β and the output voltage; c) the effect of considering the harmonic content in the various voltages and currents of interest; and d) effects of non-ideal solid state devices and non-ideal switching. The design guidelines developed to include field modulation effects should be extended to the rotor and the magnetic circuit design.

It has been observed during the experimental investigations that the source voltage waveform under light load conditions does not remain a trapezoid and is highly distorted. Therefore studies on the PBRS with

bridge input capacitors should be carried out in detail to include light load conditions.

Relaxation of the idealizing assumptions should start with the development of a method to include magnetic circuit saturation. One possible approach is to consider the commutating reactance to be a function of the load and to introduce approporiate variations in the effective rotor reactance. The effective commutating reactance of the FMGS with the special magnetic circuit should be expressed in terms of the machine physical characteristics to develop guidelines for future designs. Effects of phase shifts in the modulation envelopes on the operation of the system--especially on the timing of the triggering signals required, should be investigated. Consequences of including the transformer voltages in the machine stator windings and the development of a realistic model for the filter circuit are some of the refinements that require additional work. Extensive opportunities for further research exist in the areas of output filtering, transient behavior, stability, control and application aspects of the FMGS operating independently or in conjunction with utility grids.

A SELECTED BIBLIOGRAPHY

[1] MacNeil, C. I. "Electrical Apparatus." U.S. Patent No. 2,659,044, November, 1953.

[2] Hughes, W. L., H. J. Allison, and R. Ramakumar. "A Variable Frequency Power Source for Ground Transportation." Proceedings, Seventh Intersociety Energy Conversion Engineering Conference, California (September, 1972), pp. 996-1002.

[3] Ramakumar, R., H. J. Allison, and W. L. Hughes. "Variable Speed Drive Applications of Field Modulated Frequency Down Converters." 1973 SWIEEECO Record, IEEE Catalog No. 73 CHO 719-5-SWIECO, Houston, Texas (April, 1973), pp. 162-165.

[4] Ramakumar, R. "Development and Adaptation of Field Modulated Generator Systems for Wind Energy Applications." Proceedings, Second Wind Energy Conversion Systems Workshop, sponsored by ERDA and NSF, Washington, D.C. (June, 1975), pp. 279-289.

[5] Ramakumar, R. "Harnessing Wind Power in Developing Countries." Proceedings, Tenth Intersociety Energy Conversion Engineering Conference, IEEE Catalog No. 75 CHO 983-7 TAB, Newark, Delaware (August, 1975), pp. 966-973.

[6] Ramakumar, R. "Wind Electric Conversion Utilizing Field Modulated Generator Systems." Sharing the Sun 76-Solar Technology in the Seventies Conference, sponsored by the American Section of the ISES and the Solar Energy Society of Canada, Winnipeg, Manitoba, Canada, Vol. 7 (August, 1976), pp. 215-229.

[7] Ramakumar, R. "Wind Driven Field Modulated Generator Systems." Proceedings, Eleventh Intersociety Energy Conversion Engineering Conference, State Line, Nevada (September, 1976), pp. 1766-1772.

[8] Jayadev, T. S. "Windmills Stage a Comeback." The Institute of Electrical and Electronics Engineers, Spectrum, Vol. 13, No. 11 (November, 1976), pp. 45-49.

[9] Divone, L. V., and J. M. Savino. "The US-NSF/NASA Wind Energy Conversion System Program." Proceedings, Advanced Wind Energy Systems Workshop 1974, Vol. 2, Stockholm, Sweden (1976), pp. 7-25 to 7-33.

[10] Fernandes, R. A. "Optimum Peak Sharing Mix for Electric Utilities." IEEE Conference Paper No. C 75-143-3, Energy Development II, IEEE Catalog No. 76 CH 1102-3-PWR (1975), pp. 83-91.

[11] Ramakumar, R., and K. Bahrami. Application of Field-Modulated Generator Systems to Dispersed Solar Thermal Electric Generation. Report prepared for U. S. Department of Energy, by Jet Propulsion Laboratory, JPL Publication 79-83, California Institute of Technology, Pasadena, California, August 15, 1979.

[12] Owen, T. B. "Variable-Speed Constant-Frequency Devices: A Survey of the Methods in Use and Proposed." AIEE Transactions (Part II. Applications and Industry), Vol. 78 (November, 1959), pp. 321-326.

[13] Chirgwin, K. M., and L. J. Stratton. "Variable-Speed Constant-Frequency Generator System for Aircraft." AIEE Transactions (Part II. Applications and Industry), Vol. 78 (November, 1959), pp. 304-310.

[14] Hoard, B. V. "Constant-Frequency Variable-Speed Frequency-Make-Up Generators." AIEE Transactions (Part II. Applications and Industry), Vol. 78 (November, 1959), pp. 297-304.

[15] Kimbark, E. W. Direct Current Transmission. Vol. I. New York: John Wiley and Sons, 1971.

[16] Adkins, B., and W. J. Gibbs. Polyphase Commutator Machines. London: Cambridge University Press, 1951.

[17] Daniels, A. R. The Performance of Electrical Machines. London: McGraw-Hill, 1968.

[18] Jesse, R. D., and W. J. Spaven. "Constant-Frequency A-C Power Using Variable Speed Generation." AIEE Transactions (Part II: Applications and Industry), Vol. 78 (January, 1960), pp. 411-418.

[19] Chirgwin, K. M., L. J. Stratton, and J. R. Toth. "Precise Frequency Power Generation From an Unregulated Shaft." AIEE Transactions (Part II. Applications and Industry), Vol. 79 (January, 1961), pp. 442-451.

[20] Harnden, J. D., Jr., and F. B. Golden, editors. Power Semiconductor Applications, Vols. I and II. New York: IEEE Press, 1972.

[21] Hughes, W. L., H. J. Allison, and R. Ramakumar. "Apparatus for Providing A-C Electrical Energy at a Preselected Frequency." U.S. Patent No. 3,663,945, dated May 16, 1972.

[22] Benton, B. M., and R. P. Judkins. "Frequency Control Device for Generators." U.S. Patent No. 2,896, 150, dated July 21, 1959.

[23] Johnson, L. J. "Apparatus for Producing Alternating Current." U.S. Patent No. 3,001,124, dated September 19, 1961.

[24] Wickson, A. K. "A Simple Variable Speed Independent Frequency Generator." Proceedings, AIEE Summer and Pacific General Meeting and Air Transportation Conference, Seattle, Washington, Paper No. CP 59-915 (June, 1959).

[25] Bernstein, T., and N. L. Schmitz. "Variable Speed Constant Frequency Generator Circuit Using a Controlled Rectifier Power Demodulator." Proceedings, AIEE Pacific General Meeting, San Diego, California, Paper No. CP 60-1053 (August, 1960).

[26] Ramakumar, R., and H. J. Allison. "Design-Fabrication and Layout of a 60 kW Three-Phase Field Modulated Generator System." Proceedings, Frontiers of Power Technology Conference, Oklahoma State University, Stillwater (October, 1972), pp. 16-1 to 16-9.

[27] Allison, H. J., R. Ramakumar, and W. L. Hughes. "A Field Modulated Frequency Down Conversion Power System." IEEE Transactions on Industry Applications, Vol. IA-9, No. 2 (March/April, 1973), pp. 220-226.

[28] Ramakumar, R., H. J. Allison, and W. L. Hughes. "A Self-Excited Field Modulated Three-Phase Power System." IEEE Conference Paper No. C 74-318-2, Summer Power Meeting, Anaheim, California (July, 1974).

[29] Ramakumar, R., and C. C. Tsung. "An Approach to Model Field Modulated Generator Systems." Midwest Power Symposium Conference Record, University of Akron, Ohio (October, 1975).

[30] Tsung, C. C., and R. Ramakumar. "Idealized Model of Field Modulated Generator Systems: An Experimental Study." Midwest Power Symposium Conference Record, Kansas State University, Manhattan, Kansas (October, 1976).

[31] Ramakumar, R. et al. Development and Adaptation of Field Modulated Generator Systems for Wind Energy Applications. Final report, submitted to the Energy Research and Development Administration and the National Science Foundation, Washington, D.C. Contract No. ERDA/NSF-AER 75-00647. NTIS Accession No. PB 272495/AS (September, 1976).

[32] Ramakumar, R., H. J. Allison, and W. L. Hughes. "Description and Performance of a Field Modulated Frequency Down Converter." 1972 SWIEEECO Record, IEEE Catalog No. 72 CHO 595-9 SWIECO (April, 1972), pp. 252-256.

[33] Ramakumar, R., H. J. Allison, and W. L. Hughes. "Analysis of the Parallel-Bridge Rectifier System." IEEE Transactions on Industry Applications, Vol. IA-9, No. 4 (July/August, 1973), pp. 425-436.

[34] Ramakumar, R., H. J. Allison, and W. L. Hughes. "Operation of Alternators With Parallel-Bridge Rectifier Systems." IEEE Transactions on Power Apparatus and Systems, Vol. PAS-92, No. 5 (September/October, 1973), pp. 1679-1687.

[35] Altaf-ur-Rahman, and R. Ramakumar. "Waveform Effects on the Operation of the Parallel-Bridge Rectifier System." Midwest Power Symposium Conference Record, Ohio State University, Columbus, Ohio (October, 1979).

[36] Fitzgerald, A. E., C. Kingsley, and A. Kusko. Electric Machinery. New York: McGraw-Hill, 1971.

[37] Tsung, C. C., and R. Ramakumar. "A Study of the Parallel-Bridge Rectifier System With Bridge-Input Capacitors." Proceedings, Tenth Annual Meeting of the IEEE Industry Applications Society, IEEE Catalog No. 75 CHO 999-3 IA, Atlanta, Georgia (September/October, 1975), pp. 1012-1019.

[38] Tsung, Chi-Cheng, and R. Ramakumar. "Operation of Parallel-Bridge Rectifier Systems With Capacitors at Bridge Input." Midwest Power Symposium Conference Record, Vol. II, University of Missouri-Rolla, Rolla, Missouri (October, 1974).

[39] Tsung, C. C., and R. Ramakumar. "An Idealized Study of the Field Modulated Generator System." Proceedings, IEEE Power Engineering Society Winter Meeting, New York, New York, Paper No. A79 016-7 (February, 1979).

[40] International Mathematical and Statistical Libraries. Reference Manual, No. LIB03-0006V2, Vol. II, Chapter L-Z, revised July, 1977.

[41] Tsung, Chi-Cheng. "A Study of the Field Modulated Generator System." (Unpublished Ph.D. dissertation, Oklahoma State University, December, 1976.)

[42] Say, M. G., and E. N. Pink. The Performance and Design of Alternating Current Machines. London: Sir Isaac Pitman and Sons, 1936.

[43] Say, M. G. Alternating Current Machines. New York: John Wiley and Sons, 1976.

VITA

Altaf-ur-Rahman

Candidate for the Degree of

Doctor of Philosophy

Thesis: WAVEFORM EFFECTS ON THE OPERATION OF THE PARALLEL-BRIDGE RECTIFIER SYSTEM AND THE FIELD MODULATED GENERATOR SYSTEM

Major Field: Electrical Engineering

Biographical:

Personal Data: Born in Mahbubnagar, Andhra Pradesh, India, on January 20, 1944, the son of Mr. and Mrs. Mohammad Sultan Mohiuddin.

Education: Attended primary, middle and high school in Mahbubnagar, India; received the Bachelor of Engineering degree in Electrical Engineering from Osmania University, Hyderabad, India, in 1966; received the Master of Engineering degree in Automatic Control Engineering from the Maharaja Sayajirao University of Baroda, India, March, 1972; completed requirements for the Doctor of Philosophy degree at Oklahoma State University in December, 1979.

Professional Experience: Associate Lecturer in Electrical Engineering, Nagarjunasagar Engineering College, Jawaharlal Nehru Technological University, Hyderabad, India, July 18, 1966, to September 30, 1970; Lecturer in Electrical Engineering, Jawaharlal Nehru Technological University, Hyderabad, India, October 1, 1971, to August 12, 1975; graduate research and teaching associate, School of Electrical Engineering, Oklahoma State University, 1975-1976 and 1977-1979; research associate, Fluid Power Research Center, Oklahoma State University, 1976-1977.

Professional Organizations: Member of the Institute of Electrical and Electronics Engineers, Eta Kappa Nu, Indian Society for Technical Education.